



Durham E-Theses

NMR studies of solid nitrogen-containing dyestuffs

McGeorge, Gary

How to cite:

McGeorge, Gary (1996) *NMR studies of solid nitrogen-containing dyestuffs*, Durham theses, Durham University. Available at Durham E-Theses Online: <http://etheses.dur.ac.uk/5197/>

Use policy

The full-text may be used and/or reproduced, and given to third parties in any format or medium, without prior permission or charge, for personal research or study, educational, or not-for-profit purposes provided that:

- a full bibliographic reference is made to the original source
- a [link](#) is made to the metadata record in Durham E-Theses
- the full-text is not changed in any way

The full-text must not be sold in any format or medium without the formal permission of the copyright holders.

Please consult the [full Durham E-Theses policy](#) for further details.

NMR Studies of Solid Nitrogen-Containing Dyestuffs

The copyright of this thesis rests with the author.
No quotation from it should be published without
his prior written consent and information derived
from it should be acknowledged.

by

Gary McGeorge

B.Sc. University of Glasgow

A thesis submitted in partial fulfilment of the requirements for
the degree of Doctor of Philosophy

Department of Chemistry

University of Durham

1996

10 MAR 1997



Memorandum.

The research in this thesis has been carried out in the Department of Chemistry of the University of Durham between October 1993 and September 1996. It is the original work of the author unless otherwise stated. None of this work has been submitted for any other degree.

The copyright of this thesis rests with the author. No quotation from it should be published without his prior written consent and information derived from it should be acknowledged.

Acknowledgements.

There are a number of people I wish to thank who have contributed either directly or indirectly to the work in this thesis.

First, I would like to express thanks to my supervisor Professor Robin K. Harris for his supervision throughout the last three years, for financial aid to attend several conferences, and also for the opportunity to study at the University of Utah for three months. Barry Say, Dr A. M. Kenwright, Ian McKeag, Dr. D. C. Apperley, Nicola Apperley, Dr. U. Scheler and Dr. R. Challoner are all thanked for their helpful discussions and suggestions. Additionally, thanks are due to Dr. A. Porte at the University of Glasgow for introducing me to solid-state NMR during my undergraduate research project.

I would also like to thank EPSRC and *Zeneca Specialties* for financial support under a CASE award, without which I could not have carried out this research. At *Zeneca*, Drs. A. M. Chippendale, J. Bullock, C. Brennan, N. Hall and

B. Docherty, are all thanked sincerely for their help in my understanding of various fields of colour chemistry.

During my three months stay in Utah I made several friends who all made me feel very welcome and ensured that my stay was a pleasant one. Professor D. M. Grant should be thanked firstly for his kind invitation to work under him for the three month duration and use his spectrometers, along with Anita Orendt, Mark Solum, J. Harper and S. Bia who helped me understand and appreciate the Utahan way of life.

On a more personal note I thank my fellow members of the Durham NMR group over the past three years for their friendship: Stefan, Elke, Graham, Abdul, Peter, Anna, Tim, Se-Woung, Steve Carss, Steve Breen, Alison, Minoru, John and Susan.

Finally, I would like to thank Claire for putting up with me during the last three years, and for her patience and understanding whilst this thesis was being written.

NMR Studies of Solid Nitrogen-Containing Dyestuffs.

Gary McGeorge, B. Sc.

Abstract.

This thesis is concerned with the structural analysis of dyestuffs in their natural solid state by the application of solid-state nuclear magnetic resonance. These dyestuffs are all derived from the phenylazobenzene group, but tautomerism can produce structural changes, which have so far been uncharacterised in the solid state for many of the dyestuffs currently under investigation.

The information obtainable from ^{13}C and ^{15}N chemical shifts, both isotropic and anisotropic will be applied in this structure determination. Under magic-angle spinning the anisotropic nature of solid-state interactions is partially averaged or removed. The rotational resonance technique will be presented, which reintroduces the homonuclear dipolar interaction allowing dipolar coupling constants to be measured. Second-order effects arising from the ^{14}N quadrupole interaction broaden spin-1/2 lines (RDC) in such a manner that bond lengths can be determined. This RDC analysis will be applied to a series of hydrazone structures to determine the ^{15}N - ^{14}N bond length within the hydrazone linkage. Finally, the two-dimensional magic-angle turning experiment will be discussed and applied to both the ^{13}C and ^{15}N nuclei for a range of dyestuffs to show that accurate shielding tensor information can be obtained from large molecules.

Table of Contents.

1. INTRODUCTION.....	1
1.1 THESIS OVERVIEW.....	3
2. EXPERIMENTAL.....	6
2.1 SAMPLE PREPARATION AND CHARACTERISATION.....	6
2.2 NMR.....	7
2.2.1 Magic-angle spinning (MAS).....	7
2.2.2 Variable Temperature Operation.....	7
2.2.3 Observation of C-13.....	9
2.2.4 Observation of N-15.....	9
2.2.5 Pulse Sequences.....	10
3. ANALYSIS OF THE POLYMORPHS OF DR278.....	12
3.1 INFORMATION FROM TRADITIONAL NON-NMR TECHNIQUES.....	13
3.2 ELUCIDATION OF THE SOLUTION STATE STRUCTURES.....	15
3.3 SOLID-STATE STRUCTURES OF THE POLYMORPHS OF DR278.....	24
3.3.1 Carbon-13 NMR.....	24
3.3.2 Nitrogen-15 NMR.....	30
4. KINETICS ANALYSIS OF A LARGE-AMPLITUDE REORIENTATION.....	38
4.1 INTRODUCTION.....	38
4.1.1 Bandshape Analysis.....	41
4.2 MAGNETISATION TRANSFER EXPERIMENTS.....	45
4.2.1 1D Selective Polarisation Inversion (SPI).....	45
4.2.1.1 <i>Results: Application to DR278 form II.</i>	52
4.2.2 Two-dimensional exchange (EXSY).....	60
5. INVESTIGATION OF TAUTOMERISM IN SULPHONIC ACID AZOBENZENE DERIVATIVES BY C-13 AND N-15 NMR.....	67
5.1 APPLICATION OF C-13 AND N-15 NMR FOR THE ANALYSIS OF CARBOCYCLIC AZO DYES: A REVIEW.....	69
5.1.1 C-13 NMR.....	69
5.1.2 N-15 NMR.....	73

5.2 ANALYSIS OF NMR SPECTRA FOR A SERIES OF WATER SOLUBLE DYES	75
5.2.1 C-13 NMR.....	75
5.2.2 N-15 NMR.	98
5.3 THE SOLID-STATE STRUCTURE OF A TYPICAL REACTIVE AZO DYESTUFF.	108
6. ANALYSIS OF DIPOLAR COUPLED SPIN SYSTEMS USING N-15 NMR.	115
6.1 INTRODUCTION.....	115
6.2 SHIELDING THEORY:- SPECIAL EMPHASIS ON NITROGEN.	116
6.3 ¹⁵ N TENSOR ANALYSIS OF AZO AND IMINE GROUPS.	121
6.3.1 DR278 Polymorph II: α (II α), β (II β) and α , β (II δ) ¹⁵ N-labelled samples.	123
6.3.2 DR278 Polymorph VI: β (VI β) labelled samples.	132
6.3.3 Sulphonic acid azobenzene derivatives: β -labelled samples.....	133
6.4 REINTRODUCTION OF DIPOLAR INTERACTIONS UNDER MAS CONDITIONS.	139
6.4.1 Rotational Resonance: R ²	140
7. MAGIC-ANGLE TURNING SPECTROSCOPY.....	150
7.1 INTRODUCTION.....	150
7.2 THEORY OF MAT.	151
7.3 APPLICATION OF ¹³ C AND ¹⁵ N PHORMAT TO DYES AND PIGMENTS.....	157
7.3.1 CI-PV19: γ Linear-trans-quinacridone.....	157
7.3.2 DR278 VI.....	162
7.3.3 CI Pigment Red 57:1.....	164
8. APPENDIX.	168
9. ADDENDUM.	190

1. Introduction.

Nuclear magnetic resonance last year celebrated its 50th anniversary and several historical articles have been written which trace out the evolution of this important analytical technique.¹ Consequently, an encyclopaedia engaging all areas of NMR was published, which contains over 600 articles.² From a brief glance at these articles one can realise the great progress that has occurred in this field.

The corner-stone of modern solid-state NMR is the combination of cross polarisation³ with magic-angle spinning⁴ (CP/ MAS), which has allowed the observation of spin systems containing nuclei of low natural abundance, *e.g.* ^{15}N and ^{13}C . The lack of rapid isotropic molecular motion, as in solutions, renders the spectral features broad and featureless, and to obtain the high resolution desired in ^{13}C or ^{15}N spectra, MAS and high-power proton decoupling have to be applied. These techniques have allowed the determination of molecular structures that could not have been contemplated without such techniques. Extensions to these techniques have allowed two-dimensional experiments, analogous to solution-state ones, to be routinely obtained, opening up a whole new field. Two-dimensional studies of dynamic processes and molecular order in polymeric systems, for example, have proven useful in understanding their physical properties.⁵

The same interactions that one tries to remove to increase spectral resolution contain valuable information, and over the last decade solid-state nuclear magnetic resonance has undergone a dramatic transformation as a result of several technique developments, which allow the reintroduction of these interactions in a predictable



manner. These are principally the spin-spin dipolar coupling and the anisotropy in the shielding tensor. Dipolar coupling constants can provide constraints in the structural elucidation of biomolecules, which was previously not possible due to the removal of such couplings by rapid MAS. Additionally, the anisotropy of the shielding tensor can provide further structural information relating to the distribution of electron density surrounding a particular nucleus, and new two-dimensional techniques allow the accurate determination of the shielding tensors for various sites within a molecule.

The main problems concerning solid-state NMR are those of sensitivity and spectral resolution. For solid-state NMR to progress into the next century and compete with solution-state high-resolution NMR, I believe that it is paramount that these two problems should be solved. Both of these issues are being addressed by several pioneering laboratories. The combination of electron spin resonance spectroscopy with NMR spectroscopy in a technique called dynamic nuclear polarisation spectroscopy (DNP)⁶ has showed that hundred-fold increases in sensitivity can be observed for spectra obtained from dilute spin systems. This will open up a whole new world of structural elucidation for the NMR spectroscopist interested in biomolecules, for example. The sensitivity issue has also been approached by increasing the static field strength to the maximum possible for solid-state NMR at the current moment; that of 750 MHz. Increased resolution has also been obtained by the application of solid-state NMR at this increased field strength, with J-coupling being observed in the spectra of rigid organic solids.⁷ Increased resolution has also been possible by the application of a two-pulse phase modulation

decoupling scheme,⁸ which increases the efficiency of high-power proton decoupling.

1.1 Thesis Overview.

In this thesis several techniques, both old and new, will be presented which allow the determination of dipolar and shielding parameters, which are useful in understanding the structural features of several dye systems. Chapter 2 will discuss some of the experimental techniques used in the NMR experiments, along with pertinent information about other analytical techniques used throughout the thesis.

In Chapter 3 the reader will be taken through the structural elucidation of a disperse azobenzene dyestuff. The phenomenon of polymorphism and molecular reorientation will be addressed, and how they manifest themselves in the NMR spectra of the ^{13}C and ^{15}N nuclei will be illustrated. Single crystal X-Ray data will be used to confirm the structures derived from the NMR study. Once the basic structures have been discussed, the kinetics of a large-amplitude dynamic reorientation will be analysed in Chapter 4 for one of the polymorphs of the same dye. A simple one-dimensional technique to measure exchange rates was used to obtain accurate estimates for the rate of inter-conversion.

In Chapter 5 the structures for a range of water-soluble sulphonic acid phenylazobenzene dyestuffs will be determined from ^{13}C and ^{15}N NMR. Tautomeric inter-conversion was found to occur upon protonation of the sulphonate group, and the three-dimensional structure in the crystalline-state suggests formation of dimers and/ or higher order-oligomers. Using the simple azobenzene dyes as model

samples allows one to extend the size of dyestuffs which can be investigated via solid-state NMR. A reactive dyestuff will be presented as a typical example of a large mono-azo dyestuff.

In Chapter 5 structures were discussed using the information obtainable from the isotropic shifts in the relevant NMR spectra. However, distinct advantages occur when one retains the anisotropic shielding and the direct dipolar coupling information. Chapter 6 will address this issue by analysing the spectral properties of ^{15}N NMR as applied to ^{15}N enriched samples. Nitrogen-15 rotational resonance spectra clearly demonstrate the reintroduction of the homonuclear ^{15}N - ^{15}N dipolar coupling which is removed by rapid MAS. Finally, in Chapter 7 a technique called PHORMAT will be presented which enables one to determine the principal components of the shielding tensor for systems which exhibit spectral congestion in one dimension.

References.

- 1 a/. E. R. Andrew and E. Szczesnaik, *Prog. Nucl. Magn. Reson.*, **28**, 11-36, (1995).
b/. J. W. Elmsley and J. Feeney, *Prog. Nucl. Magn. Reson.*, **28**, 1-9, (1995).
- 2 'Encyclopaedia of Nuclear Magnetic Resonance', eds D. M. Grant and R. K. Harris, Wiley, London, (1995).
- 3 J. Schaefer and E. O. Stejskal, *J. Am. Chem. Soc.*, **98**, 1030, (1976).
- 4 E. R. Andrew, A. Bradbury and R. G. Eades, *Nature*, **182**, 1659, (1958).
- 5 A. Hagemeyer, K. Schmidt-Rohr and H. W. Speiss, *Adv. Magn. Reson.*, **13**, 85, (1989).
- 6 R. A. Wind, M. J. Duijvestijn, C. van der Lugt, A. Manenschijn and J. Vriend, *Prog. Nucl. Magn. Reson.*, **17**, 33, (1985).
- 7 K. W. Zilm, selection of posters at ENC, Asilomar, 1996.
- 8 A. E. Bennett, C. M. Rienstra, M. Auger, K. V. Lakshmi and R. G. Griffin, *J. Chem. Phys.*, **103**, 6951, (1995).

2. Experimental

2.1 Sample Preparation and Characterisation.

Virtually all of the samples in this thesis were supplied by *Zeneca Specialties* from their fine-chemical collection. The three samples of ^{15}N -enriched DR278 were prepared by Dr. N. Hall at *Zeneca*. The β -labelled sodium sulphonate dyes used were synthesised using standard techniques, with $\text{NH}_4^{15}\text{NO}_2$ as a starting material for the preparation of the diazonium cation. The free acids were obtained from the sodium salts by recrystallisation from 1M aqueous hydrochloric acid solution. All samples were checked for purity by solution-state proton NMR and by mass spectrometry. Elemental analysis verified the presence of free acid, by the absence of sodium counterions, and allowed the determination of the degree of hydration.

The solid-state Raman and UV/ Vis spectra were obtained at *Zeneca* by Dr. G. Dent and Dr. D. Williams, respectively. For the DR278 samples polymorphic purity was determined by powder X-ray diffraction at the University of Durham by Dr. C. Lehmann, using a Philips PW 1050 diffractometer.

2.2 NMR.

Three spectrometer types were used in the present investigation;- a Chemagnetics CMX II, a Varian VXR and a Varian Unity Plus. The two Varian spectrometers operate at 300 MHz for protons and are for all intents and purposes identical. Three CMX II spectrometers were utilised which range in field strength from 100 MHz to 400 MHz. Every experiment carried out in this thesis involved the initial creation of enhanced spin-polarisation by the cross-polarisation technique, for the dilute spin system to be observed. This involves fulfilling the Hartmann-Hahn matching condition, which is generally obtained using suitable reference samples.

2.2.1 Magic-angle spinning (MAS).

The Chemagnetics probes used in the current investigation use pencil spinning modules with independent bearing and drive gas inlets. The supply gas is dry air which passes into an automated PID spin-rate controller which is capable of locking the spin rate to ± 5 Hz. This is essential for the careful and accurate analysis of the spinning sideband spectra to obtain shielding tensor information via the Herzfeld and Berger technique.¹ Typical spin rates used were in the range of 2 kHz to 6 kHz.

2.2.2 Variable Temperature Operation.

Several variable temperature experiments have been carried out and the experimental procedure varies between the two systems. The Varian spectrometers use Doty probes which have single bearings. The temperature of the bearing gas

(nitrogen gas when using VT) is modified by a heater which regulates the temperature that one wishes to require. For low-temperature experiments a heat exchanger is submerged in liquid nitrogen to cool the gas and the heater subsequently raises the temperature to the desired value.

For the Chemagnetics system there is a separate variable-temperature gas inlet which is totally independent of the bearing and drive gas lines. This improves the quality of the temperature stability in comparison to that obtainable by the Doty system, and allows for better spinning stability at lower temperature. In general the spinning gas is dry compressed air and the VT gas is nitrogen. A similar approach to maintaining the required temperature is applied as in the Varian system.

Due to the fact that the thermocouple is not directly at the sample, the system requires a calibration of the actual temperature. This can be carried out using several techniques, each of which has its failings. VT calibration is inherently difficult due to complications induced by the pressure effects (or frictional heating) which arise during MAS. Thus, ideally one would calibrate the system for each spinning speed, using a solid sample. At the time the spectra were recorded, the temperature dependence of the ^{13}C resonances within samarium acetate was used. These shifts vary according to a polynomial equation given by Haw *et al.*² The new method of choice would be that of the observation of the ^{207}Pb resonance in PbNO_3 which exhibits a linear shift dependence with temperature. Thermal gradients across the sample can also be determined by careful analysis of the observed lineshape. This has been shown to be a highly accurate technique over a large temperature range.^{3,4}

2.2.3 Observation of C-13

The primary objective for the observation of ^{13}C spectra is that of obtaining the maximum resolution possible. This is carried out by spinning fast enough to remove the effect of spinning sidebands and also by the application of sufficiently high-power proton decoupling. Typical decoupling powers correspond to a nutation frequency of around 60 kHz ($\pi/2$ pulse duration of $\sim 4\ \mu\text{s}$). The Hartmann-Hahn matching condition was determined by optimising the signal intensity for ^{13}C using adamantane under slow MAS conditions ($\sim 1200\ \text{Hz}$). Referencing was carried out by sample replacement, setting the high-frequency CH_2 resonance of adamantane to 38.4 ppm relative to TMS. Typical linewidths of adamantane were $\sim 4\ \text{Hz}$. The magic angle was set using the ^{79}Br resonance from KBr, by optimising the intensity of the rotational echos resulting from the first-order quadrupole interaction.

2.2.4 Observation of N-15.

For ^{15}N a 20% doubly-enriched sample of NH_4NO_3 was used for referencing (the high frequency NO_3^- line being referenced to $-5.1\ \text{ppm}$ relative to CH_3NO_2), setting the Hartmann-Hahn matching condition (using a spin rate of $\sim 2.5\ \text{kHz}$ and matching on the centreband) and also for setting the magic angle approximately. The angle is particularly important for ^{15}N work due to the huge shielding anisotropy for the systems under investigation. It was discovered that some of the ^{15}N -enriched azobenzene (and hydrazone) samples analysed were more sensitive to the angle than NH_4NO_3 , and as a result the angle could be set directly on the sample under investigation.

In this thesis the nitrogen scale used is that of the CH_3NO_2 . Significant discussion has centred around nitrogen referencing, and several people use the liquid ammonia scale, in which most resonances have positive δ . However, due to handling problems many people prefer to use the CH_3NO_2 scale, where most signals possess negative shifts.

2.2.5 Pulse Sequences.

For the observation of high-resolution solid-state NMR spectra application of simple CP/ MAS with flip-back⁵ was used in most cases. For these spectra a dead-time is required which results in the necessity for applying a first-order phase correction to the spectrum. To solve this problem the standard Hahn-echo sequence was applied. Removal of the decoupler for a short period, $\sim 40 \mu\text{s}$, removes the presence of protonated ^{13}C signals (with the exception of CH_3 signals, due to the rapid rotation about the C_3 axis) from the spectrum, which is known as interrupted decoupling. Subtraction of signals arising in the interrupted decoupling from those obtained using the Hahn-echo sequence, results in a spectrum which contains protonated signals only.

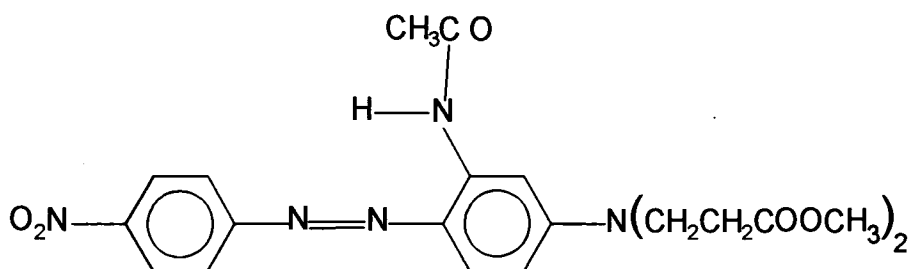
The Hahn-echo sequence is also used for the accurate determination of the powder patterns in the ^{15}N spectra under static conditions. The acquisition time was started exactly at the top of the spin echo to remove the effect of receiver dip. During static operation the purge and VT gas were used, each with flow rates of ~ 20 standard cubic feet per hour to maintain temperature stability within the probe body, and to reduce radio frequency heating.

References.

- 1 J. Herzfeld and A. Berger, *J. Chem. Phys.*, **73**, 6021, (1980).
- 2 J. F. Haw, G. C. Campbell and R. C. Crosby, *Anal. Chem.*, **58**,b 3173, (1986).
- 3 A. Bielecki and D. P. Burum, *J. Magn. Reson.*, **116**, 215, (1995).
- 4 L. C. M. van Gorkom, J. M. Hook, M. B. Logan, J. V. Hanna, R. E. Wasylshen, *Magn. Reson. Chem.*, **33**, 791, (1995).
- 5 J. Tegenfeldt and U. Haerberlen, *J. Magn. Reson.*, **36**, 453, (1979).

3. Analysis of the polymorphs of DR278.

The azobenzene dye Colour Index (CI) Disperse Red (DR) 278, 2'-acetamido-4'-[N,N-bis(2-methoxycarbonyl)ethyl]amino]-4-nitroazobenzene, (1), is a member of the class of disperse dyes used in the dyeing of polyester fibres. Monoazo dyes of this type are the single most important class of dye. Subtle changes in substituents at various positions are known to significantly influence the colour, tinctorial strength, dye-fibre affinity and the fastness properties.^{1,2} Visible spectroscopy in solution has shown that any intra-molecular hydrogen-bond formation can strongly influence the colour and solvent interactions generally affect the hydrogen-bonding nature of the system.³ This becomes important in an analysis sense because a large proportion of structural analytical techniques require the use of solvents, therefore, careful choice of solvents is essential. Additionally, the sorption process in which disperse dyes are generally thought to associate with polyester fibres assumes that the dyes are rigidly held within the pores of the fibre. Correspondingly, any technique that analyses the material in its natural solid state would hold distinct advantages over solution techniques.



(1) CI DR278

3.1 Information from traditional non-NMR techniques.

In the solid state this dye has three known crystalline states or polymorphs. Two of these polymorphs were reported to exist prior to the start of this project, but very little was known about their structure, particularly about the nature of any intramolecular hydrogen bonding that may be present. The polymorphs have been labelled as forms A, B and C according to the X-ray powder diffraction patterns shown in Figure 1. Form C is now currently in use by the *Zeneca* colours specialists, because it is thought to be the state of lowest free energy. Generally, differential scanning calorimetry (DSC) and X-ray powder diffraction are two of the methods of choice for the analysis of polymorphs,⁴ due to their ease and speed of characterisation of a particular material. DSC is particularly useful for the determination of phase changes and melting point determination. For example, one polymorph could spontaneously convert to another polymorph prior to melting. However these techniques do not give a means of obtaining structural information.

Infrared spectroscopy has, until recently, been the only tool for the analysis of the structure of these polymorphs. Resonance Raman and solid-state NMR are becoming particularly important because of advances in experimental design. In this section I shall attempt to solve the structure of all three polymorphs using solid-state NMR along with supporting evidence from the afore-mentioned techniques.

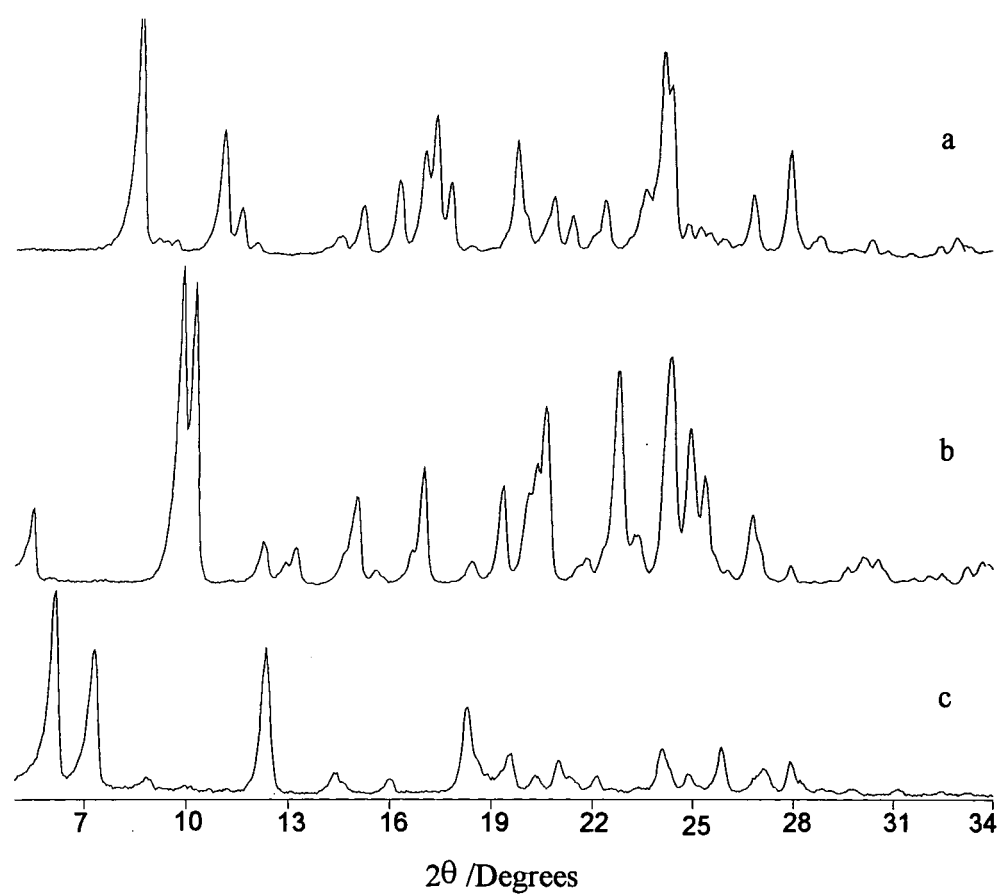


Figure 1
X-ray powder diffraction patterns for (a) polymorph A, (b) polymorph B,
and (c) polymorph C.

3.2 Elucidation of the solution-state structures.

Structural elucidation in the solid state via NMR is a formidable task and is probably a main factor in the lack of attention that it receives from organic chemists. Standard spectral editing techniques such as DEPT, homonuclear correlation and heteronuclear correlation cannot be readily applied to rigid solid materials,⁵ although certain research groups are pioneering spectral-editing techniques.^{6,7} The interrupted decoupling (see the introduction) pulse sequence is the only simple editing technique used universally. Spectral resolution is significantly reduced for a solid with ^{13}C resonances typically having linewidths of the order of 50 Hz. For this reason it was thought that a solution-state assignment for DR278 would simplify matters significantly prior to any solid-state analysis.

Solution-state ^{13}C spectra were recorded at 100.6 MHz on a Varian VXR 400 spectrometer using CD_2Cl_2 and $[\text{}^2\text{H}_6]\text{-DMSO}$ as solvents. The recycle delays were 2 s, with 1 s acquisition times. There are some significant differences between the two spectra as shown in Figure 2. Virtually all the peak positions have changed by at least 0.5 ppm and for the CD_2Cl_2 solution there appear to be fewer peaks. Closer examinations reveals the presence of two signals at 138.2 ppm and 129.4 ppm. The origin of such broadenings may be the presence of dynamic exchange between two (or more) conformers. Either raising or lowering of the temperature should then improve the quality of this spectrum. Without even assigning either spectrum it is obvious that one signal in each solution is strongly influenced by the choice of solvent *i.e.* 129.4 and 121.8 ppm in CD_2Cl_2 and $[\text{}^2\text{H}_6]\text{-DMSO}$ respectively.

With these initial observations made, a complete assignment could be carried out. This was possible purely by comparison with the assignments for other related molecules.⁸ Substituent chemical shift calculations are of some use in substituted azobenzenes, but are limited due to the modification of the electron density distribution in one ring by the substituents in the other ring. These effects are maximum at the *ipso* and *para* positions relative to the azo linkage. The assignments are made with the assumption that the azo linkage is present in the *trans* orientation, which indicates that each pair of *ortho* and *meta* resonances are inequivalent even for the C₆H₄NO₂ ring if the molecule is rigid. However, if rapid (on the NMR timescale) phenyl ring rotation occurs around the C1-N and/ or C1'-N bond(s) then motional averaging will simplify the spectrum significantly. The numbering scheme for the structure is given in Figure 3 and the corresponding assignments given in Table 1.

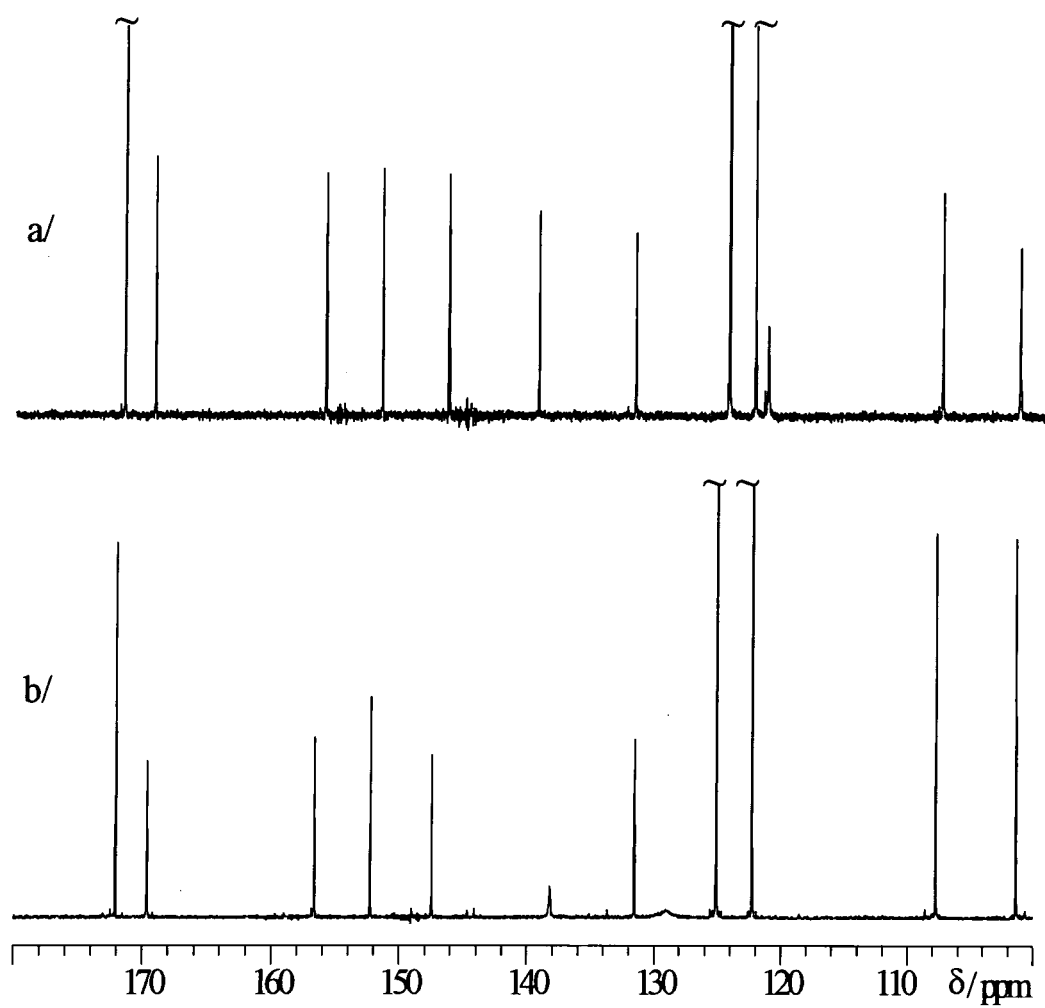


Figure 2

Room temperature solution-state ^{13}C spectra of DR278 recorded in a/ $[\text{}^2\text{H}]\text{-DMSO}$ and b/ CD_2Cl_2 . The “bump” at ~ 129 ppm in b/ is a real peak.

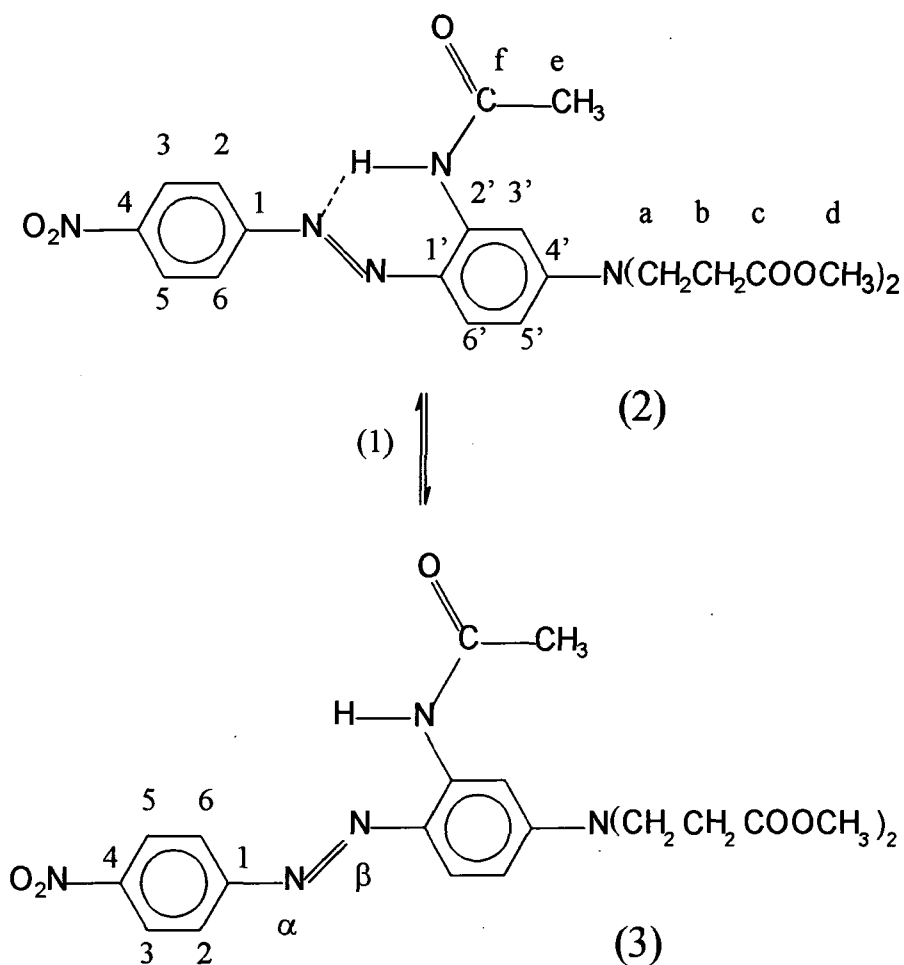


Figure 3

Dynamic equilibrium proposed for DR278 reorientation, with corresponding numbering scheme.

Rapid phenyl ring-flips are indeed present, with C2 and C6 giving one resonance at 122.3 ppm, while C3 and C5 similarly average to 124.5 ppm. Although the symmetry is lost in the other ring due to the presence of the acetamido group it is possible to verify that rapid ring rotation also occurs by analysis of the actual chemical shift values. The presence of an acidic proton on the acetamido group provides the opportunity for the formation of a six-membered ring via a N \cdots H—N

hydrogen bond.³ Sterically, the non-hydrogen-bonded conformer (3) is favoured, with the ortho substituent pointing towards the neighbouring nitrogen lone pair. To overcome the steric hindrance the N---H—N hydrogen bond must be sufficiently strong to compensate, and it becomes possible to have a dynamic equilibrium between the two conformers as shown in Figure 3. Visible spectroscopy has shown that the intramolecular hydrogen-bond strength is weaker for the acetamido case in comparison to the hydroxyl substituted derivative,³ as exemplified by the larger solvatochromic shift for the acetamido moiety. Therefore polar, basic solvents will hydrogen bond to the acidic amide proton, with DMSO being a typical example. UV/ visible spectroscopy for DR278 shows a 16 nm bathochromic shift (496 nm to 512 nm) in going from CD₂Cl₂ to DMSO solution. The large solvent dependency can be explained by interruption of the intramolecular hydrogen bonding by the DMSO molecule. This effect has been fully explained by Federov and co-workers⁹ for a range of similar azo dyes using solution-state NMR. However, I believe that his assignment regarding the shifts for C6' are rather confusing. Two papers^{8,9} analysing similar dyes give conflicting assignments. The latter (ref 9) is correct in my opinion. As a result the dye-solvent intermolecular hydrogen-bonding, which is favoured in DMSO, is associated with a low-frequency shift in the C6' resonance. This can easily be visualised by considering the equilibrium outlined in Figure 4.

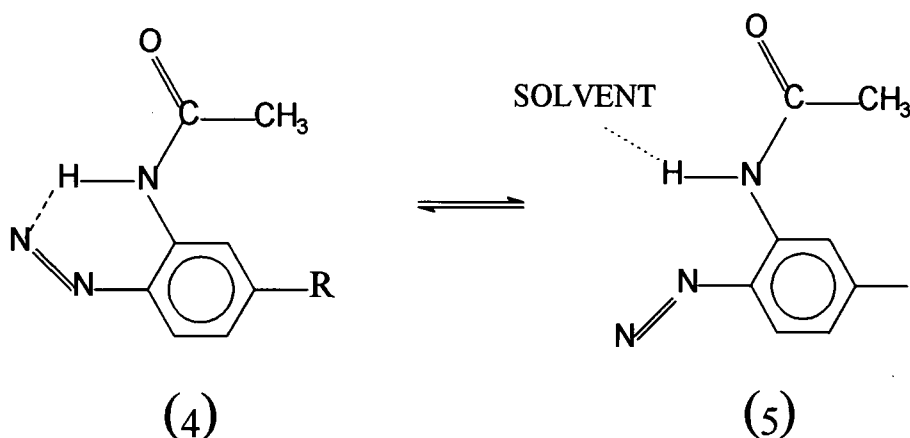


Figure 4

At ambient probe temperatures it is impossible to tell anything about the degree of solvation that this molecule may experience. This would require prior knowledge of the chemical shifts of conformers (4) and (5). This information can be obtained by carrying out a low-temperature spectrum. This was indeed done in the CD_2Cl_2 solution at -80°C . Figure 5 gives the spectrum obtained at the reduced temperature, and it can clearly be seen that there are two conformations present, with approximately equal proportions. The low-temperature shifts and assignments are given, along with the room temperature assignment, in Table 1. The actual extreme values for the two $\text{C6}'$ signals are 138.3 ppm and 116.9 ppm for conformers (4) and (5) respectively. From these low-temperature results we can see that 58% of the material is present as conformer (4) in CD_2Cl_2 solution, while only 23% is present as conformer (4) in DMSO solution, as calculated by:

$$Fraction(2) = \frac{\delta C6'_{iso} - \delta C6'_{(3)}}{\delta C6'_{(2)} - \delta C6'_{(3)}}$$

where $\delta C6'_{(3)}$ and $\delta C6'_{(2)}$ are the chemical shifts of C6' in the -80° spectrum and $\delta C6'_{iso}$ is the observed shift at room temperature. The references to conformations 2 and 3 have been used because that is the scheme which contains the numbering of the nuclei.

Again, these results give significant evidence that DMSO strongly solvates the dye. These mole fractions, as obtained from the shift values, roughly relate to the relative intensities of the two conformations in the low-temperature spectrum. Indeed, several of the shifts were assigned on the basis of intensities, the small changes in shifts being insufficient to confidently assign signals to a particular conformer. It must be remembered, however, that no intrinsic shift change as a function of temperature has been accounted for. Carrying out the same calculation as above, but using C2', gives 40% and 16% respectively. Both are consistently lower by a factor of *ca.* 3/2 which suggests that the isotropic thermal effects on these two shifts are in opposite directions. Thus averaging the two results will give a rough estimate of the molar fraction of (2). *i.e.* 50% and 20% in the two solutions. Even at -80°C phenyl ring-flips on the nitro substituted ring are still fast, producing only averaged shifts. The origin of the small splittings observed is a result of the slight modification of electron density around the rings by the formation of the hydrogen bond, probably due to the change in conjugation around the azo linkage.

Carbon	δ / ppm (Solution)			
	CD ₂ Cl ₂		[² H ₆]-DMSO	
	20 °C	-80°C		20 °C
		(2) ^a	(3)	
1	156.6	154.8	155.9	156.2
2,6	122.3	121.0	122.0	122.8
3,5	125.1	124.5		124.8
4	147.5	145.9	146.1	146.7
1'	131.6	129.6	130.5	132.1
2'	138.2	134.6	140.6	139.7
3'	101.4	99.6		102.0
4'	152.3	150.9	151.6	151.8
5'	107.8	106.6	107.	108.1
6'	129.4	138.3	116.9	121.8
	(broad)			
a	47.4	46.3		46.4
b	32.4	31.1		31.6
c	172.1	171.9		171.6
d	52.1	52.0		51.6
e	25.8	25.4	25.8	24.8
f	169.7	168.6	170.3	169.3

Table 1

Solution-state assignments for ¹³C spectra of I in solution, given in ppm relative to the signal for TMS.

^a *The more intense peaks are assigned to this conformer.*

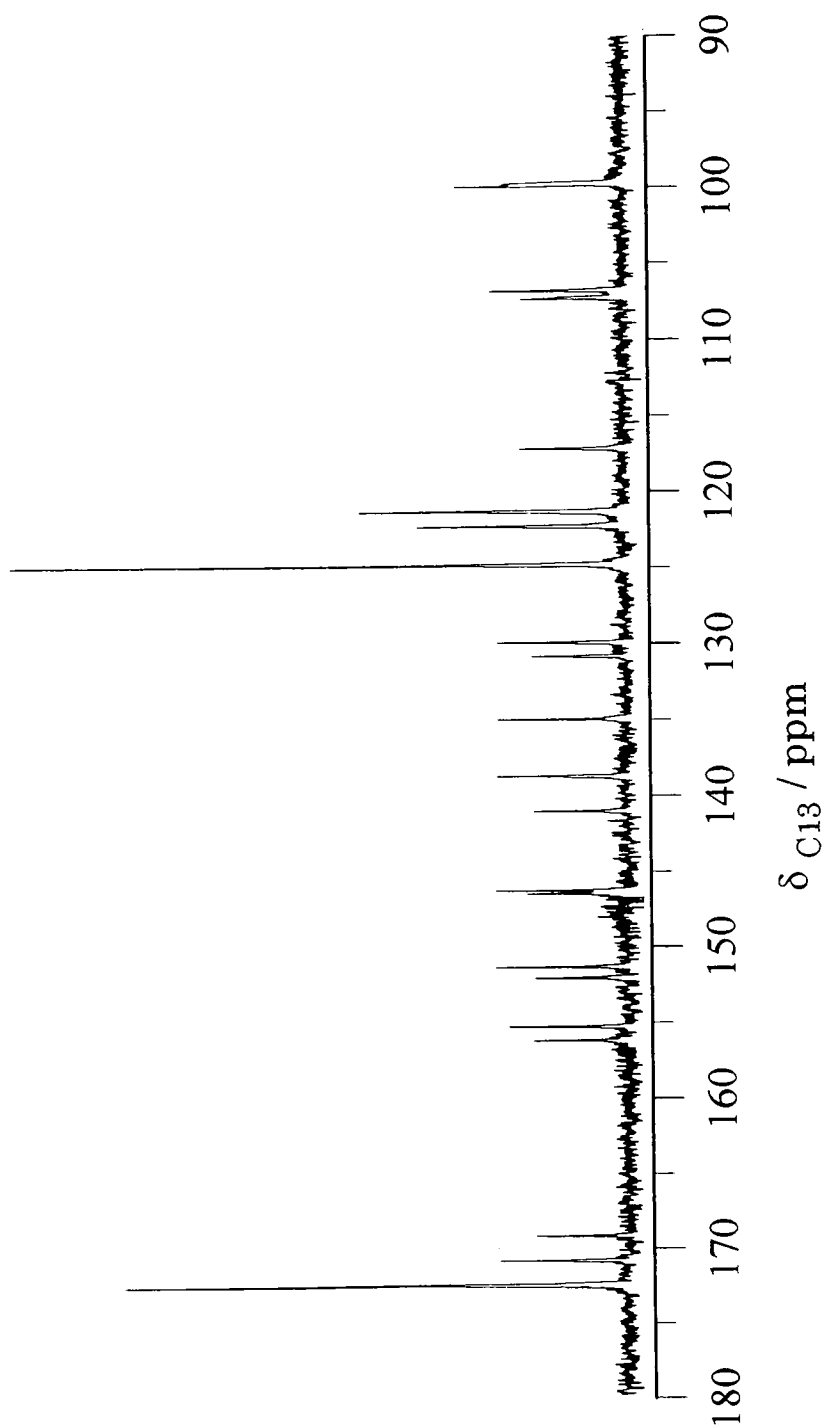


Figure 5

^{13}C solution-state spectrum recorded in CD_2Cl_2 at -80°C .

The presence of two conformations can clearly be seen by the doubling of all peaks.

3.3 Solid-state structures of the polymorphs of DR278.

3.3.1 Carbon-13 NMR.

With a complete understanding of the solution-state structures and of the effect that the azo linkage has upon the aromatic signals, a solid base has now been established for the analysis of the polymorphs in their natural state. All three polymorphs were packed into the rotors without any form of grinding or crushing. It has been shown by Maciel¹⁰ that grinding can cause changes in the SSNMR spectra of polymorphic forms. Differences in resonance Raman spectra can also result from grinding with KBr, and hence nujol mulls are often preferred. Cross polarisation with magic-angle spinning was employed to obtain high-resolution ¹³C spectra for all three polymorphs, Figure 6. At first inspection it would appear that, although some spectral features are similar, there are significant differences between the solid-state and room-temperature solution-state spectra. Also, when comparing the three polymorphs, the spectra again vary quite dramatically. It is clear from the complexity of the spectra, and from comparison with the low-temperature solution-state spectra, that polymorphs A and B contain conformationally different molecules in the crystal lattice, with non-integral intensity ratios. This is a most unusual situation for a single crystalline form, let alone for two distinct polymorphs.

At ambient temperature it is clear that the linewidths for all three polymorphs are different, with form C giving the narrowest resonances. This is the structure which is believed to exist as a single molecular entity in the crystal state, given the relative simplicity of the spectrum. With the observation of 12 aromatic signals it is

evident that the C2,C6 and C3,C5 pairs of signals are no longer averaged in this sample. Hence, phenyl ring rotation is hindered and the group is locked in a fixed orientation relative to the azo linkage. Chippendale *et al.*¹¹ analysed this effect in a similar series of compounds. The parent molecule, *trans*-azobenzene, showed that the C2-C6 splitting is around 13 ppm, while the C3-C5 splitting is far smaller, to the extent that no observable splitting can be detected unless narrow lines are observed. However, a splitting of 3 ppm was observed (ref. 11) for C3-C5 and suggested to be typical of that which would generally arise from these meta ¹³C signals. With the solution-state spectra of DR278 and the information regarding locked conformations, the signals for polymorph C could be assigned, Table 2, and are thought to arise from a purely non-hydrogen-bonded molecule. C6' and C2' produce resonances at 118.4 ppm and 140.5 ppm respectively, close to the values found for conformer 3 in the low-temperature spectrum. Additionally it should be noted that the signals assigned to C1' and C3' deviate from their solution shifts by approximately 4 ppm to higher frequency. This is probably due to the acetamido group being fixed out of the plane of the aromatic ring, introducing a steric contribution to the shift for these resonances. This out-of-plane rotation is only possible for molecules in the non-hydrogen-bonded conformer.

The situation is more complex for the other two polymorphs which is primarily due, as suggested before, to the reduced spectral resolution. If two conformers mutually exchange then any broadening would be expected to be less at a higher static field strength. Also, with the presence of several ¹⁴N nuclei it is possible to experience residual dipolar coupling¹² of the quadrupolar nucleus to the directly bonded ¹³C, which is again reduced at higher field strengths. With this

supposition, ^{13}C CP/MAS spectra were recorded at 50 MHz and 75 MHz for both polymorphs. The 50 MHz spectra are shown in Figure 6, and the 75 MHz spectrum for polymorph B is shown for comparison in Figure 7. Interrupted-decoupling spectra were recorded to select the non-protonated aromatic carbon signals, and the corresponding difference spectra with only the aromatic CH signals selected can also be obtained. A representative interrupted-decoupling spectrum is shown with its corresponding difference spectrum in Figure 8.

A significant resolution-enhancement is observed in moving to the higher field, and the small peaks which appear as “bumps” in the baseline at 50 MHz can clearly be observed. These peaks correspond to the minor contribution arising from C2' and C6' and can therefore be assigned to the non-hydrogen-bonded conformation (2). The relative intensities of each pair will give an estimate of the populations of the two conformers present in each polymorph. Thus we see that polymorph A is present with a 50:50 ratio of the two conformations, while polymorph B contains ~80:20 ratio in favour of the hydrogen-bonded conformer. Variable-temperature analysis of these samples show significant changes in the spectral features due to the expected conformational averaging of the C2(6), C2' and C6' pairs. Analysis of the spectra at these elevated temperatures proved rather difficult due to the complexity of the spectra and poor signal-to-noise of the exchanging lines. In an effort to analyse the motional processes involved it was decided that the ^{15}N nucleus would be used as a probe.

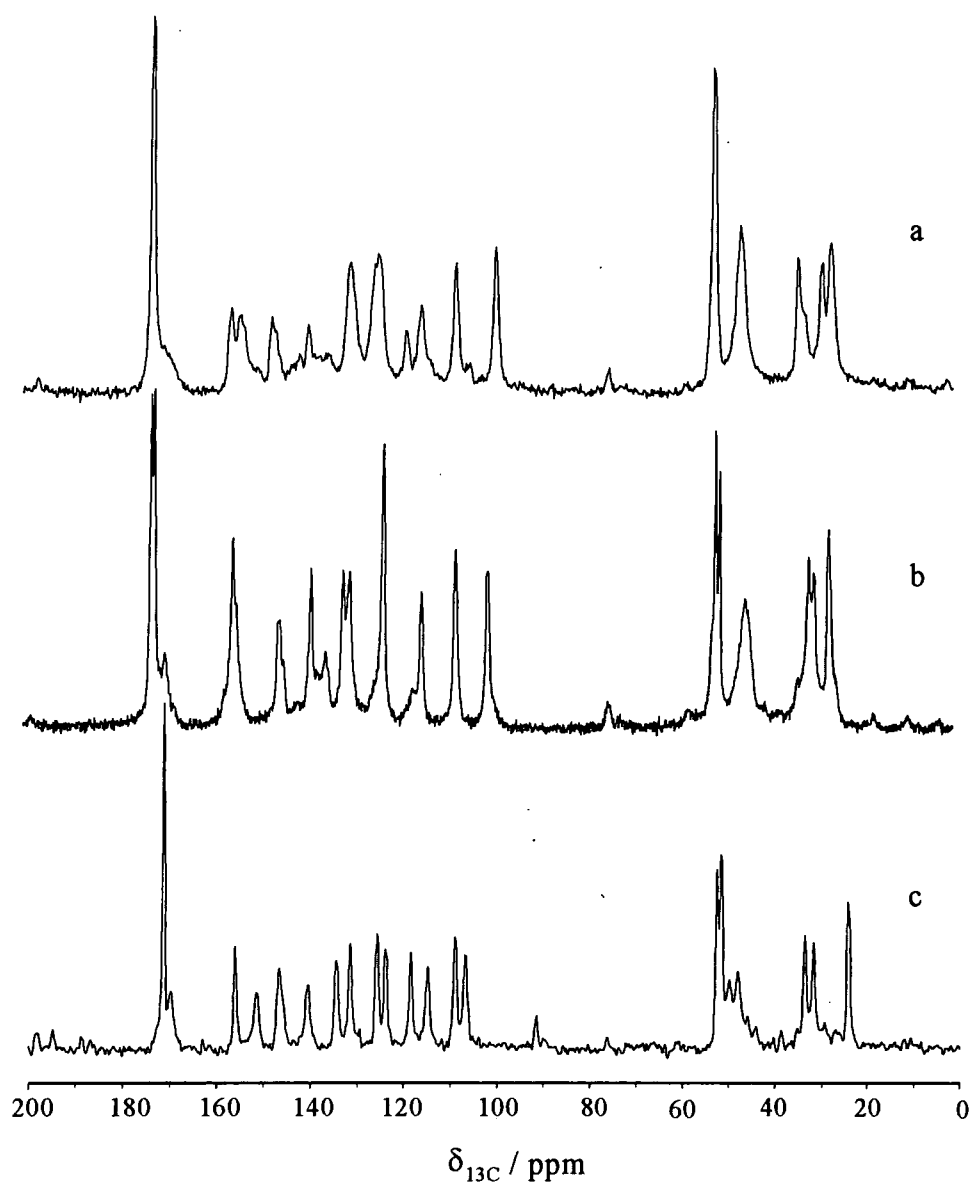


Figure 6

¹³C CP/MAS spectra of a/ polymorph A, b/ polymorph B and c/ polymorph C. All spectra were recorded at 50 MHz, with typical acquisition parameters of; a 7 ms contact time, a 30 s pulse delay for A and B, and 5 s for C, and between 600 and 1000 transients. Spin rates of ~4.5 kHz to 5.5 kHz were applied.

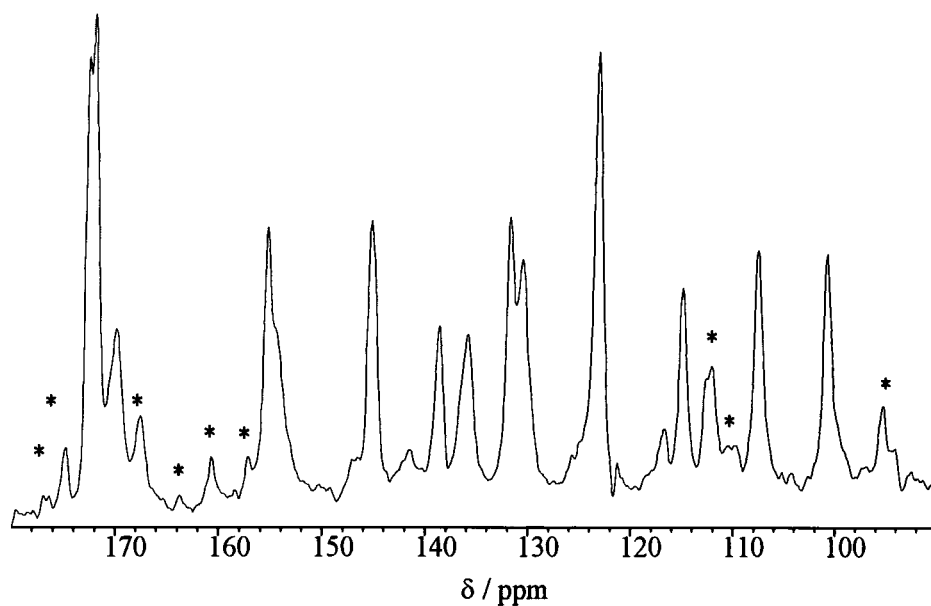


Figure 7

^{13}C CP/MAS spectrum of DR278 at 75 MHz for polymorph B.

* indicates spinning sidebands.

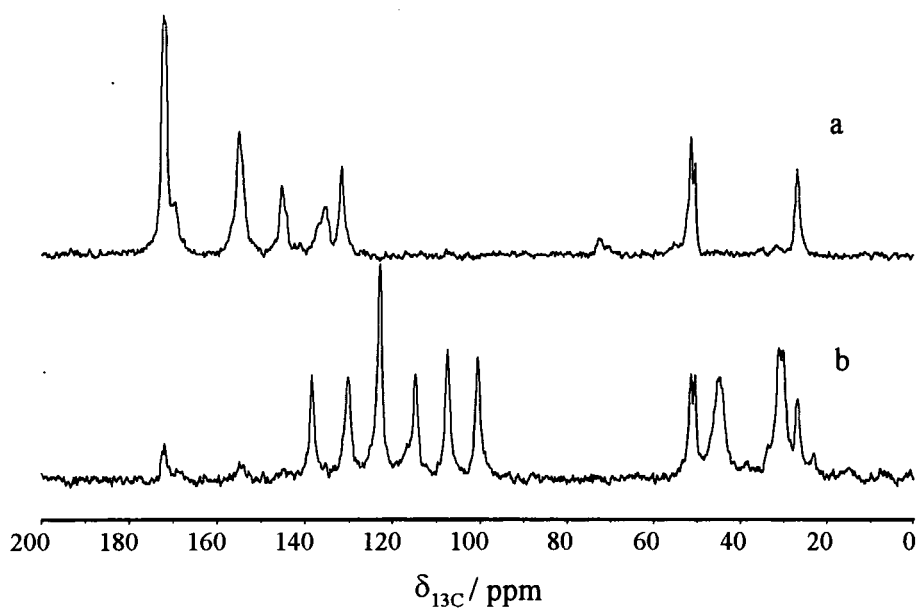


Figure 8

^{13}C CP/MAS a/ interrupted-decoupling and b/ difference spectra for polymorph A. The decoupler was switched off for a duration of 40 μs to allow removal of the aromatic CH signals. Standard acquisition parameters were used as in the caption for Figure 6.

Carbon	δ / ppm (Solid)		
	Polymorph A	Polymorph B	Polymorph C
1	155.7	155.3	156.0
2	130.5	130.3	131.4
6	114.9	115.0	114.9
3,5	124.2	123.0	123.8
			125.7
4	147.0	145.3	146.7
1'	130.0	131.7	134.4
2'	141.4	141.5 #	140.5
	135.2	135.9	
3'	99.0	100.8	106.7
4'	153.7	155.3	151.4
5'	107.5	107.6	109.0
6'	138.8	138.7	118.4
	117.9	116.7 #	
a	46.0	45.2	49.9
			48.2
b	33.8	31.3	33.7
	28.6	30.5	31.8
c	172.6	172.6	171.4
		172.1	
d	51.9	51.6	52.6
		50.7	51.9
e	26.6	27.0	24.3
f	170.0	169.7	169.8

Table 2

Solid-state ^{13}C assignment for the spectra of the polymorphs for DR278.

Shifts are given in ppm relative to TMS. The minor conformer is

indicated by the # for polymorph B.

3.3.2 Nitrogen-15 NMR.

The ^{15}N nucleus is a useful probe for the analysis of azobenzenes because of the large shielding anisotropy of the azo nitrogen sites. Wasylshen¹³ has reported that pure *trans*-azobenzene has a chemical shift span of over 1000 ppm, one of the largest known for nitrogen. Hence, both the anisotropies and the isotropic shifts should be sensitive to the local environment. Also, with its low magnetogyric ratio, couplings to other nuclei will be weak in comparison to those for carbon, which will result in a virtually isolated spin. On the down side is the fact that it has a very low natural abundance which limits the application of natural abundance ^{15}N NMR to samples which have short T_{1H} and long T_{1p} , allowing fast repetition of the acquisition and long contact times to be employed. Possession of a large SA is not beneficial in this case because the signal intensity is spread over many sidebands, reducing the chance of observing the relevant isotropic signal. Fast MAS is thus required to remove as many sidebands as possible, as shown for form C in Figure 9. Observation of the azo nitrogen signals is possible only because of the very high number of transients used and this is certainly not a typical ^{15}N spectrum. A poorer signal-to-noise ratio still allows the secondary and tertiary amines to be observed for form B, as these have very small shielding anisotropies which have been effectively spun out at the speeds used. No azo nitrogen signals appear, however. Thus if a proper analysis is to be carried out then isotopic enrichment with ^{15}N must be used. The isotropic ^{15}N shifts for the solid and solution states are given in Table 3.

Isotopic enrichment of the α and β positions of the azo linkage produced three samples of polymorph A:-

a/ α singly-labelled sample

b/ β singly-labelled sample

c/ α and β doubly-labelled sample

The two singly-labelled samples are essentially ^{14}N - ^{15}N isolated heteronuclear spin pairs, while the doubly-labelled sample is a ^{15}N - ^{15}N isolated homonuclear spin pair. Probing the dipolar couplings between these two nuclei would intuitively provide information regarding the structure of the azo bond. The ^{15}N spectra, showing the isotropic chemical shifts, are given in Figure 10 for these three samples.

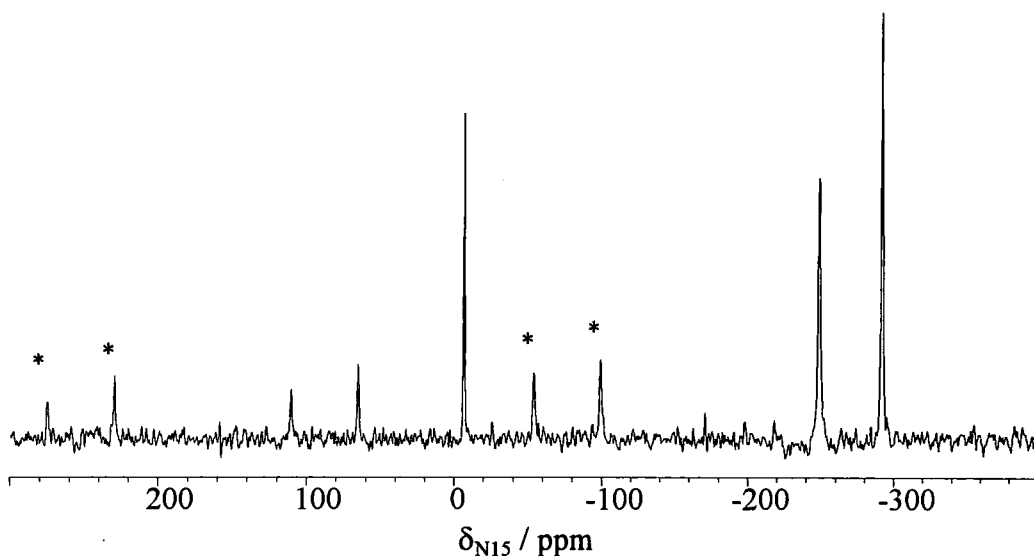


Figure 9

Natural abundance ^{15}N spectra of DR278 form C at 30 MHz and a spin rate of 5 kHz. * indicates spinning sidebands.

δ_N / ppm	SOLID		SOLUTION	
	Polymorph			
Nitrogen	B	C	D ₆ DMSO	CDCl ₃
N _{α}		60.0	62.3	
N _{β}		105.4	111.3	
NO ₂	-13.6	-11.7	-11.9	-13.2
NHCOCH ₃	-248.8	-254.1	-254.7	-253.9
N(CH ₂ -----)	-290	-297.3	-294.4	-294.7 (very weak)

Table 3

¹⁵N chemical shift assignment of polymorphs B and C at natural abundance. The N _{β} signal for polymorph C was taken from the labelled sample.

Polymorph A should produce two signals of approximately equal intensity in the ¹⁵N CP/MAS spectra for each of the two singly-labelled samples. This was indeed the case, providing irrefutable evidence that two conformations exist, with peaks being observed at 121 ppm and 89 ppm for the β label, and at 60 ppm and 44 ppm for the α label. A two-dimensional chemical shift / dipolar correlation experiment could not distinguish between the two sites for either sample on the basis of differing N-H dipolar coupling and the chemical shifts are too close to be able to assign them. This is as expected for the β site due to the very similar environments of the two sites. However, it was hoped that the hydrogen-bonded proton would be

sufficiently close to allow a dipolar coupling to be realised for the hydrogen-bonded conformation in the α label sample. Additionally, the ^{14}N - ^{15}N spin pairs for the singly-labelled materials show no evidence of residual dipolar coupling at room temperature. This phenomenon will be discussed later. The spectrum of the doubly-labelled sample appears to be simply a superposition of those for the two singly-labelled samples, with no observable dipolar coupling under MAS. The fact that the chemical shifts are far enough removed from each other should allow a complete kinetics analysis to be carried out. First though it would be useful to obtain a chemical shift assignment for the four signals.

This assignment was obtained from two new pieces of information. Firstly, the β -labelled sample was converted to form C, which is already known to exist in the purely non-hydrogen-bonded conformation. A single peak at 105.4 ppm was observed for this sample in the ^{15}N CP/MAS spectrum. Strangely, this does not coincide with either of the two shifts in the form A spectrum, 121 ppm and 89 ppm, as these shifts are thought to represent the values for the two possible conformations. The natural abundance signals could be observed in the labelled spectrum, and gave the same shifts as for the natural abundance sample. With the extra sensitivity and narrower lines the shifts could be extracted more accurately. From comparison with the spectrum of the α labelled sample the resonance at 60 ppm could be assigned to the non-hydrogen-bonded conformer. This only leaves the β sites to be assigned.

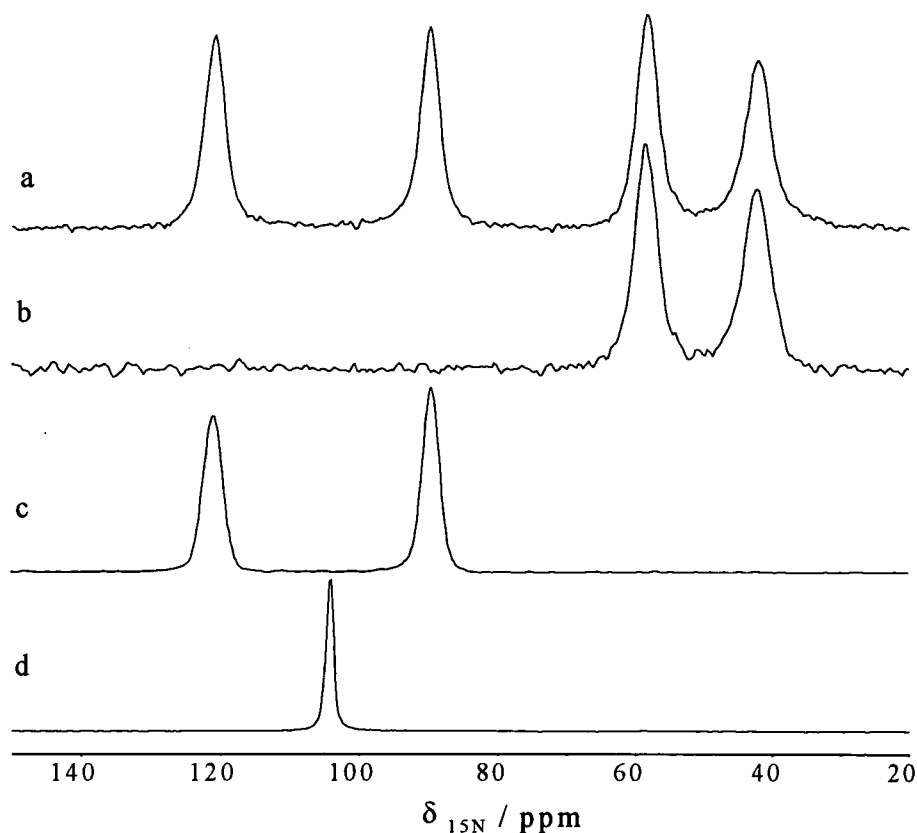


Figure 10

Comparison of the ^{15}N CP/MAS spectra for the labelled samples of polymorph A. a/ α,β double label, b/ α single label, c/ β single label and d/ β single label of polymorph C.

The second tool in this assignment is the application of rotational resonance to the ^{15}N spin-pair in the doubly-labelled sample of polymorph A. Generally this technique is used to obtain non-bonding internuclear separations in molecules with a view to understanding conformations in the solid state.¹⁴ Upon matching the spin rate with the isotropic chemical shift difference (expressed in Hz) of two homonuclear coupled spins, a splitting will be observed which is dependant upon the direct dipolar coupling constant. The rotational resonance spectrum, Figure 11, for the 121 ppm and 44 ppm signals provides the proof that these two lines are directly

bonded and are present in the molecule at the same time. Similarly matching the spin rate to the 89 ppm, 60 ppm spin-pair produced an equivalent splitting, while the 121 ppm, 60 ppm spin pair did not show any splitting at their rotational resonance condition, proving that the nuclei contributing to the signals at 121 ppm and 60 ppm are not coupled.

The only curiosity that remains to be answered is the apparently anomalous shift for the β signal of form C. A non-planar orientation of the acetamido group, as suggested for the ^{13}C spectra, would only affect the β site in this non-hydrogen-bonded conformation. The α site would be significantly spatially removed from the amide nitrogen lone pair so that it is not affected.

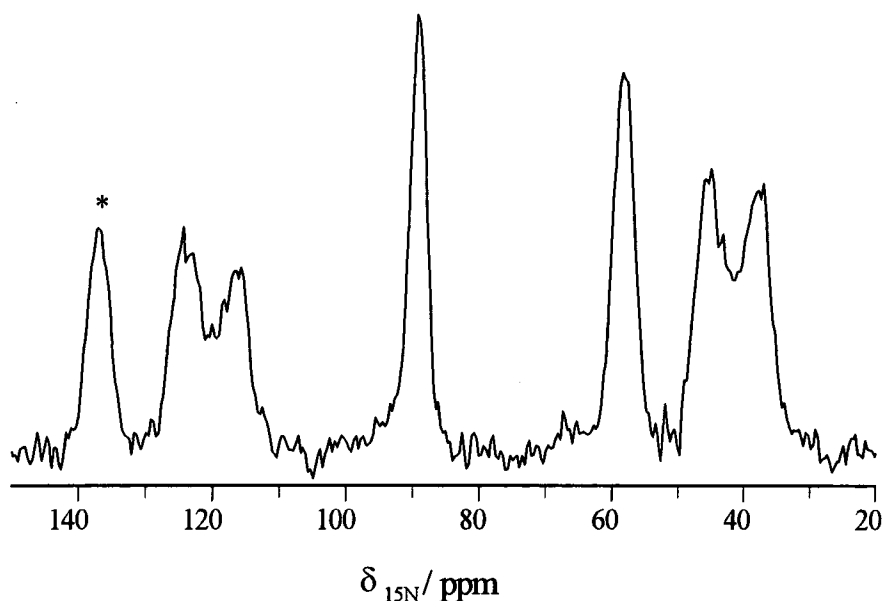


Figure 11

^{15}N rotational resonance ($n=1$) spectrum for the doubly labelled sample of polymorph A. Selecting only the hydrogen bonded spin pair.

* indicates spinning sideband.

Conclusion.

It has been shown that a complete assignment of the ^{13}C solution and solid-state spectra for DR278 can give information regarding the local molecular environment of the system. The solution-state spectra are profoundly influenced by the particular choice of solvent which gives clear evidence that the hydrogen bonding network is being interrupted by the solvent. In the solid phase the different polymorphs can be considered to be composed of two conformations, which can undergo molecular reorientation, in different proportions. As to how the total free energy of the system relates to the local structures is at the moment unclear.

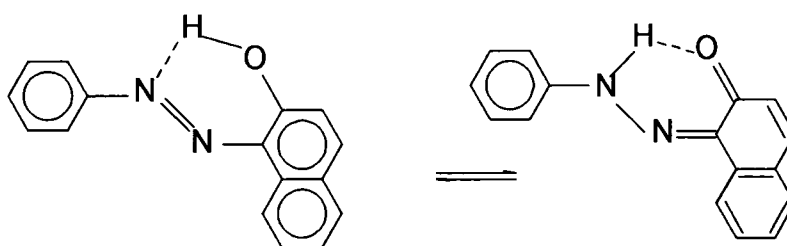
The ^{15}N NMR spectra verify the supposition of the presence of two conformations and with the application of rotational resonance a full assignment of the signals for all the samples can be made.

References.

- 1 H. Zollinger, *Colour Chemistry; Syntheses, Properties and Applications of Organic Dyes and Pigments*, 2nd Ed, VCH, (1991).
- 2 W. Biedermann, *J. Soc. Dyes Colour.*, **87**, 105, (1971).
- 3 P. Gregory and D. Thorp, *J. C. S. Perkin Trans I*, pp1990, (1979).
- 4 T. L. Threlfall, *Anal.*, **120**, 2435, (1995).
- 5 A. Bax, *Two-Dimensional Nuclear Magnetic Resonance in Liquids*, Delft University Press, Delft, (1982).
- 6 X. Wu and K. W. Zilm, *J. Magn. Reson.*, **102**, 205-213, (1993).
- 7 R. Sangill, N. Rastrup-Andersen, H. Bildsoe, H. J. Jakobsen and N. C. Neilsen, *J. Magn. Reson.*, **107**, 67-78, (1994).
- 8 P. Savarino, G. Viscardi, E. Barni, R. Carpignano, L.A. Federov, *Dyes and Pigments*, **13**, 71, (1990).
- 9 P. Savarino, G. Viscardi, E. Barni, R. Carpignano, L.A. Federov, V. I. Dostovalova, *J. Struct. Chem.*, **33**, 6, 844-852, (1992).
- 10 G. E. Maciel, N. M. Szeverenyi and M. Sardashti, *J. Magn. Reson.*, **64**, 365, (1985).
- 11 A. M. Chippendale, A. Mathias, R. K. Harris, K. J. Packer, B.J. Say, *J.C.S. Perkin Trans II*, 1031, (1981).
- 12 S. H. Alarcón, A. C. Olivieri and P. Jonsen, *J. Chem. Soc. Perkin Trans. 2*, 1783-1786, (1993).
- 13 R. D. Curtis, J. W. Hilborn, G. Wu, M. D. Lumsden, R. E. Wasylshen and J. A. Pincork, *J. Phys. Chem.*, **97**, 1856, (1993).
- 14 M. H. Levitt, D. P. Raleigh, F. Creuzet and R. G. Griffin, *J. Chem. Phys.*, **92**, 6347, (1990).

5. Investigation of Tautomerism in Sulphonic Acid Azobenzene Derivatives by C-13 and N-15 NMR.

The systematic analysis of azobenzene dyestuffs by NMR, particularly in the solid state, has been limited to a small range of dyes. Disperse dyes constitute the majority of the work done on substituted phenylazobenzenes, while phenylazonaphthols have also received significant attention, which is in part due to the presence of rapid proton transfer in the solution state, and also in the solid state. The resultant system is thought to yield a well defined double-well potential-energy surface. Theoretical chemists trying to understand these proton transfers require accurate experimental evidence to validate their ab-initio studies. The proton transfer in phenylazonaphthols results in a tautomeric change in the structure of the dye, with the naphthol OH proton transferring, back and forward, between the azo group and the hydroxyl group, resulting in an equilibrium between the enol / azo and keto / hydrazo structures as shown in Scheme 1. Jonsen and co-workers^{1,2} and Lycka³ have utilised both ¹⁵N and ¹³C CP/MAS NMR in the solid state to probe the tautomerism of these phenylazonaphthols.



Scheme 1

4. Kinetics Analysis of a Large-Amplitude Reorientation.

4.1 Introduction.

Large amplitude reorientations of the type suggested in the previous section are rather uncommon in the solid state. Phenyl ring rotation is common place, but with the acetamide group attached rotation of this ring is unlikely to proceed. Three plausible mechanisms for the motional process exist. One suggestion is that two independent phenyl ring rotations around the central azo linkage occur. Secondly, a complete crankshaft motion of the aromatic rings around the C1'-N and C1-N bonds of the azo linkage, while keeping the two aromatic rings approximately co-planar at all times, could occur. This second proposal requires far less free volume to proceed and is thought to be a more likely mechanism. The third proposal involves an in-plane inversion of the azo linkage, similar to *cis-trans* isomerisation.¹ It should be noted, however, that the transition-state structure is likely to be identical for the first two mechanisms with the aromatic rings orientated perpendicular to the azo linkage. The transition state of the *trans-trans* inversion is generally believed to be linear around the azo linkage in the crystal state. The co-planarity requirement must hold if the crystal is held together by π - π intermolecular interactions (as suggested by the crystal structure).¹

I. Additional crystal structure information is given in the addendum.

A crystal structure determination, recently obtained, was solved by considering that there are two orientations of the azo linkage, and also two positions of the benzene ring with the nitro group attached. This determination showed a significant degree of disorder within the molecule, with the two configurations having approximately equal populations. The presence of these two conformations is shown below in Figure 1. Figure 1 shows that the two structures occupy virtually the same space within the lattice. Consideration of the molecular packing would intuitively provide more information for one to propose a mechanism for any motional rearrangement.

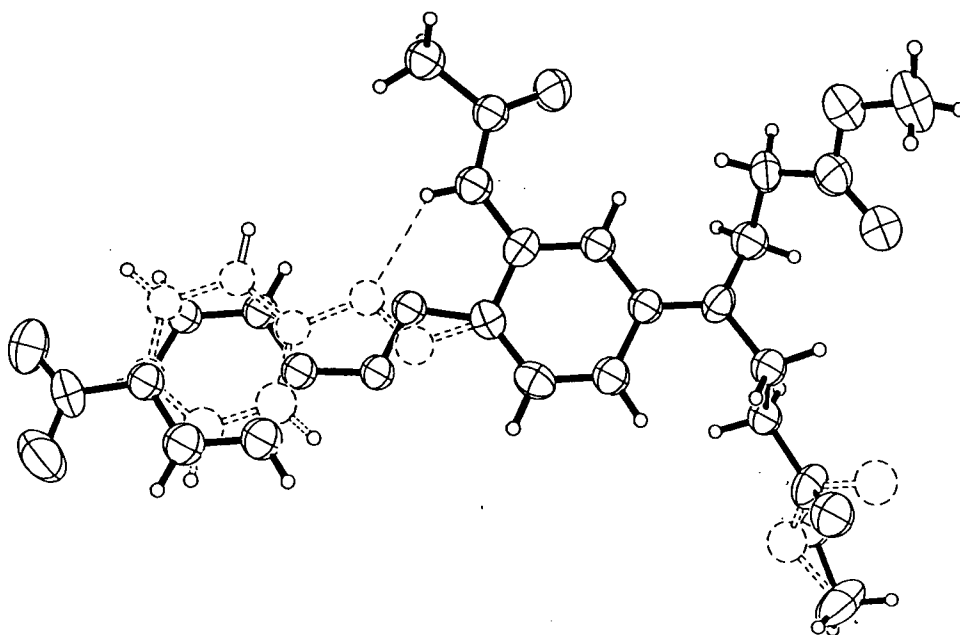


Figure 1

Single crystal X-ray derived molecular structure for DR278 A. Thermal ellipsoids are shown at 30 % probability for clarity.

X-ray crystallography cannot determine the origin of such disorder, be it static, long range or motional. It merely detects the fact that over a large collection of atoms, and over a long time, there is a distribution of electron density which is not attributable to one single well-defined molecular environment. The NMR evidence has, however, shown that at least some of that disorder is motional in nature, as discussed in the previous chapter. In this chapter a complete understanding of the kinetics process within polymorph A of DR278 will be presented.

NMR has proven to be an invaluable tool for the analysis of dynamic processes, particularly those which involve equilibria or where simple intramolecular motion is present.²⁻⁵ In this branch of NMR, which is known as dynamic NMR (DNMR), it is possible to probe molecular reorientation, conformational change, or chemical reactions by a variety of experimental techniques. The choice of technique depends upon the rate of the exchange process in relation to the observable features in an NMR spectrum. By utilising the appropriate experiment it is possible to probe processes where the first-order, or pseudo first-order, rate constants span the range 10^{-2} Hz to 10^8 Hz. The upper limit given here is for processes which produce efficient pathways for spin-lattice relaxation⁶ and $T_{1\rho}$ relaxation.⁷ Accordingly these motions interact with the static field and applied RF field in the range of 10^8 Hz to 10^4 Hz. Additionally, any coherent perturbation applied to the system, be it pulses or CW irradiation, can interfere with the motional processes inherently present. As a result it is possible to observe significant broadening of the solid-state NMR signal when the motion interferes with the decoupler field,^{8,9} the cycle time in multiple pulse experiments such as CRAMPS and also the spin rate of the rotor,¹⁰ even well above the

Rothwell *et al.*¹¹ These fast motional processes include methyl rotation about the C₃ axis, aliphatic chain rotation and proton tunneling involved in tautomeric equilibria. Typically rotor spin rates and decoupler fields are in the kHz to 100's of kHz range. To monitor slower processes it is possible to apply magnetisation transfer sequences¹² and to use the bandshape analysis technique.² Both of these last two techniques shall be considered in greater detail in the following sections.

Bandshape Analysis.

When the exchange rate between two chemically shifted signals is of the order of the separation of the two resonances then it is possible to observe a broadening of the signals. Initial studies of the resultant lineshapes in solution were initially carried out by considering an uncoupled two-spin system and solving for the transverse components of the exchange-modified Bloch equations. The final expression was derived by Rogers and Woodbrey:¹³

$$v = -C_0 \frac{\left\{ P \left[1 + \tau \left(\frac{p_B}{T_{2A}} + \frac{p_A}{T_{2B}} \right) \right] + QR \right\}}{P^2 + R^2} \quad (1)$$

where,

$$P = \tau \left[\frac{1}{T_{2A} \cdot T_{2A}} - 4\pi^2 \Delta v^2 + \pi^2 (\delta v)^2 \right] + \frac{p_A}{T_{2A}} + \frac{p_B}{T_{2B}}, \quad Q = \tau [2\pi \Delta v - \pi \delta v (p_A - p_B)]$$

$$R = 2\pi \Delta v \left[1 + \tau \left(\frac{1}{T_{2A}} + \frac{1}{T_{2B}} \right) \right] + \pi \delta v \tau \left(\frac{1}{T_{2A}} - \frac{1}{T_{2B}} \right) + \pi \delta v (p_A - p_B)$$

$$\tau = \frac{p_A}{k_A} = \frac{p_B}{k_B}, \quad v = \nu_A - \nu_B, \quad \Delta v = 0.5(\nu_A + \nu_B) - \nu$$

where T_{2i} , ν_i and p_i are the transverse relaxation times, frequencies and fractional populations of the i th resonance, k_i are the exchange rate for the process i to j .

In the solid state, however, one must be very careful in the method of analysis. Schmidt *et al*¹⁴ discussed the exchange-broadened lineshapes in the solid state under magic-angle-spinning by the application of Floquet theory. Essentially, the simple theory previously mentioned cannot be applied to a system where spectral overlap occurs due to the presence of shielding or dipolar sidebands.

The ^{15}N CP/MAS spectrum of the β -labelled sample of DR278 II at room temperature shows no evidence of exchange broadening. Upon increasing the temperature, significant broadening is observed, with the coalescence temperature at approximately 80 °C. Due to the low melting point of this sample the maximum temperature recorded was 90 °C. The error in the estimate of the rate constant is significant when there is very little exchange broadening of the line, which proved to be a problem below 40 °C. As discussed previously it is desirable to reduce the presence of sidebands to the minimum possible. This was achieved by carrying out the experiment at 20.33 MHz and applying rapid MAS (6 kHz), which allowed the analysis to be carried out by simulating spectra by evaluating Equation (1), and then fitting the experimental spectra by inspection by eye. A typical example is shown in Figure 2, which was obtained at ~60 °C. In fitting these lineshapes it was found that the relative populations could not be easily determined, and this is as expected by the fact that the equilibrium constant (and the exchange rates) varies as a function of temperature. This situation is discussed in greater detail by Searle¹⁵ and by Lane.⁵ The best fits for all the temperatures recorded are shown in Figure 3. As a result of

damage which occurred to the probe soon after these measurements were made it was not possible to calibrate the temperature of the sample. A replacement stator was inserted which would have an unknown effect on the temperature calibration and it would be unwise to use these data to obtain kinetic activation parameters. The main source of error would arise from the fact that the two stators employ different bearing designs which require significantly different bearing pressures to maintain the same spin rate. The thermal mixing of the room temperature spinner gases and the variable temperature heater gas of the initial stator would therefore be unpredictable and an accurate calibration could not be obtained.

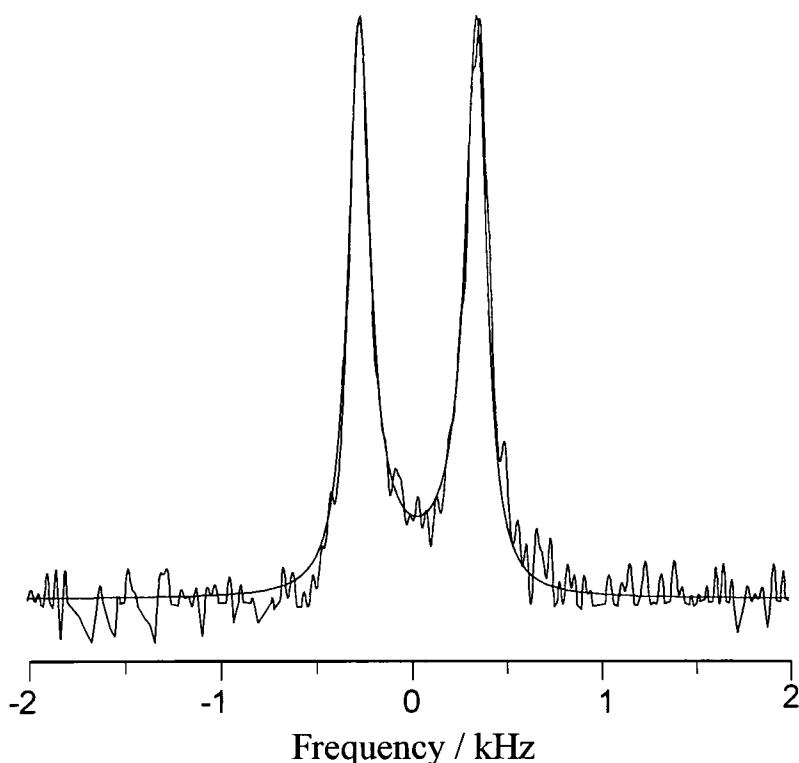


Figure 2

Experimental lineshape for the ^{15}N CP/MAS spectrum of DR278 II recorded at 60 °C and the corresponding best fit with an estimated exchange rate of $k=460$ Hz.

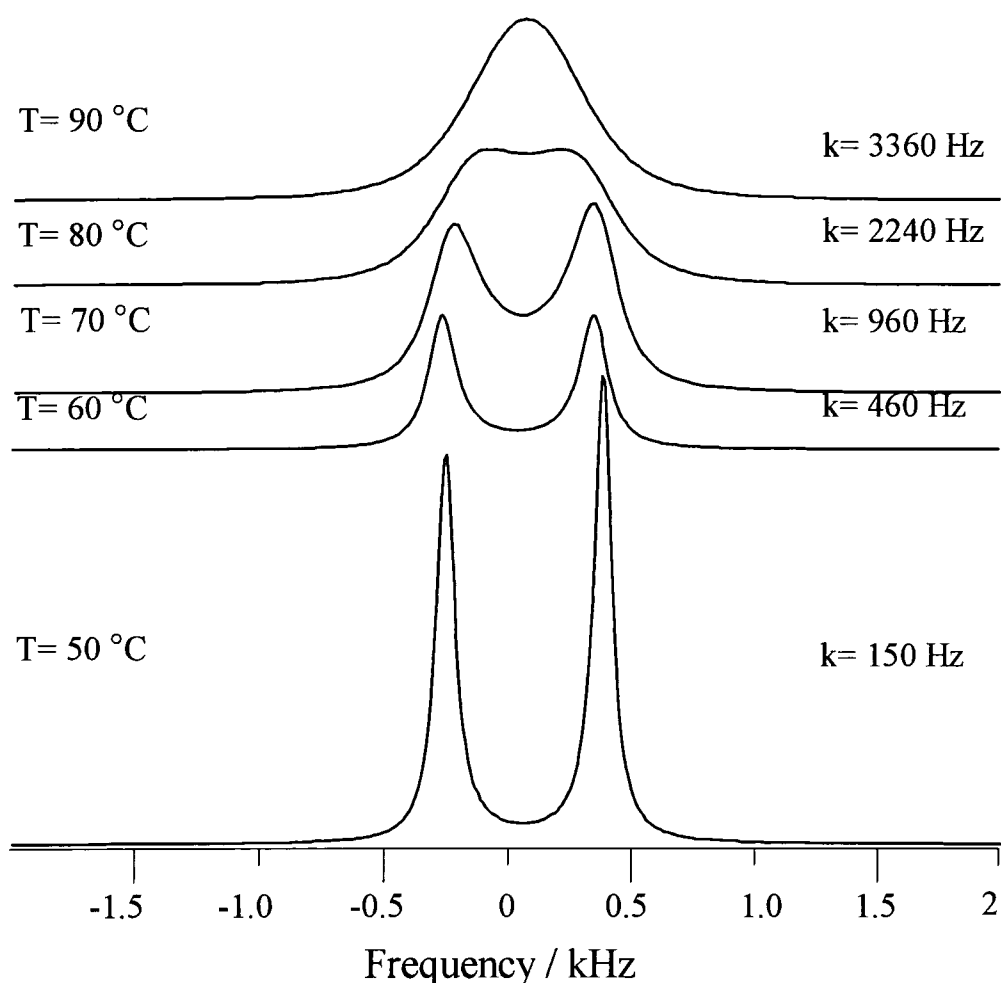


Figure 3

Results of the simulated ^{15}N lineshapes for the exchange broadened resonances from 50 °C to 90 °C (uncalibrated temperatures), plotted on an absolute scale.

From Figure 3 it can be easily seen that when exchange broadening occurs the maximum amplitude of the lines becomes reduced. This was also observed in the ^{15}N solution-state spectrum recorded at ambient temperature in CDCl_3 solution. However no further analysis of the solution-state kinetics has been carried out via ^{15}N NMR. With increasing the temperature it is also evident that there is an additional intrinsic shift to lower frequency of the whole band, with the assumption that the reference frequency is fixed at all temperatures over the range used.

4.2 Magnetisation Transfer Experiments.

In the slow exchange regime where no observable effect can be detected upon the linewidth, as outlined previously, it is possible to follow the exchange process via exchange-driven magnetisation transfer techniques. Ernst *et al* discussed thoroughly the application of such techniques in both one¹⁶ and two dimensions¹⁷. In both the one-dimensional and two-dimensional experiments, relaxation of the z-magnetisation occurs during a mixing time due to exchange, creating modulation of the signal intensity or cross peaks in the two experiments respectively. Magnetisation (coherence) transfer sequences can be applied to monitor not only exchange, but also dipolar coupling constants under rotational resonance conditions in solids,¹⁸ and they form the basis for virtually all 2D spectral editing techniques in both solids¹⁹ and solutions.²⁰ These techniques have only been possible due to the time-domain nature of FT NMR.

4.2.1 1D Selective Polarisation Inversion (SPI).

The pulse sequence which was used is outlined in Figure 4. It essentially consists of a non-selective preparation component, in this case cross polarisation, followed by a selective inversion of one signal. The inverted state can be created by several methods which include DANTE,²¹ soft pulses, and shaped pulses. Quite often these schemes are only useful for systems with highly dispersed isotropic shifts in the solid state. In the cases of DANTE and soft pulses the transmitter is placed on resonance with respect to the line to be inverted. However both techniques involve long cycle times for the creation of the inverted state, during which exchange can

occur. Also, with soft pulses the excitation bandwidth is inversely proportional to the duration of the pulse, and as a result excitation selectivity is often compromised to reduce the pulse duration.

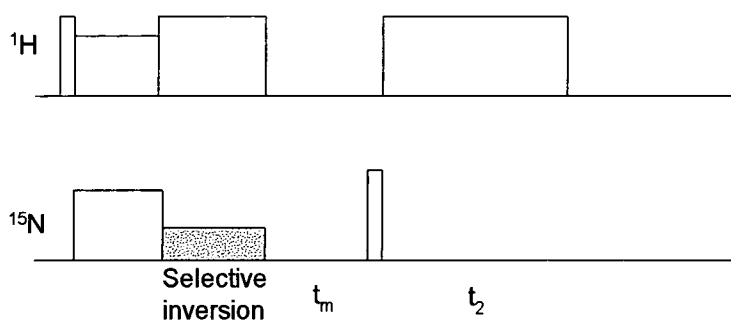


Figure 4

Schematic representation of the pulse sequence used in the general magnetisation-transfer sequence.

In the DR278 β -labelled system, which was previously analysed, there is a ^{15}N chemical shift separation of ~ 30 ppm. At 30 MHz for ^{15}N this relates to a frequency of 900 Hz which would require a soft pulse of duration in excess of 2 ms to create an inverted state with the appropriate selectivity. Additionally, the signal intensity is damped as a result of T_2 dephasing during the initial inversion step. The method of choice used here is based upon the precession frequencies and the angle that the magnetisation vectors subtend with the rotating axis system after a period of free precession, because it is highly selective and less time is required for inversion. The rate of precession in the transverse plane, within the rotating frame, is equal to the frequency offset, Δf , from the transmitter and subsequently the angle, θ , acquired during a time t_1 is simply $2\pi \Delta f t_1$. To create a rotation of 180° relative to the carrier then $t_1 = 1/(2\Delta f)$. By suitably placing the carrier at Δf from one signal and $2\Delta f$ from

the other then these signals will acquire a 180° phase difference relative to each other. The actual pulse sequence used is shown in Figure 5. This method has been used both for solutions²² and solids,²³⁻²⁶ with this same pulse sequence being utilised recently in the determination of the relative orientations of the ^{15}N shielding tensors and of the hydrogen-bonding geometry for a series of pyrazole cyclic trimers and tetramers under off-magic-angle spinning conditions.²⁷

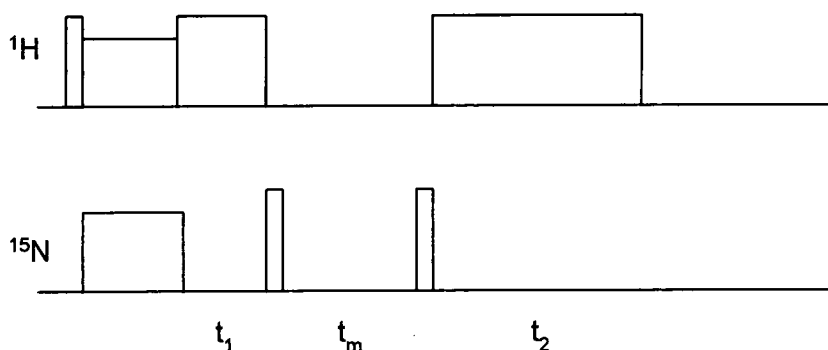


Figure 5

Magnetisation transfer sequence with selective inversion obtained via a non-selective pulse.

Application of a 90° pulse stores the magnetisation along the z axis, at which point relaxation occurs via the exchange-modified Bloch equations if utilising a classical approach. For a two site $A \leftrightarrow B$ scheme the coupled differential equations are:

$$\frac{d(M_Z^A)}{dt} = -R_{A1}(M_Z^A - M_0^A) - k_f M_Z^A + k_b M_Z^B$$

$$\frac{d(M_Z^B)}{dt} = -R_{B1}(M_Z^B - M_0^B) - k_b M_Z^B + k_f M_Z^A$$

where M_Z^A and M_Z^B are the z-magnetisations of sites A and B respectively at time t , M_0^A and M_0^B are the equilibrium z-magnetisation, R_{A1} and R_{B1} are the spin-lattice relaxation rates ($1/T_1$) for each site, and k_f and k_b are the forward and backward rate constants, defining $A \Rightarrow B$ as the forward process. These Bloch equations are only valid under perfect experimental conditions and it becomes very complex to consider this classical approach in non-ideal cases, of which pulse imperfections form an example.

The density matrix formalism allows a more rigorous investigation to be carried out. The density matrix for this isolated system,²⁵ at time $t_2=0$ is given by:

$$\rho(t_2(0)) = e^{-i(\frac{\pi}{2})I_x} e^{-i\bar{\nu}t_m} e^{-i(\frac{\pi}{2})I_x} . \quad (2a)$$

$$\left[e^{-i2\pi\Delta I_x t_1} I_x^A e^{+i2\pi\Delta I_x t_1} + e^{-i4\pi\Delta I_x t_1} I_x^B e^{+i4\pi\Delta I_x t_1} \right]. \quad (2b)$$

$$e^{i(\frac{\pi}{2})I_x} e^{i\bar{\nu}t_m} e^{i(\frac{\pi}{2})I_x} f(t_1, \Delta W_{CSA}, T_2) \quad (2c)$$

This representation shows more clearly the full dynamics of the experiment. In line (2b) the evolution of the initial I_x magnetisation, created from the CP preparation component, for both sites is clearly traced out, with the evolution of site B precessing twice as fast as that of site A, which, with the previously given timing for t_1 , results in a phase-inverted state. The accuracy of placing the transmitter has to be considered carefully as this will result in a loss of signal due to phase cycling the I_y signal away. However, the accuracy of the experiment would suffer more drastic damage due to the creation of a spin system which is not phase-inverted, but

in some other non-equilibrium state. The relaxation processes during t_1 must be considered and may be represented by $f(t_1, \Delta\omega_{\text{CSA}}, T_2)$, which is a complex function of the shielding tensor, the transverse dephasing time under proton decoupling and the t_1 evolution time. Consideration of the isotropic shifts, as in liquids, simplifies $f(t_1, \Delta\omega_{\text{CSA}}, T_2)$ to a simple exponential damping imparted by T_2 dephasing. With systems containing a large SA component to the observable spectrum, one must consider the effect of the sample spinning, which further complicates the situation. Under MAS the dephasing associated with the t_1 period is primarily due to the time dependence of the resonance frequency resulting from the SA under such spinning. As proven by Marich & Waugh²⁸ such dephasing is only refocussed at integral multiples of the rotor period, and a rotor echo occurs, forcing one to store the magnetisation only at the top of a rotor echo. The temporal width of the rotor echo is inversely proportional to the static lineshape, and for large SA this fact imposes a very strict rotor synchronisation on the evolution period. This undetermined state of the initial magnetisation is one severe drawback of this technique in comparison to 2D exchange spectroscopy, where this kind of relaxation only manifests itself in spectral broadening in the second dimension.

The average Hamiltonian, $\bar{\mathcal{H}}$, during t_m contains the terms included in the Bloch equations (T_1 and exchange relaxation) in terms of relaxation and exchange superoperators, and of the spin-spin coupling terms which cause rapid dephasing of the remaining transverse magnetisation, which simplify the situation. In solution-state experiments the transverse magnetisation is deliberately destroyed by the application of gradients. The spin labelling is eventually lost if the mixing time is

long in comparison to the longitudinal relaxation time constant T_1 . Even under cross polarisation conditions, where the recycle delay is governed by the T_1 of the protons, we have to consider the T_1 relaxation of the X nucleus, since explicit sampling of the X magnetisation occurs for various mixing times. Restoration of this phase-inverted z-magnetisation to the transverse plane allows the detection of the two signals. Variation of the mixing time, the duration during which the magnetisation is stored along the z-axis, allows a thorough investigation of the exchange dynamics. A simulation of the evolution of the magnetisation of the two spins is given in Figure 6.

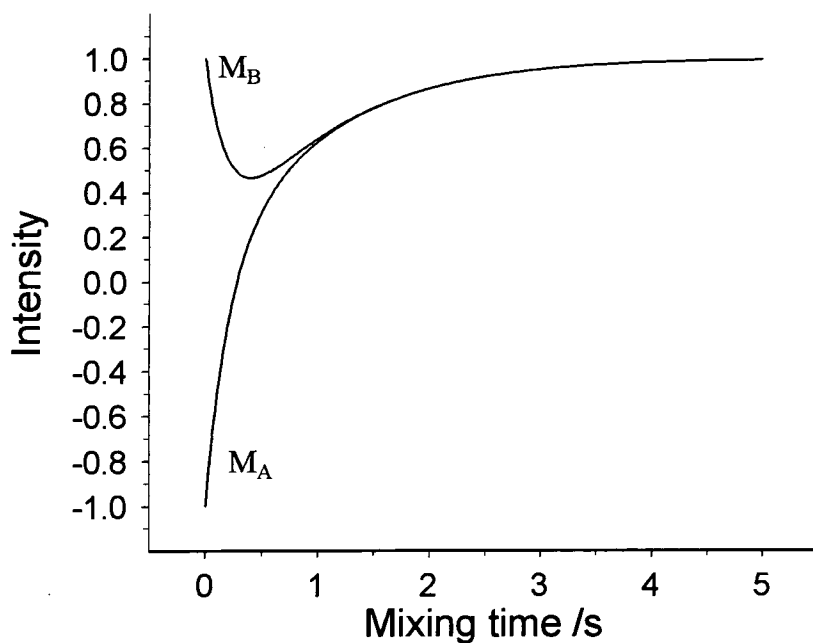


Figure 6

Simulation of the SPI experiment, with $T_1=1$ s and a total exchange rate of $k=2$ Hz for an equally populated two spin system.

This 1D technique requires the application of about 10 different mixing times per temperature in order to obtain a suitably good estimation of the exchange rates. Hence, a great reduction in time is observed in comparison to a full 2D exchange sequence, which will typically have several hundred increments in the t_1 dimension. This is defined by the fact that the spectral width in the second dimension has to be sufficiently large to incorporate all of the signals, including sidebands. Obviously this becomes a serious problem in the analysis of nuclei which have large shielding anisotropies, *e.g.* ^{15}N , as shall be discussed later. The saving in time is rather staggering when one considers the fact that a full kinetics analysis at 10 temperatures via the 2D exchange sequence would take about 20 days, while the 1D analogue takes only 3 days. In analogy with 3D accordion spectroscopy²⁹ one could Fourier transform along the t_m dimension, and the resultant lines would show a linewidth dependence upon both the T_1 relaxation and the exchange rate. This would require equidistant sampling to allow a discrete Fourier transformation to be applied, and this again would lengthen the experimental time, but with the advantage of a significant simplification of the analysis to obtain exchange rates.

4.2.1.1 Results: Application to DR278 form II.

The rate of the motional process within DR278 II is expected to be less than several hundred hertz, at room temperature, due to the fact that minimal exchange broadening is observed in the ^{15}N spectrum for the β -labelled sample. Consequently, a low temperature study would increase the temperature range over which the motion can be probed, increasing the accuracy for estimation of any activation parameters. The ^{15}N spectrum consists of two central resonances separated by 32 ppm, which corresponds to 960 Hz at 30 MHz, and a large spinning sideband envelope covering 1000 ppm (30 kHz). In the previous section it was shown that the peak at 121 ppm was from the hydrogen-bonded (β -H) conformer, and the 89 ppm peak was from the non-hydrogen bonded (β -nH) conformer. The complete SPI analysis was carried out from 243 K to 323 K using the Varian VXR 300 MHz spectrometer previously outlined. With such a large SA the FID is represented by a train of rotor echoes, each of which is very narrow. The widths of these are approximately 11 μs and imparts a tight restriction upon the timing during the inversion component of the sequence.

Experimentally it was observed that the evolution time (t_1) had to be a multiple of $2n$ rotor periods, where n is integer, and that the error in the spin rate should be less than ± 50 Hz. The necessity for rotor synchronisation is shown in Figure 7. A spin rate of 3850 Hz was subsequently chosen such that $n=2$ and a t_1 evolution time of 515 μs was used. The transmitter was placed to high frequency of the 121 ppm peak, and as a result the 121 ppm resonance had its phase inverted. A

typical SPI spectrum is shown in Figure 8, which shows how large the SA is with a substantial number of sidebands being observed.

The ^{15}N spin-lattice relaxation time was found to be $\sim 1000 \pm 100$ s via a non-selective inversion-recovery sequence, as first outlined by Torchia.³⁰ This sequence allows for a more rapid repetition rate, determined by the proton T_1 relaxation time, which is generally shorter than that for the ^{15}N nucleus. The ^{15}N T_1 relaxation time is long enough to allow the exchange-modified Bloch equations to be simplified by ignoring T_1 relaxation during the relatively short mixing times. The time evolution of the individual magnetisation vectors, during the mixing time, can now be considered to be governed by first-order reaction kinetics and as such can be fitted, for the general case of a non-integral equilibrium constant, to a simple shifted exponential function. In the following analysis the difference of the two magnetisations was fitted as a function of mixing time:

$$M_{diff} = (M_Z^A - M_Z^B) \exp(-(k_f + k_b) t) + (M_Z^A + M_Z^B)$$

The relative sign (phase) of the magnetisation vectors is retained in these equations and as a result the first term is the total initial magnetisation, the second is the exponential recovery back to equilibrium, and the third is the final equilibrium state in the absence of T_1 relaxation. Figure 9 shows the relaxation curves for the difference equations, taken at 50 °C and 22 °C, and the corresponding fitted lineshapes. As can be seen, the relaxation process is much faster for the higher temperature and the results from the whole temperature range are given in Table 1.

The values were obtained by a non-linear regression of the above equation, using the windows software package MATHCAD.³¹

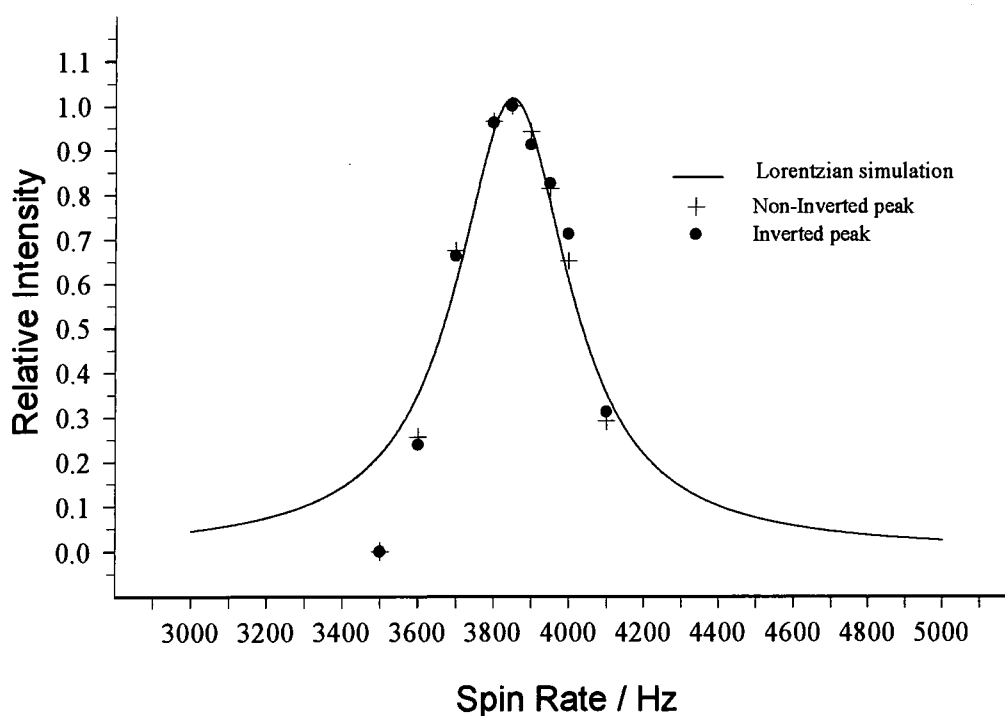


Figure 7

Variation of signal intensity as a function of spin rate to verify rotor synchronisation necessity. A Lorentzian curve with a FWHH of 300 Hz is shown for comparison.

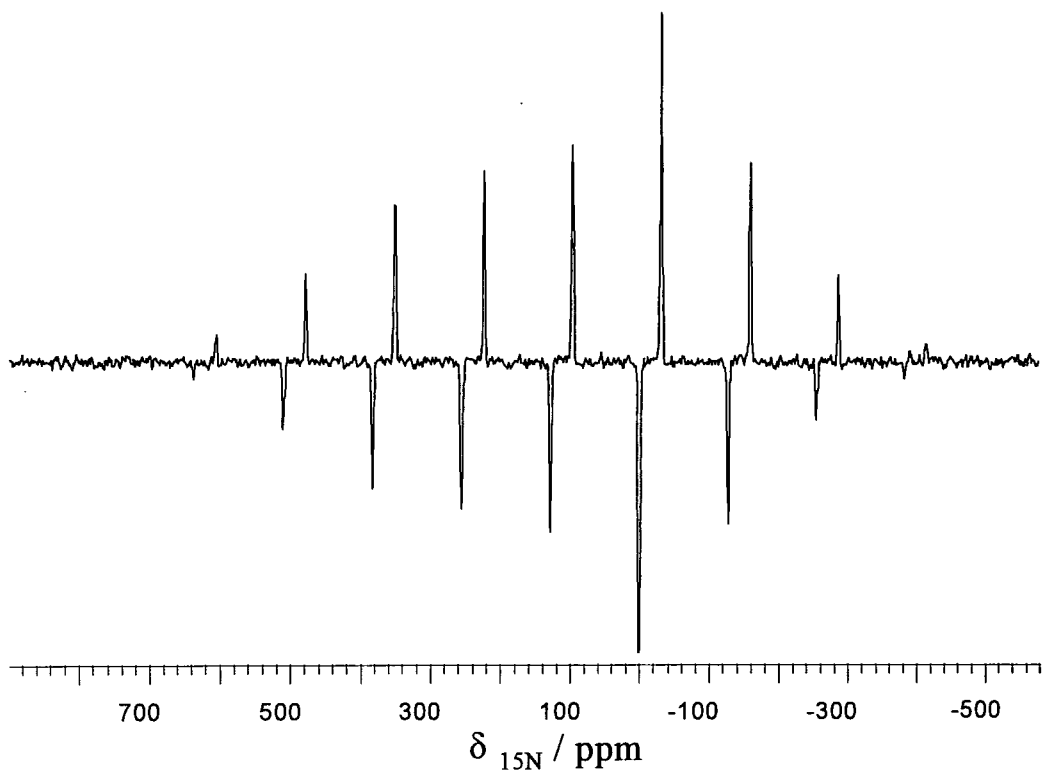


Figure 8

Typical ^{15}N SPI spectrum taken at 8°C . The acquisition parameters were $t_1=515\ \mu\text{s}$, $t_m=500\ \mu\text{s}$, with a pulse delay of 30 s, a contact time of 10 ms and 48 transients.

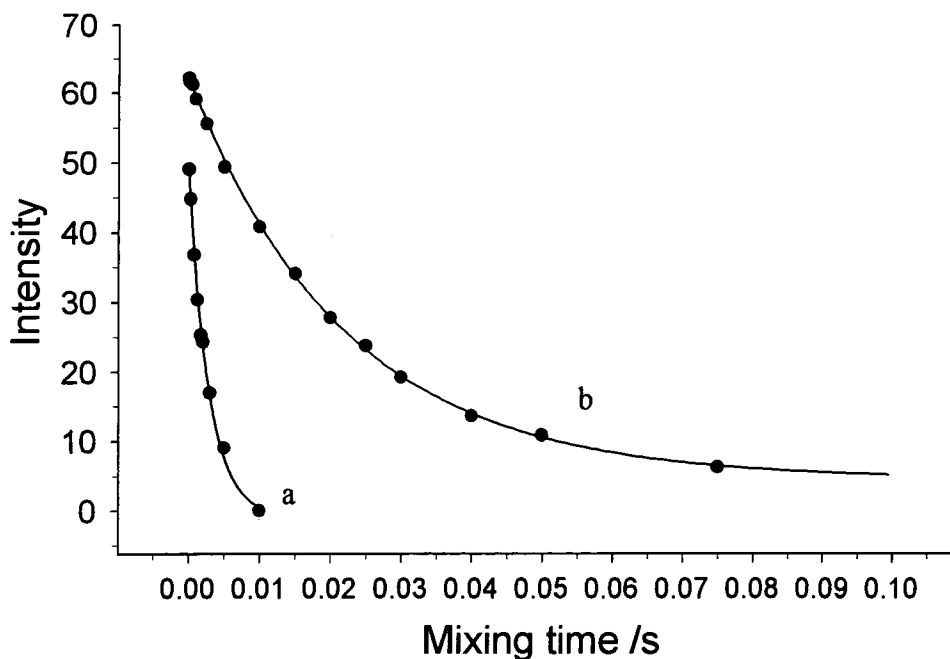


Figure 9

Experimental results for the ^{15}N SPI experiment, shown as difference curves, for DR278 II at a/ 50°C and b/ 22°C , with the corresponding best-fit curves. Note the significantly enhanced exchange rate for the higher temperature.

T/ K	243	253	263	273	281	298	303	313	323
k_A+k_B / Hz	0.11	0.34	1.4	4.1	10.3	45.3	87.6	178	349
$M_{\beta\text{-hB}}$	0.43	0.44	0.45	0.46	0.47	0.48	0.49	0.50	0.51
$M_{\beta\text{-nhB}}$	0.57	0.56	0.55	0.54	0.53	0.52	0.51	0.50	0.49

Table 1

Exchange rates and fractional populations from the SPI experiment as obtained by fitting the difference magnetisation.

Initial studies in kinetics used the Arrhenius activation theory, which was realised to depend upon rather over-simplified assumptions. A model-based treatment was given by Eyring which was based on statistical mechanics, and the resultant Eyring equation was derived:-

$$k = \kappa \frac{k_B T}{h} e^{-\frac{\Delta G^\ddagger}{RT}}$$

where $\Delta G^\ddagger = \Delta H^\ddagger - T\Delta S^\ddagger$, κ is the transmission coefficient, which will be assumed to be unity and k_B is the Boltzmann constant. To obtain the activation parameters one constructs the typical Eyring plot, as shown for the SPI and bandshape analysis results in Figure 10. The Arrhenius activation parameters ΔG^\ddagger (evaluated at 295 K), ΔH^\ddagger and ΔS^\ddagger can be obtained from this graph. These values are the Gibbs free energy, enthalpy and entropy of activation, and are measured relative to the activated transition state. Hence, knowing the forward and backward reaction rates allows one to determine these parameters for the forward and backward reactions, and the results are summarised in Table 2. The fractional populations were used to obtain the forward and backward reaction rates. The results from the bandshape analysis will be ignored in these calculations because, as discussed already, the probe temperature had not been calibrated. It should be noted, however, that if the temperature was reduced by 5 °C for each point corresponding to the bandshape results then the two sets of data become virtually indistinguishable. This suggests that the actual temperature may be ~5 °C too high.

These activation parameters yield information relating to the structure of the potential energy surface, which is presumed to be a double well, and therefore to the relative stabilities of the two structures. The relative stability of the two states is defined by the Gibbs free energy difference, ΔG , and as shown it is virtually zero at room temperature, indicating that the two states are almost equally populated. The interconversion rate between the two states is dominated by the enthalpic contribution. For simple phenyl ring rotation it has been shown⁷ that the free energy of activation is $\sim 58 \text{ kJ mol}^{-1}$, which is relatively close to the values obtained in this analysis. However, the barriers to rotation appear to be dominated purely by crystal packing interactions and the free volume present in the sample, which is related to the density. This azobenzene dye has a particularly low density in relation to other similar organic molecules. The packing coefficient, defined as the ratio of the Van der Waals volume of the molecule to the unit cell dimensions (assuming two molecules per cell), turns out to be ~ 0.6 for DR278 in relation to 0.7-0.8 for typical organics. However, similar studies have shown that phenyl ring flips can proceed significantly faster in large drug molecules *eg.* penicillin.⁹ 4,4'-Dimethyl-*trans*-phenylazobenzene undergoes a similar rearrangement which is on the same timescale.³² This is rather surprising when one considers the fact that the density would be expected to be much higher in the dimethyl-azobenzene sample, resulting in an increase in the rotational barriers via crystal packing interactions. Interestingly enough the crystal structure of 4,4'-Dimethyl-*trans*-phenylazobenzene shows the same disorder as for the present structure. Brown³³ solved the structure by assuming two orientations of the whole molecule, not just the azo linkage.

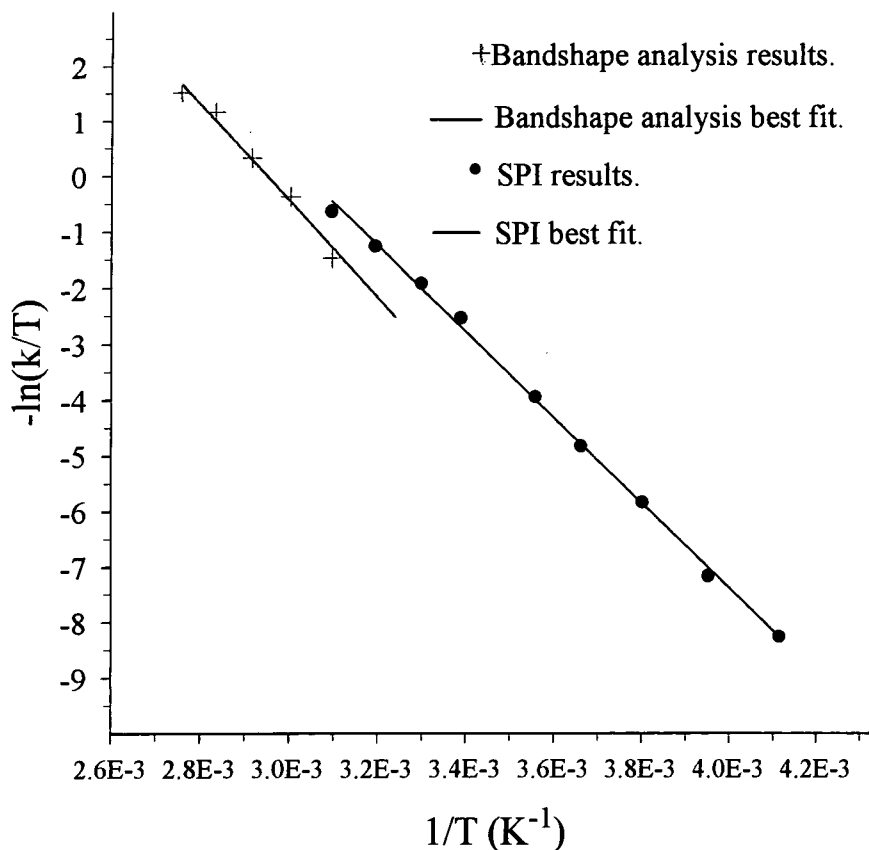


Figure 10

Results of the kinetics analysis presented as an Eyring plot, for both the bandshape analysis and SPI data, where k is the sum of k_f and k_b .

Forward (H to nH)			Back (nH to H)		
ΔG_{295}^\ddagger	ΔH^\ddagger	ΔS^\ddagger	ΔG_{295}^\ddagger	ΔH^\ddagger	ΔS^\ddagger
/ kJ mol ⁻¹	/ kJ mol ⁻¹	/ J mol ⁻¹ K ⁻¹	/ kJ mol ⁻¹	/ kJ mol ⁻¹	/ J mol ⁻¹ K ⁻¹
64.9 (±2)	63.8 (±2)	-3.6(±2)	65.1 (±2)	66.5 (±2)	4.7 (±2)

Table 2

Activation parameters obtained from the SPI kinetics analysis. The forward process is defined as that which converts the magnetisation at 121 ppm to the magnetisation at 89 ppm.

However, it must be remembered that this rotation was not considered to be a simple phenyl ring flip, but a crankshaft rotation of the full azo linkage. Due to the complex nature of solid state structures it would be impossible to solve the full wave equation for the solid, and carry out molecular mechanics calculations on this sample to compare experimental and calculated activation parameters. Additionally, it would be pointless to carry out such calculations in the gas phase because the primary barrier, *i.e.* the neighbouring molecules, has been removed from the problem.

4.2.2 Two-dimensional exchange (EXSY).

In an EXSY experiment one sequentially increments the t_1 evolution time in the magnetisation transfer sequence. After Fourier transformation in two dimensions, any non-exchanging resonances result in diagonal peaks, while those which have undergone exchange during the mixing time are represented by off-diagonal peaks. From the relative intensities of the peaks it is possible to obtain the exchange rate for the process. However, the results tend to be reliable only if several values of the mixing time are used, and with the fact that the sequence takes a long time this becomes a very time-consuming experiment to use for a complete kinetics analysis. As a result, only two EXSY spectra were obtained, with different mixing times, 20 ms and 200 ms, at ambient temperature, purely for the verification that cross peaks would arise as a result of exchange. This was indeed the case as can be seen in Figure 11. Using a mixing time of 20 ms only small off-diagonal peaks appear, but with a longer mixing time the off-diagonal elements increase

dramatically, as would be expected. The intensities of the diagonal and off-diagonal peaks can be shown¹² to be:-

$$\begin{aligned}a_{AA}(t_m) &= \frac{1}{4} e^{-R_1 \tau_m} \left[1 + e^{-k \tau_m} \right] \\ a_{AB}(t_m) &= \frac{1}{4} e^{-R_1 \tau_m} \left[1 - e^{-k \tau_m} \right]\end{aligned}$$

where k is the rate of mutual exchange and τ_m is the mixing time. Hence, in the case of equal populations and slow T_1 relaxation, *ie.* $R_1 = 0 \text{ s}^{-1}$, each signal will reach a common intensity of 0.5 at the limit of complete exchange, with the same exponential rate. This can be seen in the 200 ms spectrum where all the signals have approximately the same intensity. The spectra were acquired via the method of States³⁴ to obtain quadrature detection in the indirectly detected dimension.

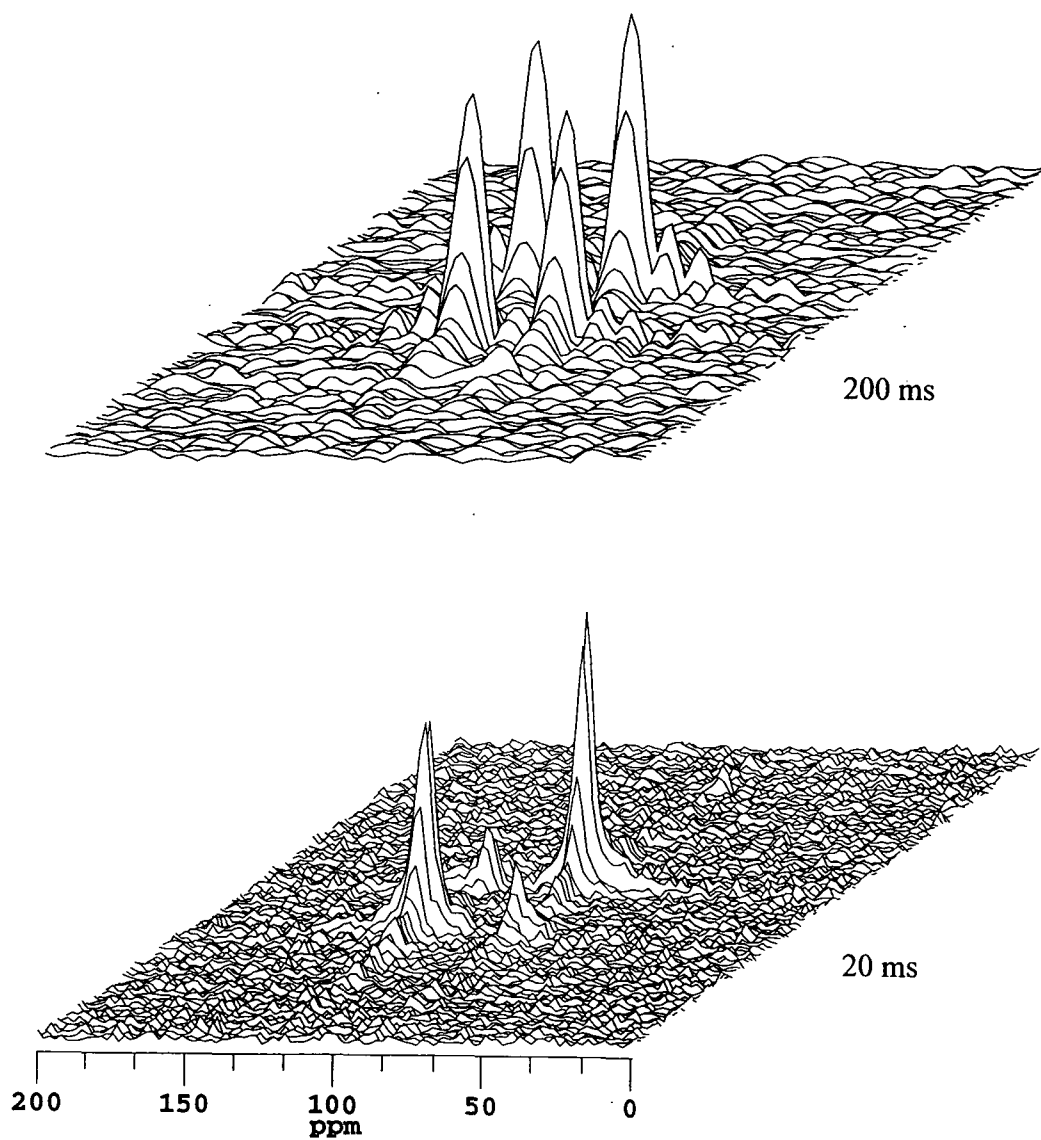


Figure 11

¹⁵N 2D EXSY spectrum of DR278 II obtained on the CMX200 at 20.33 MHz. Acquisition parameters were; $ct=10$ ms, $pd=30$ s, and mixing times of 20 ms and 200 ms. 128 points were acquired in the second dimension and zero-filled to 512 to create a square dataset.

Conclusions.

It has been possible by the analysis of an isotopically ^{15}N -enriched sample of DR278 II, via several NMR techniques, to evaluate the energetics of the motional process within this polymorph. The SPI sequence with inversion via the chemical shift offset method has proven to be a simple, yet effective, technique for obtaining accurate rate constants. The free energy of activation for the process was found to be $\sim 65 \text{ kJ mol}^{-1}$, which is in accordance with other investigations of phenyl ring flips. The mechanism for the process has not been identified, but it is still consistent if it is thought to be a concerted rotation of the azo linkage in a crankshaft manner. The main source of error was found to relate to the temperature calibration and not within the calculation of the rate constant. Every effort should be made to calibrate temperatures within probes prior to carrying out any kinetics analysis.

References.

- 1 R. Cimiraglia and H.-J. Hofmann, *Chem. Phys. Lett.*, **217**, 430, (1994).
- 2 J. Sandstrom, "Dynamic NMR Spectroscopy", Academic Press, London/ New York, (1982).
- 3 H.S. Gutowsky and C.H. Holm, *J. Chem. Phys.*, **25**, 1228, (1956).
- 4 C.L. Perrin and T.J. Dwyer, *Chem. Rev.*, **90**, 935-967, (1990).
- 5 A.N. Lane, *Prog. NMR Spec.*, **25**, 481-505, (1993).
- 6 C.G. Hoelger, B. Wehrle, H. Benedict and H.H. Limbach, *J. Phys. Chem.*, **98**, 843-851, (1994).
- 7 F.G. Riddell, M. Bremner and J.H. Strange, *Magn. Reson. in Chem.*, **32**, 118, (1994).
- 8 J.R. Long, B.Q. Sun, A. Bowen and R.G. Griffin, *J Am. Chem. Soc.*, **116**, 11950-11956, (1994).
- 9 J. Fattah, J.M. Twyman, S.J. Heyes, D.J. Watkin, A.J. Edwards, K. Prout and C.M. Dobson, *J Am. Chem. Soc.*, **115**, 5636-5650, (1993).
- 10 D. Suwelack, W.P. Rothwell and J.S. Waugh, *J. Chem. Phys.*, **73**, 2559-2569, (1980).
- 11 W.P. Rothwell and J.S. Waugh, *J. Chem. Phys.*, **73**, 2721, (1981).
- 12 J. Jeener, B.H. Meier, P. Bachmann and R.R. Ernst, *J. Chem. Phys.*, **71**, 4546-4553, (1979).
- 13 M.T. Rogers and J.C. Woodbrey, *J. Phys. Chem.*, **66**, 540, (1962).
- 14 A. Schmidt and S. Vega, *J. Chem. Phys.*, **87**, 6895, (1987).
- 15 M.S. Searle, *Prog. NMR Spec.*, **25**, 403-480, (1993).

- 16 R.R. Ernst, G. Bodenhausen and A. Wokaun, "Principles of Nuclear Magnetic Resonance in One and Two Dimensions", 2nd Ed, Ch. 4.6, Clarendon Press, Oxford, (1991).
- 17 R.R. Ernst, G. Bodenhausen and A. Wokaun, "Principles of Nuclear Magnetic Resonance in One and Two Dimensions", 2nd Ed, Ch. 9, Clarendon Press, Oxford, (1991).
- 18 D.P. Raleigh, M.H. Levitt and R.G. Griffin, *Chem. Phys. Lett.*, **146**, 71, (1988).
- 19 P. Caravatti, G. Bodenhausen, R.R. Ernst, *Chem. Phys. Lett.*, **89**, 363-367, (1982).
- 20 R.R. Ernst, G. Bodenhausen and A. Wokaun, "Principles of Nuclear Magnetic Resonance in One and Two Dimensions", 2nd Ed, Ch. 8, Clarendon Press, Oxford, (1991).
- 21 G.A. Morris and R. Freeman, *J. Magn. Reson.*, **29**, 433, (1978).
- 22 G. Robinson, P.W. Kuchel, B.E. Chapman, D.M. Doddrell and M.G. Irving, *J. Magn. Reson.*, **63**, 314-319, (1985).
- 23 N.M. Szeverenyi, A. Bax, G.E. Maciel, , *J. Am. Chem. Soc.*, **105**, 2579-2582, (1983).
- 24 G. Almond, *PhD Thesis*, University of Durham, (1995).
- 25 C. Connor, A. Naito, K. Takegoshi and C.A. McDowell, *Chem. Phys. Lett.*, **113**, 123, (1985).
- 26 L.D. Field, N. Bampos and B.A. Messerle, *Magn. Reson. Chem.*, **29**, 36-39, (1991).
- 27 C.G. Hoelger, F. Aguilar-Parrilla, J. Elguero, O. Weintraub, S. Vega and H.H. Limbach, *J. Phys. Chem.*, **120**, 46-55, (1996).
- 28 M.M. Marich & J.S. Waugh, *J. Chem. Phys.*, **70**, 3300-3316, (1979).

- 29 R.R. Ernst, G. Bodenhausen and A. Wokaun, "Principles of Nuclear Magnetic Resonance in One and Two Dimensions", 2nd Ed, Ch. 9.6, Clarendon Press, Oxford, (1991).
- 30 D.A. Torchia, *J. Magn. Reson.*, **30**, 613, (1986).
- 31 MATHCAD Plus 6, Mathsoft Inc, (1995).
- 32 G. McGeorge, A.M. Chippendale and R.K. Harris, unpublished work.
- 33 C. J. Brown, *Acta Cryst.*, **21**, 153, (1966).
- 34 D.J. States, R.A. Haberkorn and D.J. Ruben, *J. Magn. Reson.*, **38**, 286, (1982).

For industrial applications the dye chemist would prefer to choose molecules which are present as the hydrazone tautomer. These dyes tend to be more cost effective than azobenzene dyes, due to their higher extinction coefficients. Extensive research has been carried out using solution-state techniques to understand this tautomerism. UV-Vis, Raman, and ^1H , ^{13}C and ^{15}N NMR have all proven useful. Conversion from the azo tautomer to the hydrazone tautomer results in a large bathochromic shift,^{4, 5} which can exceed 100 nm for certain systems. Raman spectroscopy has proven popular due to the high symmetry of the azo linkage, which renders the resonance weak in IR studies, but very strong in Raman spectroscopy. A further extension of Raman spectroscopy is to carry out resonance Raman studies, where only the characteristic vibrations for the chromophore are selectively excited by application of a coherent stimulus to a particular electronic transition. The enhanced bands correspond to the N=N stretch, C-N stretch and in-plane deformation vibrations, for the case of *trans*-azobenzene.

Substituted phenylazobenzenes predominately exist in solution as the azo form. Upon protonation, which occurs in acidic media, it is possible for zwitterions to be created. Here, one must consider the possible resonance structures, and the resultant mesomeric effect upon the shielding parameters. In this chapter an initial survey of the present state of the NMR analysis of azobenzene dyes will be presented. Once this foundation has been built, a thorough investigation of the solution-state and solid-state structures for a series of phenylazobenzene sulphonic acid dyes will be described, primarily via ^{13}C and ^{15}N NMR techniques, but also with corroborating information from Raman spectroscopy and UV-Vis spectroscopy.

5.1 Application of C-13 and N-15 NMR for the analysis of carbocyclic azo dyes: A review.

5.1.1 NMR.

Azobenzene dyes contain two aromatic groups attached to each end of the azo linkage. When both groups are aromatic then the resultant dye is classed as a carbocyclic dye. The presence of electron donating and accepting groups creates extensive modification of the π -electron density across both rings, and with the inherent conjugation present in such systems prediction of shielding constants becomes rather complicated. The solution state creates a much simpler environment in which one can generally assign shifts by considering the average structure created by rapid molecular and group rotations. Ewing⁶ built up the first comprehensive collection of ^{13}C substituent chemical shift (SCS) parameters for mono-substituted benzenes. With these data and the fact that substituent effects in benzenes are approximately additive, unless substituents are *ortho* to each other, it becomes possible to calculate the shifts for poly-substituted benzenes according to:

$$\delta_{\text{C}} = 128.5 + \sum_i A_i(\text{R})$$

where $A_i(\text{R})$ represents the chemical shift increment for a substituent R in the i th position, as tabulated by Ewing⁶ for example. This includes the parent azobenzene molecule, as shown in Figure 1, which will be used throughout this chapter.

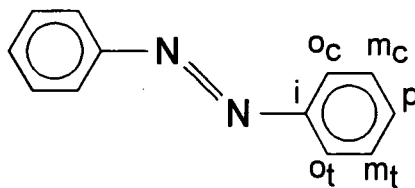


Figure 1

The SCS parameters for the *ipso*, *ortho*, *meta* and *para* positions in azobenzene are $A_i = 24.0$ ppm, $A_o = -5.8$ ppm, $A_m = 0.3$ ppm and $A_p = 2.2$ ppm respectively. In solution the o_c and o_t (likewise m_c and m_t) resonances are equivalent due to rapid phenyl ring rotation. Lycka⁷ and Chippendale *et al.*⁸ have analysed several 4,4'-disubstituted *trans*-azobenzenes in which these simple rules held true. However, addition of groups *ortho* to the azo linkage result in changes which were attributed to the presence of locked conformations, with the substituent being found purely in the o_t position, rendering these traditional additivity rules virtually useless. Additionally, if this *ortho*-group can participate in the formation of an intramolecular hydrogen bond, then a conformational equilibrium can be set up whereby the electronic and hydrogen-bonding interactions compete to produce the more stable conformation. This has already been discussed in the previous chapter for the case of an *ortho*-acetamido group. For large inert *ortho*-substituents the benzene rings may twist out of the plane of the azo group to minimise steric hindrance, and also changes in bond angles may significantly contribute to rather complicated geometries and NMR spectra. Thus, the maximum chemical shift deviation between the o_c and o_t pair will be reduced depending upon the exact orientation of the aromatic ring. This further complication is particularly pronounced in the solid state

where the aforementioned rapid molecular rotations are not present to average shifts. Fedorov *et al.*⁹ have recently published ¹³C data relating to some 40 azo disperse dyes in an attempt to understand the combination of hydrogen-bonding, electronic effects and steric effects on solution-state shifts.

In the case of *ortho*-hydroxy groups the structure is almost always found to be hydrogen bonded. Depending upon the neighbouring substituents, the proton can actually transfer over to the nitrogen atom, and form a hydrazone dye or an equilibrium between the two tautomers. This is generally not observed in carbocyclic phenylazobenzene dyes, but it has been characterised by Fedorov^{10, 11} under conditions of extreme basicity. Fedorov's analysis is rather important in relation to the current research. It was observed for resorcinol (2',4'-dihydroxy phenyl group) azobenzene derivatives that the ¹³C NMR shifts in the solid state were identical to those in strongly alkaline aqueous solutions, and that these structures were deduced to be hydrazone in nature in the solution state. However, a discussion of the solid-state structure was totally avoided in those reports, and it definitely does not contain a formal negative charge as in solution, unless it is some way stabilised by intermolecular interactions. The preferred state of azonaphthol dyes is that of the hydrazone tautomer, but the exact equilibrium constant is highly dependant upon both temperature and pKa of the solvent.¹² Heterocyclic azobenzene dyes also constitute an important class, because it is possible to force the hydrazone tautomer by the substitution in the heterocycle (the heterocycle is typically a pyridone). Thus, from Lycka's work¹³ it has been possible to identify the shifts one would expect from a phenyl ring attached to 1/ an azo group, 2/ an azo group intra-molecularly hydrogen-bonded to an *ortho*-substituent, 3/ a hydrazone group and 4/ a hydrazone

group intra-molecularly hydrogen-bonded to an *ortho*-substituent. The SCS parameters arising from these systems are summarised in Table 1.

One important additional piece of information that remains to be clarified is the effect that the strongly acidic sulphonic acid group has upon both the observed ^{13}C NMR shifts, and also on the expected structure in various solvents. Benzene sulphonic acid has a pKa of ~ -2 in aqueous solution, being nearly as acidic as sulphuric acid, and will deprotonate in all aprotic solvents. This can prove to be a problem due to the insolubility of the azobenzene sulphonic acids in acidic aqueous media, which is the type of solvent that one would wish to record a spectrum in, in order to obtain the NMR shifts relating to the neutral molecule.

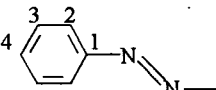
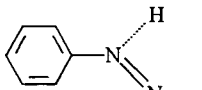
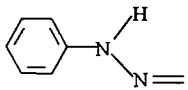
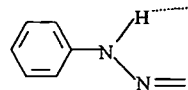
	1/	2/	3/	4/
Carbon signal				
C1	23.8	22.0	13.5	12.4
C2	-6.2	-6.4	-14.2	-12.9
C3	1.0	0.7	0.8	1.0
C4	2.0	2.0	-3.9	-2.9

Table 1

^{13}C SCS values for the phenyl resonances in azo and hydrazone systems
in ppm relative to *trans*-azobenzene.

5.1.2 N-15 NMR.

Nitrogen-15 NMR has proven to be very useful in the determination of the structures found for these dyes. The primary reason for this is the huge shielding range that ^{15}N nuclei cover, and also the nature of the tautomerism that we wish to analyse here. Azo signals are generally found between 50 ppm and 150 ppm, whereas those for hydrazos cover a much larger range, -200 ppm to 70 ppm. The latter is a feature of the protonation of the α nitrogen position in converting from the azo to hydrazo tautomer. For ^{15}N NMR a low-frequency shift of between 200 and 300 ppm is realised for this α ^{15}N resonance. Both Jonsen¹ and Lycka¹⁴ have successfully used the difference between the α and β ^{15}N resonances to pin-point the percentage of hydrazo or azo form present in a system. To be able to have confidence in this information one must understand the SCS arising at the two nitrogen sites as a result of substitution of the aromatic rings, and also the effect of intra-molecular hydrogen bonding in *ortho*-substituted azobenzenes. Some pertinent SCS parameters are shown in Table 2 for the N_α and N_β signals of four 4-substituted *trans*-azobenzenes,¹⁵ with the substituent being attached to the ring adjacent to N_α . A general trend was observed such that the resonance of the nitrogen atom closer to the para-substituent was always shifted to lower frequency, regardless of substituent, while that for the second nitrogen atom was shifted to lower frequency with electron-donating substituents, and to higher frequency for electron-accepting substituents. From the entry for NH_2 it is clear that there is a strong solvent dependency upon the SCS for the N_β signal.

Substituent	SCS _α	SCS _β
^b N(CH ₃) ₂	-10	-31
^a NH ₂	-10	-37
^b NH ₂	-9	-26
^a OH	-6	-20
^b NO ₂	-7	+17

Table 2

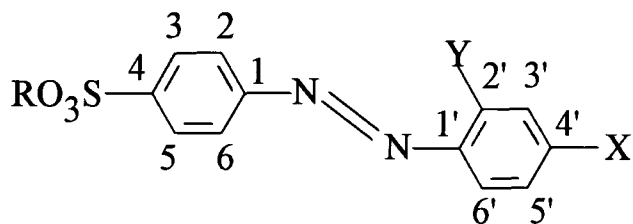
¹⁵N SCS values for 4-substituted trans-azobenzenes relative to that for trans-azobenzene (130 ppm). The spectra were recorded in ^a DMSO-d₆ and ^b in CDCl₃.

Kuroda *et al*¹⁶ provided direct evidence of the site of protonation in acidic media of 4-aminophenylazobenzene by ¹⁵N NMR. In weakly acidic media the acidic proton was located at both the azo nitrogen β to the amino group and also at the amino group. The shifts (and supporting UV/ Vis data) suggested that the equilibrium favoured the protonation of the amino group. In strong acid where two protons have transferred to the dye it was shown that one of the protons was located on the amino group and the other at the nitrogen α to the amino group, either as an azonium cation or as the hydrazo form. Knowledge of these ¹⁵N resonances may assist in understanding two of the sulphonate systems under investigation in the present chapter.

5.2 Analysis of NMR spectra for a series of water soluble dyes.

5.2.1 NMR.

A complementary range of mono-sulphonic acid phenylazobenzene dyes, and their sodium salt analogues, have been analysed in an attempt to correlate the solution-state and solid-state NMR shielding constants. These dyes are generally present as the mono-anionic salts, making them highly soluble in aqueous solutions. This is beneficial in the dyeing procedure, but is a major disadvantage when it comes to washing the garment. Leaching of the dye colour occurs from the inferior wash fastness. As the free acids they are not actually used as dyes, being highly insoluble at all pH's in water, but the structures for the free acids may help in the understanding of the structures of more complex reactive dyes, as will be investigated later. The NMR shielding parameters relate to the molecular conformations, of which the solid-state structures are unknown. In solution it is generally perceived that they all exist in the azo form. As a result, the solution shifts will be assumed to be those that relate to the sulphonic acid anion of the corresponding dye (when recorded in DMSO-d₆). The assignments were made by comparison to data for similar molecules and the known substituent shifts previously discussed. The numbering system adopted is shown in Figure 2.



R=H, Na

Figure 2

The substituents R, X and Y are tabulated in Table 3 for the compounds recorded in solution, along with the corresponding ^{13}C chemical shift assignments. These spectra were all recorded in DMSO- d_6 , so solvent effects across the range can be considered to be comparable for all samples, and therefore ignored. The data for the parent sulphonic acid azobenzene anion has been built up from the literature and is reported as sample A.

The ^{13}C shifts in the sulphonate-substituted ring are all very similar when comparing across the range, and are as one would expect. It should be noted that the SCS parameters of $A_i = 16.7$ ppm, $A_o = 3.3$ ppm, $A_m = 0.3$ ppm and $A_p = 5.9$ ppm, relative to benzene, for the sodium sulphonate group¹⁷ have not been used in any of the current analyses, because Kosugi¹⁸ found a very poor correlation using these SCS parameters for di-substituted benzenes. It was suggested that the electronic nature of the sulphonate group varies according to the nature of the substituent. No other literature, to my knowledge, has been published on the SCS effects for poly-substituted benzenes with sulphonate groups attached. Thus the assignments given

in the literature for azobenzene sulphonates have been obtained purely by consideration of a large number of analogous compounds.

The assignment for I is within 1 ppm for all shifts in comparison to those for A. A low frequency shift of ~2 ppm appears for the C1 resonance of the di-hydroxy sample, when compared to the other molecules. This, by comparison with Table 1, is suggestive of the formation of an intra-molecular hydrogen bond. The other ring is, however, far more susceptible to the influences of hydrogen bonding, and changes can easily be observed at C2', C4' and C6' (depending on the sample). C6' allows one to determine the conformation of the *ortho*-substituent, *i.e.* *cis* or *trans* with respect to the azo linkage, which is important for V and VI and IX. VI and IX exhibit low-frequency shifts of 12.4 ppm in comparison to V, which are too large to be accounted for by the difference between the *meta*-SCS values for methyl, amino and hydroxy groups. These *meta*-SCS values are ~0 ppm, 0.5 ppm and 1.2 ppm respectively, and the corrected shifts for C6', due to the electronic interaction between the azo nitrogen lone-pairs with the C6' nucleus, are 117.3 ppm, 117.3 ppm and 128.5 ppm, for V, IX and VI respectively. Thus, an 11 ppm splitting is observed in these *ortho*-substituted samples, wholly in accordance with other previous reports in the literature, for both solids⁸ and liquids.¹⁹ These shifts therefore prove that *ortho*-CH₃ groups are present in the *trans*-orientation, while *ortho*-hydroxy groups are present in the *cis*-orientation, due to a stabilisation of the molecular system by the formation of an intra-molecular hydrogen bond.

Compound			Carbon										
No.	R	X	Y	1	2	3	4	1'	2'	3'	4'	5'	6'
A	Na	H	H	152.5	121.8	127.8	149.3	152.5	122.8	128.8	130.7	128.8	122.8
I	H	H	H	151.8	122.5*	126.7	150.1	151.7	122.2*	129.4	131.6	129.4	122.2*
II	Na	OH	H	152.0	121.6	126.7	149.5	145.3	125.0	116.0	161.1	116.0	125.0
III	H	OH	H	152.7	122.4	127.2	149.0	143.7	125.6	116.5	161.7	116.5	125.6
V	H	OH	CH ₃	152.6	122.0	126.8	149.1	143.4	141.3	117.1*	161.3	114.2	117.3*
VI	Na	OH	OH	150.4	121.1	126.7	148.8	132.3	156.5	102.9	163.3	109.2	129.7
VIII	Na	H	N(CH ₃) ₂	152.2	121.0	126.5	149.0	142.5	124.8	111.7	151.9	111.7	124.8
IX	H	NH ₂	CH ₃	151.4	120.9	126.5	148.4	142.3	141.9	117.2*	149.3	115.1	117.8*

Table 3

*Solution-state ¹³C chemical shift assignments for 4'-mono-substituted and 2',4'-di-substituted sulphonic acid azobenzenes. All spectra were recorded in DMSO-d₆. * Indicates that assignments are interchangeable. Data for sample A arise from a theoretical estimation taken from references 20 and 21. Chemical shifts for the CH₃ groups are 17.5 ppm for V, and 17.3 ppm for IX. The CH₃ signal for VIII is presumably hidden under the DMSO-d₆ solvent peak (~40 ppm).*

In the solid state the situation becomes rather more complex with the additional possibility of inter-molecular hydrogen bonding, resulting in the formation of dimers, or polymeric-like chains. In 1-phenylazo-2-naphthol, it is thought that the intra-molecular proton transfer occurs via formation of an inter-molecular hydrogen bond. Monahan *et al.*^{22,23} have suggested that arylazonaphthols readily form dimers and higher aggregates in solution, giving complementary evidence that the proton transfer is facilitated via inter-molecular interactions, in direct contrast to the description given by Jonsen¹ and Lycka and Macháček,³ who have suggested that formation of an intra-molecular 6-membered ring is preferred. It is probable that both mechanisms exist, and dominance of one over the other may be directly related to the crystal structure, and also to the substituents on the rings. Kuder²⁴ established approximate stabilities of the azo and hydrazo tautomers for a series of hydroxyarylazo compounds by the application of the Hückel molecular orbital method. Terms were included to allow for the possible formation of intra- and / or inter-molecular hydrogen bonding. These calculations reproduce the experimental trends observed via NMR^{1,25}, UV/ Vis^{26,27} and IR²⁸ techniques. Additionally, it was observed that dimer formation produced a three times greater stabilisation for a hydrazo-hydrazo dimer compared to an azo-azo dimer. Applying similar considerations to the sulphonic acid phenylazobenzenes would result in an understanding of their structures.

The crystal structure for the acid-base indicator methyl orange (Sample VI above) is one of only two reported in the literature for this class of dyes.²⁹ It was present as the monohydrate monoethanolate form, and the co-ordination of the sodium atom is distorted octahedral. The octahedron is made up of two water

molecules, three sulphate oxygen atoms (each from a different molecule) and the oxygen atom of the ethanol molecule. These octahedra hydrogen-bond together to form chains, creating a two-dimensional plane as shown in Figure 3. The present samples do not contain solvent co-crystals, and similar structures are therefore unlikely to be present for the salts in the present investigation.

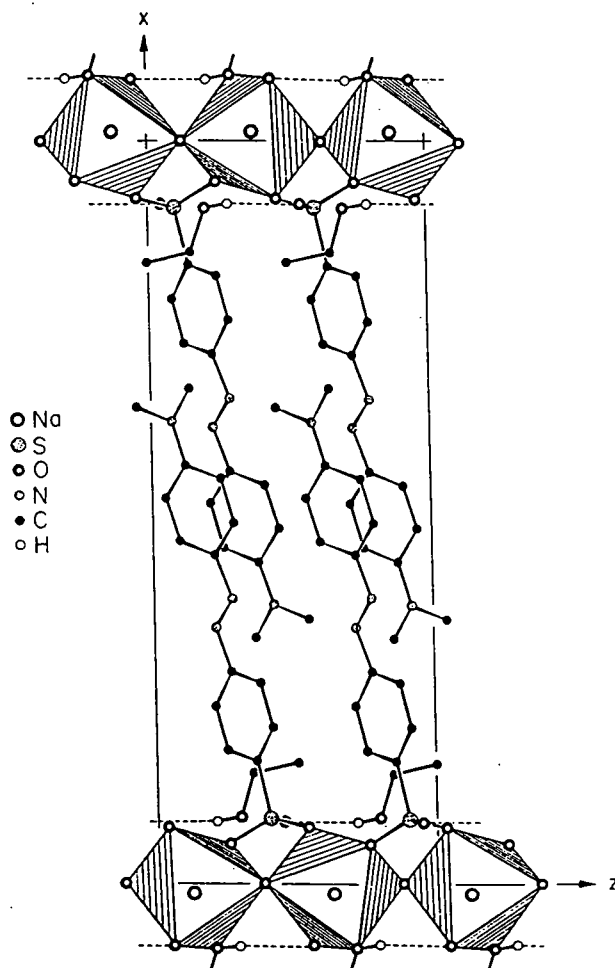


Figure 3

*Crystal structure for methyl orange monoethanol monohydrate sodium salt, viewed along *b*, showing the planar arrangement of the coordination octahedra. (Taken from ref 29.)*

The second crystal structure, which was recently reported by Ehlinger *et al.*,³⁰ is again rather important in relation to the current investigation, with two crystal forms of 4-(4-hydroxy-3,5-dimethylphenylazo)-benzenesulphonic acid being presented. Both systems are monoclinic ($P2_1/c$) with one water molecule being associated with each dye molecule. The important point is the fact that there is extensive hydrogen bonding between the SO_3H group and the azo group. The proton from the SO_3H group donates to the nearest azo nitrogen resulting in an azonium ($\text{N}=\text{NH}^+$) group. The OH hydroxy group interacts with two SO_3^- groups by utilising the H_2O as a bridging molecule. This dye is the first of its kind isolated in the solid state (with supporting crystal data) and NMR studies do not appear to have been carried out so far on this system. This structure may, however, represent what is possible in some of the free sulphonic acid systems under investigation here, where strong intermolecular contacts are expected.

The assignments of the ^{13}C solid-state NMR spectra were made by comparison with the solution assignments for the azo structures, and also by comparison with previous literature assignments for analogous compounds in the solid state. Rather than tabulating the assignments in a fashion similar to the solution-state results, each molecule will be treated individually, with a corresponding discussion of the structure. Dipolar-dephasing spectra were recorded to distinguish between the protonated and non-protonated carbons.

I. 4-phenylazobenzene sulphonic acid

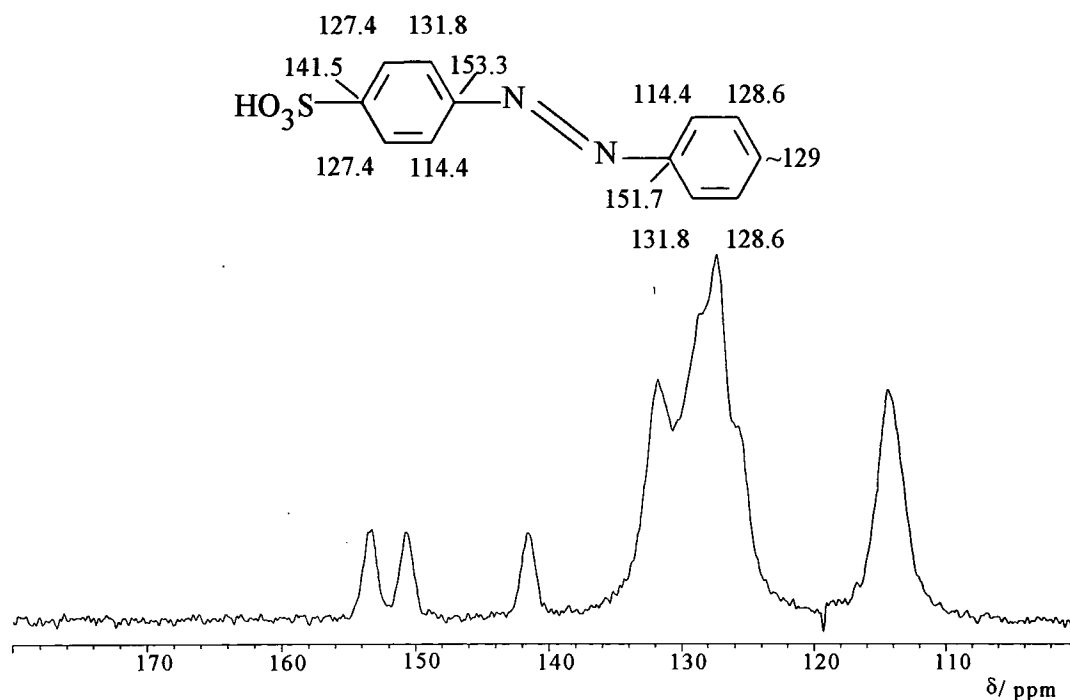


Figure 4

¹³C CP / MAS spectrum of I obtained at 75 MHz, with 2500 transients, a 2 s recycle delay, a 2 ms contact time, and a spin rate of 8300 Hz.

Under normal operating conditions one sets the Hartmann-Hahn matching using slow-spinning adamantane where the profile is broad. At faster spin rates the profile breaks up into a series of sidebands, which are more pronounced for quaternary carbons. Consequently, the three high-frequency peaks are less intense than one would expect. It was expected that this parent sulphonic acid would be the simplest to assign, but this proved a rather optimistic assumption, because when compared to the solution shifts one resonance moves from ~150 ppm to 141.5 ppm. This has been tentatively assigned to the *ipso*-carbon C4, with this position being

highly sensitive to the inter-molecular interactions. All the other shifts are indicative of the presence of the azo form.

IIa. and IIb Sodium 4-[4'-hydroxyphenylazo] benzene sulphonate dihydrate.

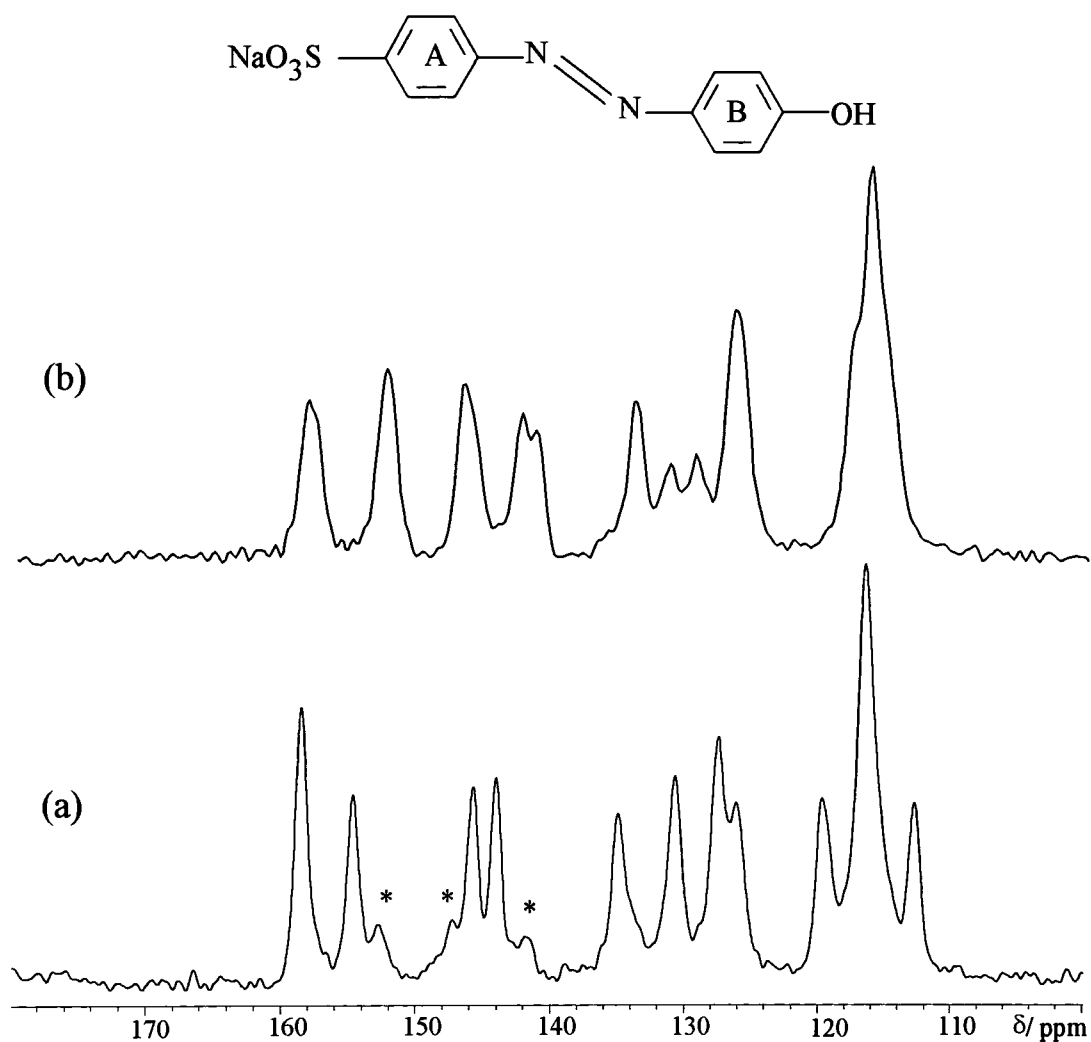


Figure 5

^{13}C CP / MAS spectra of a/ IIa obtained at 75 MHz, with 104 transients, a 60 s recycle delay, a 1 ms contact time, and a spin rate of 4500 Hz and b/ IIb obtained at 50 MHz; with 476 transients, a 10 ms contact time, a 5 s recycle delay, and a spin rate of 5 kHz.

Two separate samples of this compound were analysed, one being a reference sample supplied by *Zeneca* (IIa), and the other (IIb) being enriched with ^{15}N at the β - azo nitrogen. The two samples produced different ^{13}C CP/MAS spectra, with their respective assignments given in Table 4. The small peaks in Figure 5a, labelled by asterisks, actually correlate to the large peaks in Figure 5b, which is highly suggestive that two crystal forms (polymorphs or hydrates) exist in IIa. IIb is actually present as the dihydrate as determined from elemental analysis. Interestingly, heating IIa to $80\text{ }^\circ\text{C}$ causes a change in the spectrum, and it then appears very similar to the room temperature spectrum of IIb, which could possibly be attributed to a different mode of binding of the water hydrate molecules. Care should be taken in trying to interpret the spectra in terms of signal intensities, because the signals for these samples all have very different cross-polarisation dynamics, and this feature should be more fully investigated for a proper understanding of this system. The assignments given are tentative, and several could be interchangeable. However, they do show the existence of the azo tautomer by consideration of the C-OH signal at ~ 159 ppm.

Ring A	1	2	3	4	5	6
IIa	154.7	130.7	127.4	145.7	126.1	112.7
	152.8			147.3		
IIb	152.5	129.6	126.5	146.7	126.5	116.0*
Ring B	1'	2'	3'	4'	5	6'
IIa	144.0	119.6	116.4	158.5	116.4	134.9
	141.8					
IIb	142.0	116.0*	116.0*	158.4	116.0*	133.9

Table 4

*¹³C assignment for the solid samples of IIa and IIb. * indicates that a broad resonance was observed, and all the relevant signals were assigned to the centre of that peak.*

III. 4-[4'-hydroxyphenylazo] benzene sulphonic acid. (^{15}N β -labelled)

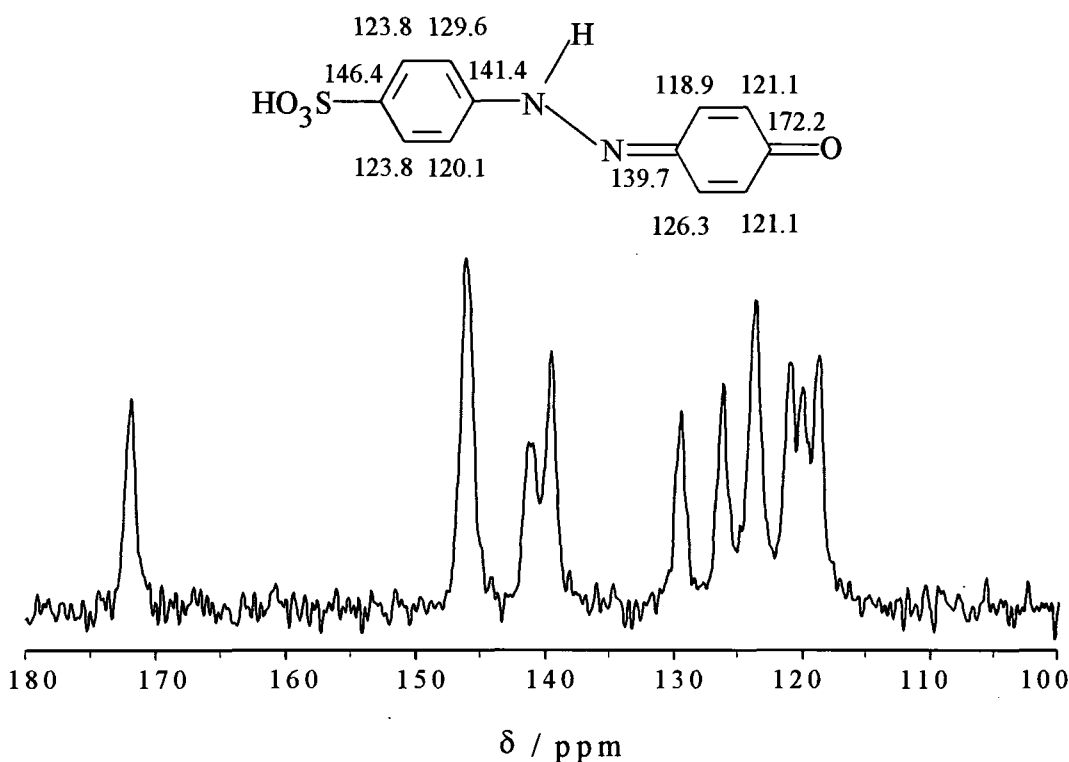


Figure 6

^{13}C CP / MAS spectrum of III obtained at 50 MHz, with 200 transients, a 2 s recycle delay, a 7 ms contact time, and a spin rate of 5 kHz.

Unlike its respective sodium salt, the spectrum of this compound strongly suggests it exists as the hydrazo tautomer, with one set of sharp lines, indicating that one distinct crystal form is present. Low-frequency shifts of the C1, C4 and C1' are all indicative of this form, in addition to the C4' high-frequency shift resulting from the quinoid structure (as drawn).

Further evidence of the structural changes between II and III has been supplied from the techniques of solid-state Raman spectroscopy and solid-state

visible spectroscopy. As mentioned previously a large bathochromic shift, in the visible spectrum, is generally observed in going from the azo to the hydrazo tautomer. Compound IIa produced a peak at 350 nm, which is attributed to the presence of the azo form, and a weak shoulder at ~480 nm which may be from a small fraction of the hydrazo form not observed in the NMR analysis. Also, III produced the same two bands with approximately equal intensity, suggesting that the a larger contribution comes from the hydrazo form in comparison to IIa. Figure 7 shows the comparison between IIa and III.

Absorbance

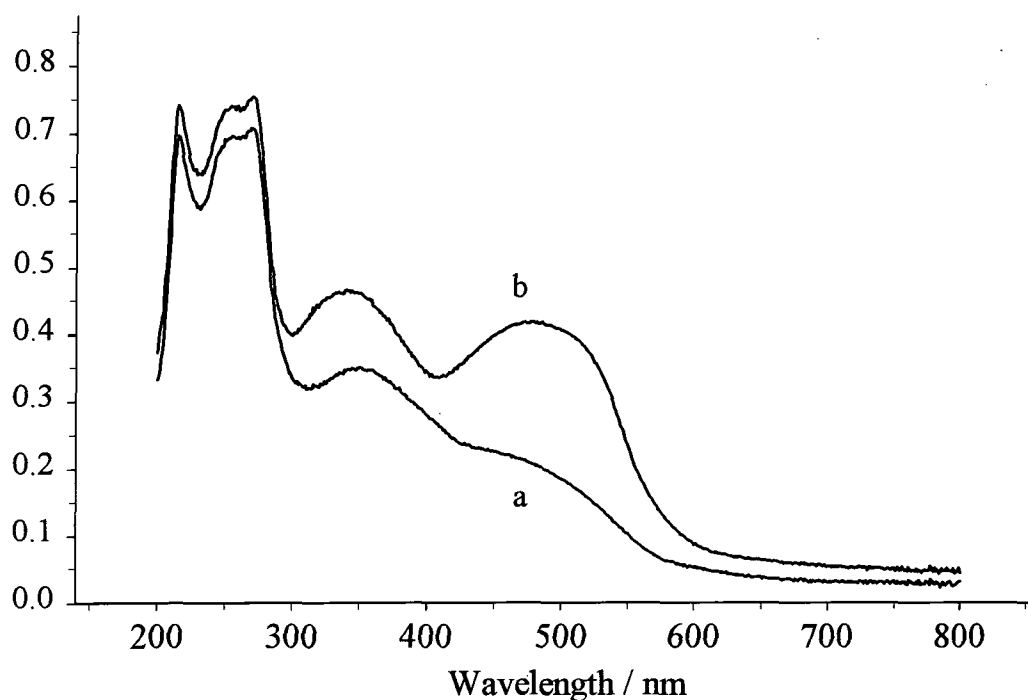


Figure 7

UV / Vis spectra of a/ IIa and b/ III recorded in the solid state. Spectral features below 300 nm should be ignored.

The Raman spectra are simpler to understand than the UV/ Vis spectra. Saito *et al.*³¹ observed a decrease in frequency of the Raman band due to the N=N stretching vibration in p-hydroxyazobenzene-sulphonic acid upon dissolution in strongly basic solution, and attributed it to a reduction of the order of the N-N bond. Thus, deprotonation of the phenolic OH group, forming the dianion (the sulphonic group is already deprotonated) results in a resonance structure between the azo and the quinoid structures. A comparative study by Chattopadhyay *et al.*³² showed the same effects, with similar conclusions. Using the assignments given by Saito,³¹ Chattopadhyay³² and Gregory³³ it was possible to assign some of the important bands in the Raman spectra for IIa and III. The Raman spectra are shown in Figure 8, with the corresponding assignments given in Table 5. The low-frequency shift of 71 cm^{-1} and the reduction in intensity of the triplet at 1100 to 1200 cm^{-1} indicates the increased proportion of the hydrazo form for III as compared to IIa.

Sample	IIa	III
Ring stretches	1590+1610	1595+1625
N=N	1440	
N-N		1205
Ph-N=	1187	
C=N		1370
C-N (hydrazo)		1171
C-N(azo)	1148+1123	

Table 5

Observed wavenumbers (cm^{-1}) and corresponding assignments for the Raman spectra for the solid samples of IIa and III.

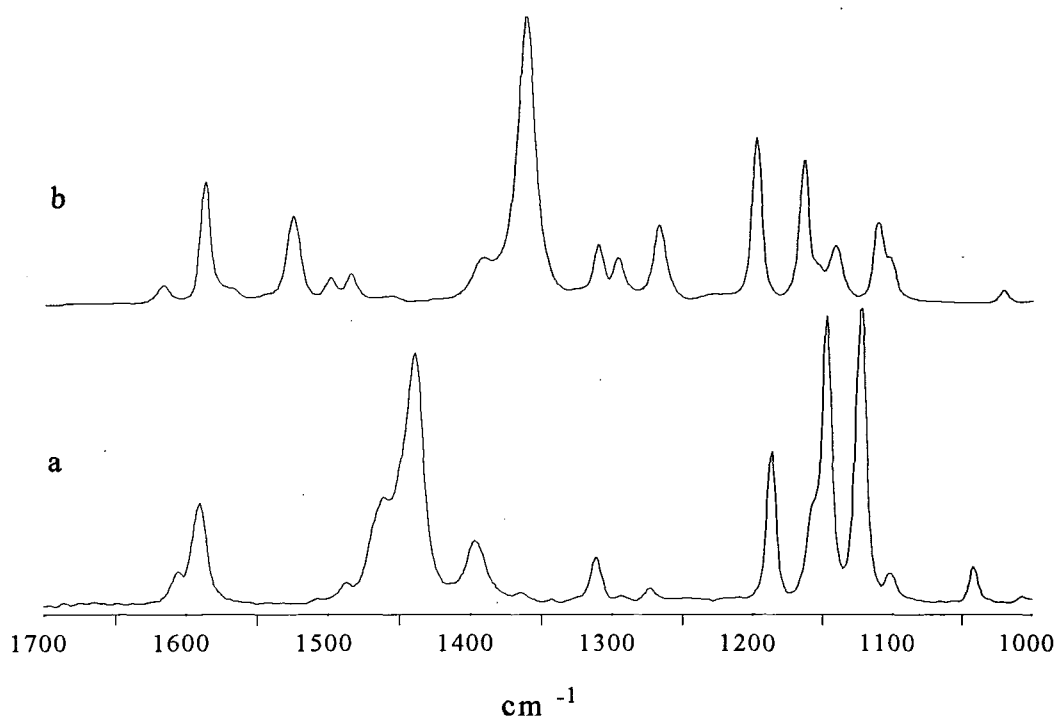


Figure 8

Solid-state Raman spectra for a/ IIa and b/ III.

IV. Sodium 4-[2'-methyl, 4'-hydroxyphenylazo] benzene sulphonate.

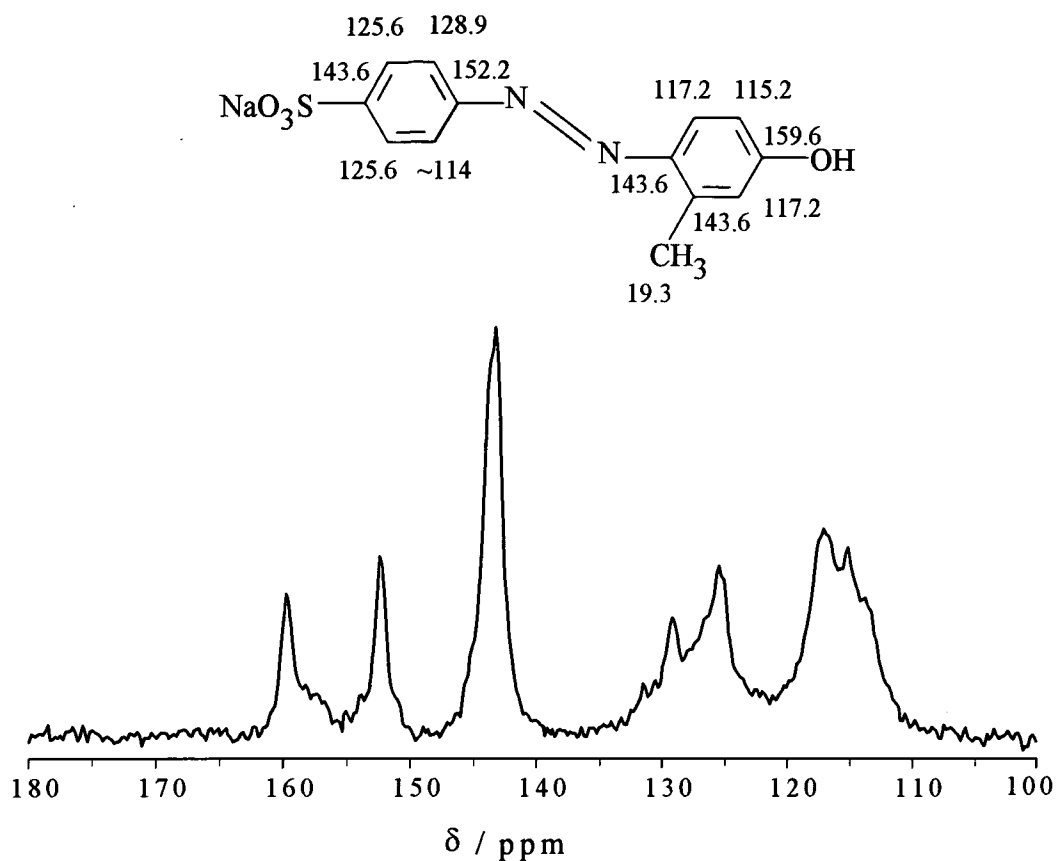
(^{15}N β -labelled)

Figure 9

^{13}C CP / MAS spectrum of IV obtained at 50 MHz, with 108 transients, a 5 s recycle delay, a 4 ms contact time, and a spin rate of 5 kHz.

Steric hindrance from the *ortho*-methyl group forces the *trans*-orientation to be observed. There is no observed structural change in going from solution to the solid. However, all of the hydrogen-carrying carbon resonances are broad, indicating that some motional process may be present, resulting from intermediate averaging of two conformations of the benzene rings. The spectral broadening may

possibly arise from incomplete decoupling via interference of the decoupler and molecular motion.

V. 4-[2'-methyl, 4'-hydroxyphenylazo] benzene sulphonic acid. (^{15}N β -labelled)

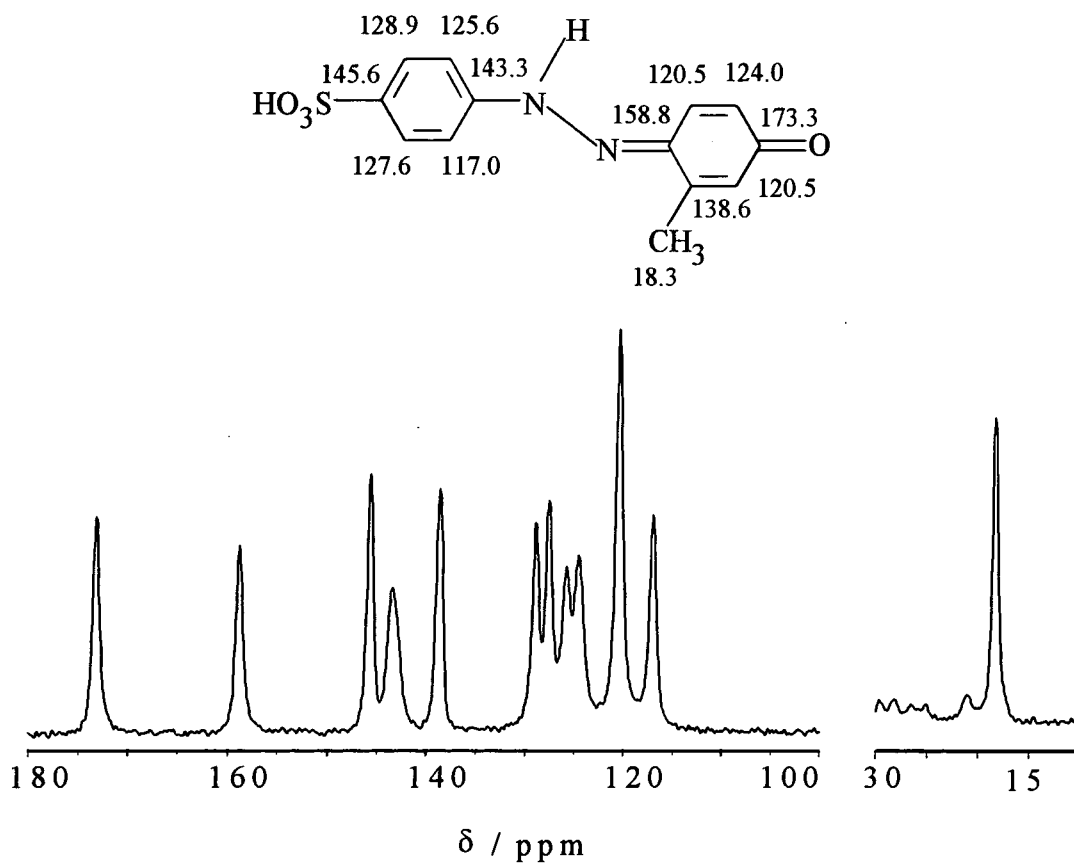


Figure 10

^{13}C CP / MAS spectrum of V obtained at 50 MHz, with 640 transients, a 5 s recycle delay, a 8 ms contact time, and a spin rate of 5 kHz.

As with III, the hydrazo form is observed, with the methyl group being present in the *trans*-orientation. Surprisingly though, one quaternary resonance moves quite significantly from the expected value. This has been assigned to a high-frequency shift of the C=N, C1', resonance, as it is known that C=N shifts can vary quite significantly. The solid-state Raman spectrum shows similar features to that of III, indicating that the two structures are similar, the C=N stretch being found at 1382 cm^{-1} , compared to 1369 cm^{-1} for III.

VI. Sodium 4-[2',4'-dihydroxyphenylazo] benzene sulphonate. (^{15}N β -labelled)

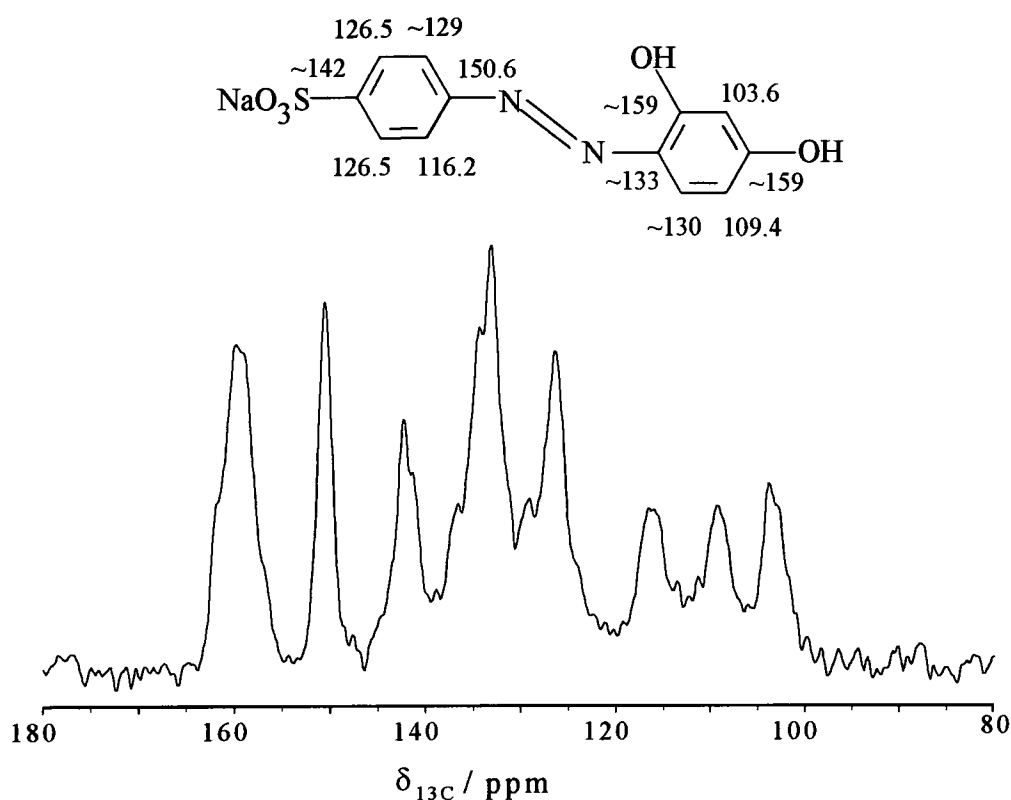


Figure 11

^{13}C CP / MAS spectrum of VI obtained at 50 MHz, with 108 transients, a 5 s recycle delay, a 4 ms contact time, and a spin rate of 5 kHz.

The poor resolution of this spectrum makes a positive assignment very difficult, but it is again clear, as for the other salts, that it is present in the azo form (judged by the shift of the phenolic carbons). Intra-molecular hydrogen bonding is suggested from the shift of C2', which would be ~8 ppm higher if rapid rotation of the phenyl ring was present.

VII. 4-[4'-dihydroxyphenylazo] benzene sulphonic acid. (^{15}N β -labelled)

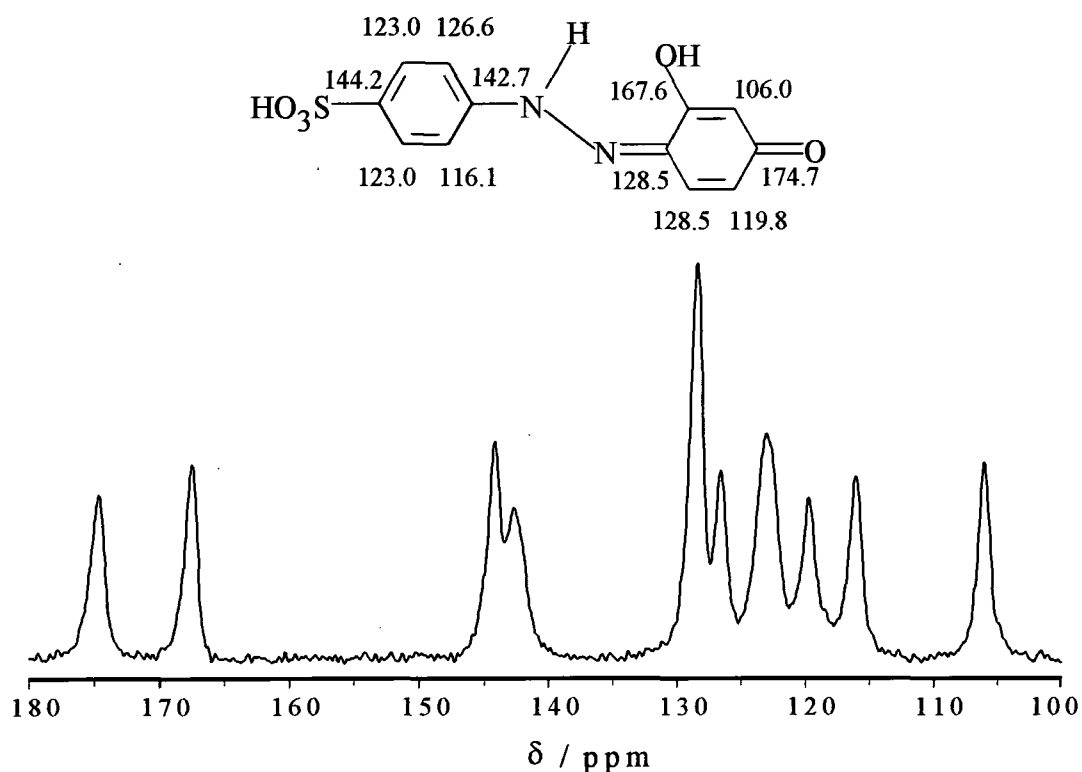


Figure 12

^{13}C CP / MAS spectrum of VII obtained at 50 MHz, with 200 transients, a 5 s recycle delay, a 7 ms contact time, and a spin rate of 5 kHz.

The spectrum obtained for this sample, Figure 12, was one of the best for this range of dyes. Significantly narrowed lines were observed in comparison to the salt, simplifying the assignment. Strangely though, it appeared that one carbon signal was not realised. The dipolar dephasing spectrum, with a standard 40 μ s dephasing window, did not resolve the problem. To try to locate the lost CH resonance a variable dipolar dephasing experiment was carried out, with the results displayed as a stacked plot in Figure 13. It should be remembered that intensities are not reliable via CP, but within a single experiment it is possible to correlate changes in intensity. The variable dipolar dephasing experiment showed that several resonances decayed rather rapidly, as one would expect, followed by a slight increase in signal intensity when the dephasing time was equal to the rotor period. However, the resonance at 128.5 ppm decayed initially, but stayed fixed at ~60% of its original intensity. This is proof that the 128.5 ppm line is composed of two signals, one an aromatic CH, and the other a quaternary signal, which were assigned to the C6' and C1' carbon atoms respectively. The final assignment all of the resorcinol ring carbons has been made by considering a 50:50 equilibrium of the azo and hydrazo forms, with the hydrazo shifts being taken from Fedorov's analysis of similar resorcinol derivatives.¹⁰ The lack of reference samples for azobenzene resorcinol derivatives prevents an accurate estimation of the actual equilibrium constant. As shown from the two crystal structures discussed earlier it is clear that several possible combinations of intermolecular contacts are possible, each of which have profound effects on the ¹³C NMR spectral features. Hence, other possible structures, not so far proposed may explain the NMR spectra better.

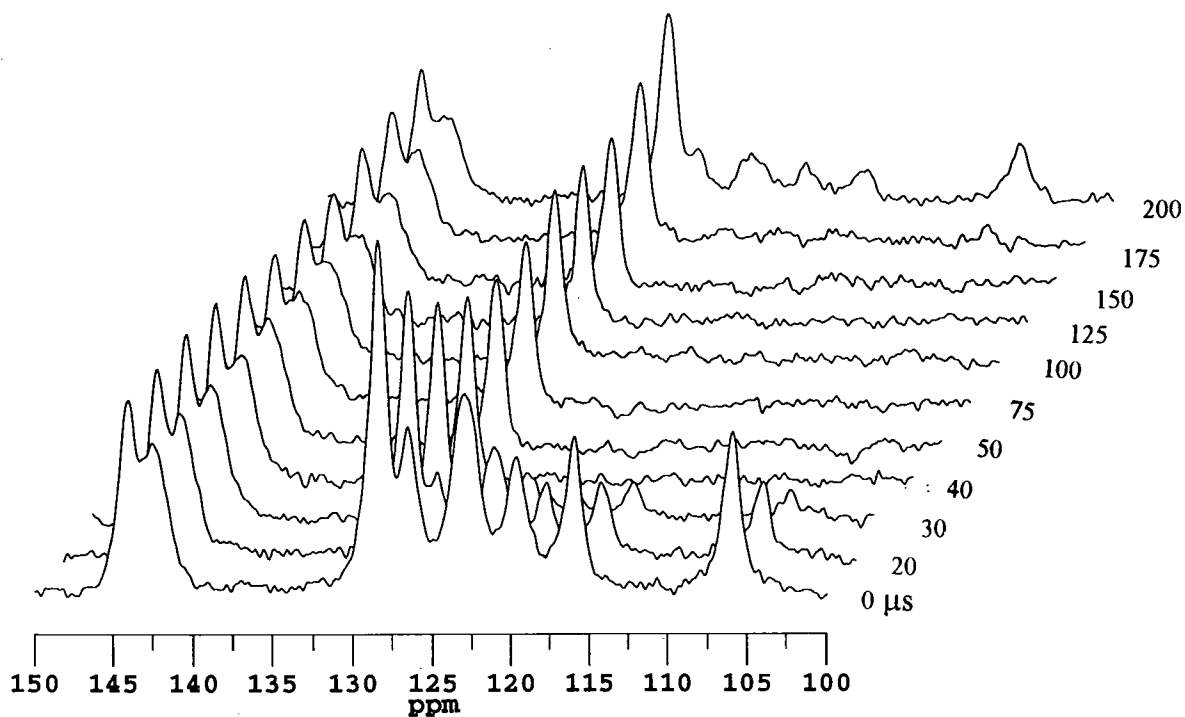


Figure 13

Stacked plot of the ^{13}C CP/MAS, variable dipolar dephasing experiment of VII, obtained with a Hahn echo. The echo time was 200 μs which is one rotor period i.e. corresponding to a spin rate of 5 kHz.

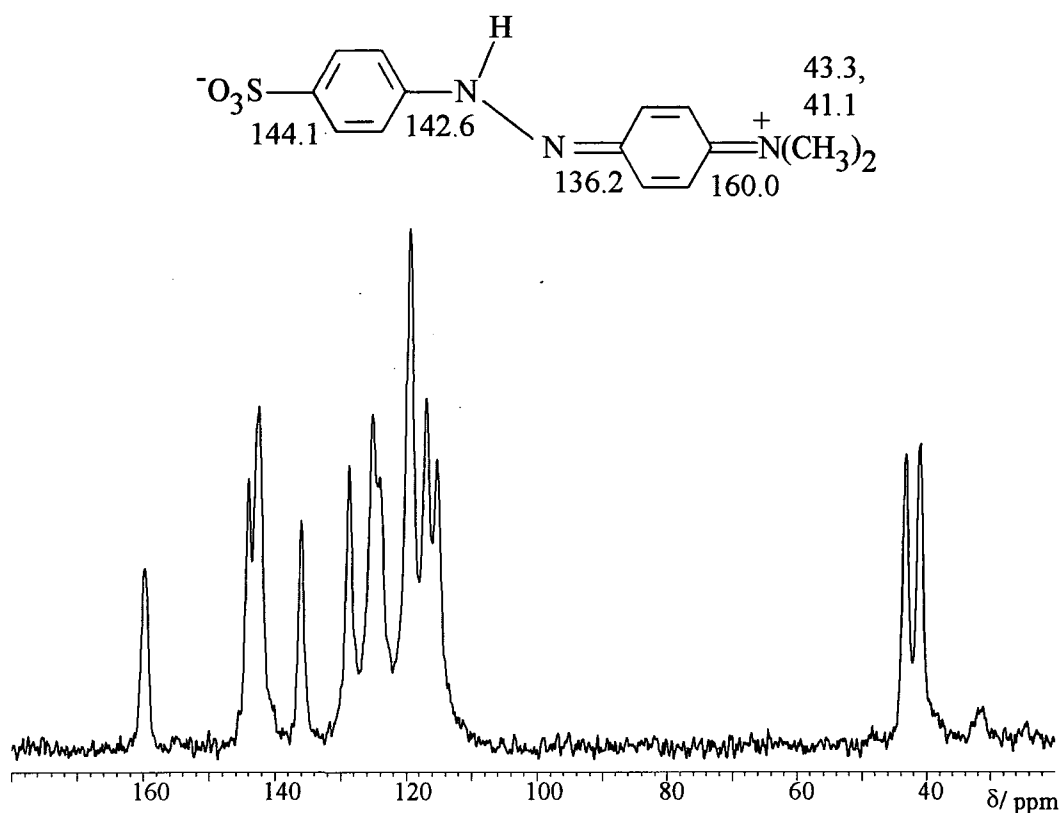
VIII 4-[4'-(dimethylamino) phenylazo] benzene sulphonic acid.

Figure 14

¹³C CP / MAS spectrum of VIII obtained at 75 MHz, with 1550 transients, a 4 s recycle delay, a 3 ms contact time, and a spin rate of 8.43 kHz.

All of the ¹³C resonances could not be assigned for this sample, however, the quaternary signals were successfully assigned. The signals associated to the protonated carbons were: 115.5, 117.1, 119.7, 124.3, 125.3 and 128.9 ppm. The C1 resonance frequency of 142.6 ppm suggests that the hydrazone tautomer is present. Additionally, the presence of two separate CH₃ signals with a 2 ppm splitting infers that there is hindered rotation of the dimethylamino group, presumably due to the formation of a C, N double bond, as shown above.

IX. 4-[2'-methyl, 4'-amino phenylazo] benzene sulphononic acid, sodium salt.

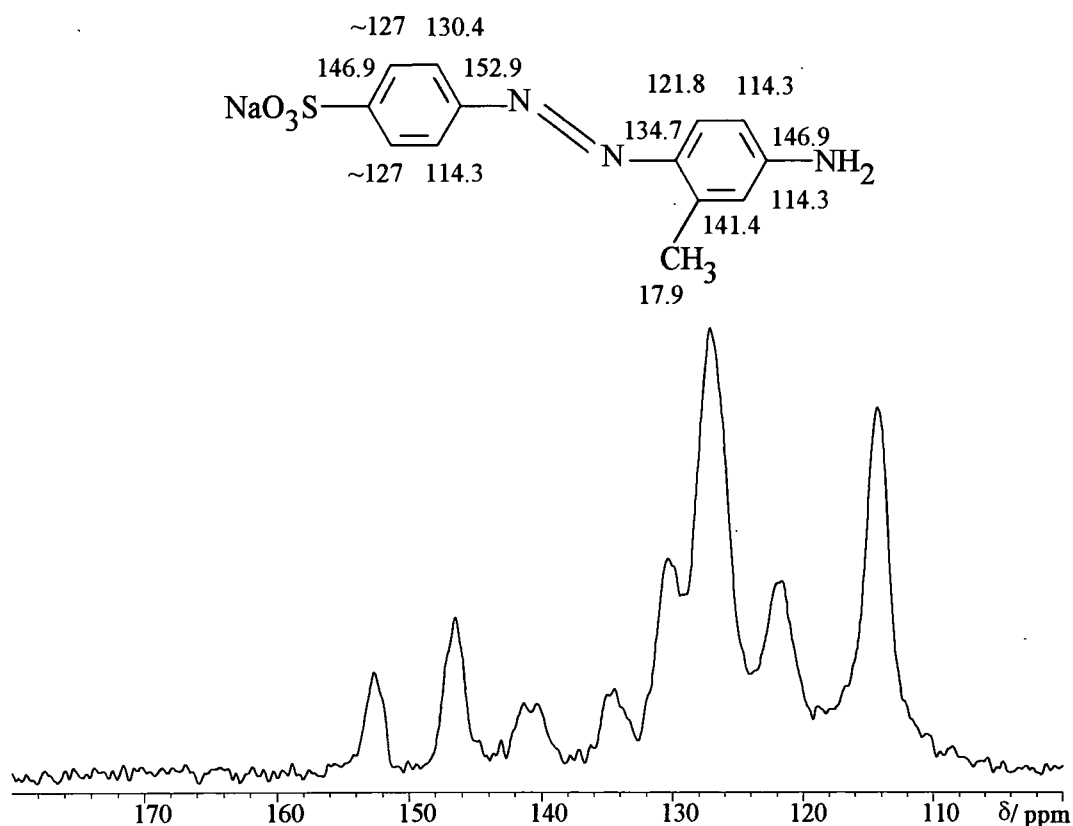


Figure 15

^{13}C CP / MAS spectrum of IX obtained at 75 MHz, with 1100 transients, a 2 s recycle delay, a 5 ms contact time, and a spin rate of 8.3 kHz.

The assignment given above indicates that IX is present as the azo tautomer, with the CH₃ group locked in a conformation such that steric hinderance from the azo α nitrogen lone pair orbital is minimised. Weak quaternary signals were observed due to the high spin-rates used, as already discussed.

5.2.2 N-15 NMR.

The effect of the substituents upon the electron density distribution in similar conjugated systems has been well characterised via visible spectroscopy, and a significant variation was observed.³⁴ Nitrogen-15 NMR is very sensitive to small changes in electron density, and thus would be useful in analysing these sulphonic acid azobenzene systems. The isotropic shifts for azo nitrogens are particularly difficult to detect at natural abundance in the solid state, due to the huge SA for the signals, diluting the signal over many sidebands under MAS conditions. Too fast a MAS rate will reduce the number of sidebands, but as was observed from the ¹³C experiments several of the samples show modulation of the Hartmann-Hahn matching profile. Setting the matching condition accurately is critical for these measurements if one spins at high rates. All of the spectra recorded in the section were acquired at moderate spin rates of 5 kHz or less, thus alleviating the problem with HH matching breakup. The assignments for the ¹⁵N isotropic shifts are given in Table 6. Some of the entries in Table 6 were obtained at natural abundance, and the error in the shifts is rather large, $\sim\pm 1$ ppm. The labelled samples have chemical shifts quoted with a significantly higher accuracy, due to the increased signal-to-noise ratio. The calculated entries for the azo compounds were obtained by comparison to the SCS values given in Table 6, along with the SCS parameter found for the SO₃⁻ group in I. This ¹⁵N SCS has not been reported in the literature, and was determined to be -12 ppm for the α nitrogen and +4 ppm for the β nitrogen.

Sample No.	N α	N α (calc.)	N β	N β (calc)	N α - N β
I	118.7 n	118.7	135.3 n	135.3	16.6
II	110 n	98.7	130 (122.9)*	129.3	20.0
III	-131.5 n		40.9 *		172.1
IV			128 (122.9)*		
V	-146.7 n		31.2 *		177.9
VI		37.7	107 (111.3)*	126.3	69.3 ^a
VII	-122.5 n		5.8 *		128.3
VIII ^b	-173.3 n		2.1 n		175.4
IX ^c	126.7 n		122.2 n		4.5

Table 6

*Assignment of ¹⁵N isotropic shifts in the solid state. The value in parenthesis is for the solution(given in ppm) in DMSO-d₆. The calculated values were determined as discussed in the text. n indicates that the peak is observed at natural abundance, while * indicates observation of the labelled signal.*

^a |N α - N β | determined from theoretical N α and experimental N β .

^b N(CH₃)₂ δ_{N-15} = -245.8 ppm. ^c NH₂ δ_{N-15} = -328 ppm

From the results it is easy to see that I, II, IV, VI and IX are all present as the azo tautomer. The planarity of the aromatic rings affect the ¹⁵N shifts of the azo nitrogens in a manner which is dependant on the paramagnetic contribution. Mixing of the angular momentum components for the ground states and the excited states results in a higher paramagnetic contribution, *i.e.* a shift to higher frequency. If the energy difference between the levels involved increases, then the mixing will be reduced, as would be expected if stabilisation of the bonding orbital by hydrogen

bonding was present. Additionally, lone pair orbitals, of OH and NR₂ groups for example, can overlap with the aromatic π orbitals, creating further stabilisation. This is why the dihydroxy salt, VI, shows an approximate 20 ppm low-frequency shift in relation to the other azo resonances for the β site. In comparison with the theoretical shifts, using solution-state SCS values, a large deviation to low frequency is also observed. Lycka observed similar low-frequency shifts in going from solution to solid,¹⁵ and attributed them to an increased proportion of the hydrazo tautomer. The ¹³C CP/MAS spectra do not show the introduction of any hydrazo tautomer. This site is very sensitive to the strength of the hydrogen bond, and consequently small changes in the structure significantly influence the observed shift. It is clear that the sample is present in the azo form with a hydrogen bond. The hydrogen bonding cannot be proven to be intra- or inter-molecular since the α resonance cannot be observed.

As an example of a ¹⁵N spectrum obtained at natural abundance, Figure 16 shows the CP/MAS spectrum of VIII. The two large low-frequency peaks are from the N α -H resonance (-183 ppm) and the Ar-N(CH₃)₂ (-245.8 ppm), and appear stronger due to the small SA. It should therefore be noted that it is very difficult to obtain signals from the non-protonated azo ¹⁵N nuclei at natural abundance, particularly when the ¹H T_{1 ρ} is rather short (which can happen for several classes of organic materials, and especially with many polymers).

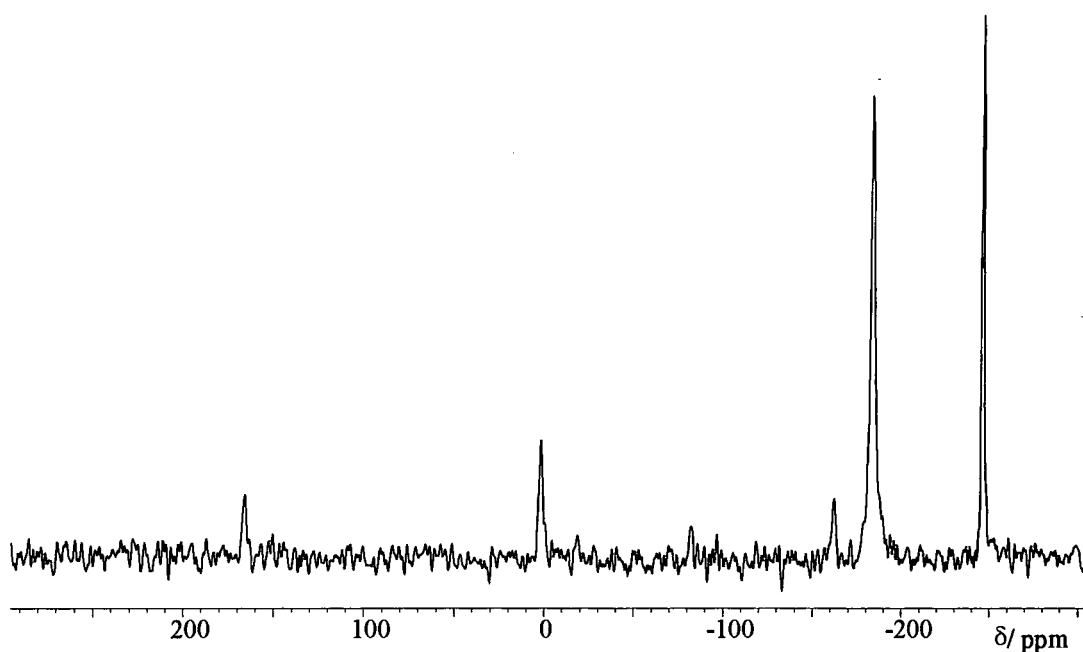


Figure 16

¹⁵N CP/MAS spectrum of VIII obtained at 30.4 MHz, with 7392 transients, a contact time of 5 ms, a recycle delay of 7 s and a spin rate of 5 kHz.

For samples VIII and IX knowledge of the shifts for N,N-dimethylaniline (-336 ppm) and aniline (-323 ppm) are required to determine if Zwitterion formation occurs. Substitution of these anilines with a *para*-azo group does not significantly effect the ¹⁵N resonance frequencies. Protonation of anilines result in low frequency shifts, however, and for VII a high frequency shift of ~90 ppm was observed, which indicates that there is an increased double bond character for the nitrogen atom. Thus, the proton from the sulphonic acid group is now associated with the α azo nitrogen, resulting in the hydrazone tautomer. This differs from that determined from ¹⁵N NMR by Kuroda¹⁶ where the proton was associated with both the amino and azo group as shown in Figure 17, with the ammonium resonance form being favoured. The assignments for both the ¹³C spectra and for the N α and N β



resonances in the ^{15}N spectra are consistent with the hydrazone tautomer. Nuclear Overhauser enhancements cannot generally be observed in solid state ^{15}N spectra, and consequently the degree of protonation cannot be determined by NOE enhancements, as in solution.

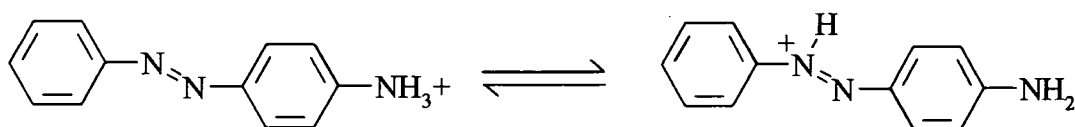


Figure 17

The three β - ^{15}N labelled free-acid samples all provide evidence from the ^{15}N CP/ MAS spectra that the hydrazo form is present, or at least that there is a fast equilibrium which significantly favours the hydrazo form. Variable temperature analysis could give some insight into the equilibrium position of the azo / hydrazo tautomerism, if one exists and is found to be mobile. For III, V and VII no such equilibrium was found. The ^{13}C and ^{15}N CP/MAS spectra were virtually identical over the temperature range, $-100\text{ }^\circ\text{C}$ to $+80\text{ }^\circ\text{C}$. The differences between the α - ^{15}N and β - ^{15}N are ~ 175 ppm for both III and V, which are comparable to those observed by Lycka.¹⁵ The splitting for VII is 128 ppm, which is significantly smaller than III, V and VIII. If one considers a mixture of the azo / hydrazo tautomers in rapid exchange then, using the values for the splitting of 70 ppm (azo, determined in Table 6) and 170 ppm (hydrazo), an $\sim 50\%$ contribution from the azo tautomer can be determined. This is identical to the ^{13}C results given earlier. However, it appears that this explanation does not fully explain the results of the variable temperature analysis. A shift of the resonance would be expected, because the equilibrium would most probably be dynamic, as shown by Lycka.¹⁵

The ^{15}N CP/MAS spectra were obtained at various field strengths, and show the presence of a perturbation to the lineshape which is observed at 20 MHz, but is negligible at 40 MHz. This perturbation, which was observed as a splitting of between 35 Hz and 45 Hz at 20 MHz, depending on the sample, can be attributed to the phenomenon of residual dipolar coupling (RDC) for these samples. No data have been published where anyone has observed this phenomenon for ^{14}N - ^{15}N coupled spins in a hydrazo spin system, which is not surprising. The β - ^{15}N site exhibits a very large SA which renders it very sensitive to the magic angle. The spinning sidebands span approximately 800 ppm, over twice that of NH_4NO_3 which was used to set the angle. Hence, it is twice as sensitive to errors in setting the magic angle. Even small errors will cause broadening of the signals, and the splitting is therefore lost. For example, for an error of 0.1° , a broadening of ~ 80 Hz would be observed. Older probes may not have such sensitive angle adjustment as those used for the new Pencil rotors. On the Chemagnetics spectrometer the angle is slightly dependent upon the temperature, and a broadening was observed in reducing the temperature. It was possible to reset the angle and reintroduce the splitting. Challoner *et al.*³⁵ have observed this splitting in the linear benzene diazonium cation. Jonsen¹ and Lycka¹⁵ did not observe any splitting in their hydrazo compounds, even though a ^{15}N - ^{14}N isolated spin system was present in their selectively labelled samples, due to the large linewidths, in excess of 200 Hz in Jonsen's case, and the presence of a crystallographic splitting in Lycka's work. Figure 18 shows the comparison between the ^{15}N CP/MAS spectra obtained at 40 MHz and 20 MHz for the three samples.

Strangely, the 2:1 asymmetric doublet, after deconvolution, was found to be a 3:2 doublet for V, and this cannot be explained properly in terms of RDC. If the origin of the splittings was of a crystallographic nature then one would expect them to be retained at the higher field strengths. Assuming the hydrazo tautomer is solely present it is possible to obtain the N-N bond length. The splitting between the two lines is given by:

$$S = \frac{9D\chi}{20\nu_N} \left(3 \cos^2 \beta^D - 1 + \eta \sin^2 \beta^D \cos 2\alpha^D \right)$$

where, $D = \frac{\mu_0}{4\pi} \frac{\gamma_{N14} \gamma_{N15} \hbar}{4\pi^2 r_{NS}^3}$ is the dipolar coupling constant, expressed in Hertz, χ

is the ^{14}N nuclear quadrupolar coupling constant, η is the asymmetry of the electric field gradient, ν_N is the Larmor frequency for the ^{14}N nucleus, while α^D and β^D are the Euler angles defining the orientation of the EFG tensor to the molecular frame.

It should be remembered that the magnetogyric ratio of the ^{15}N nucleus is negative when one evaluates this expression.

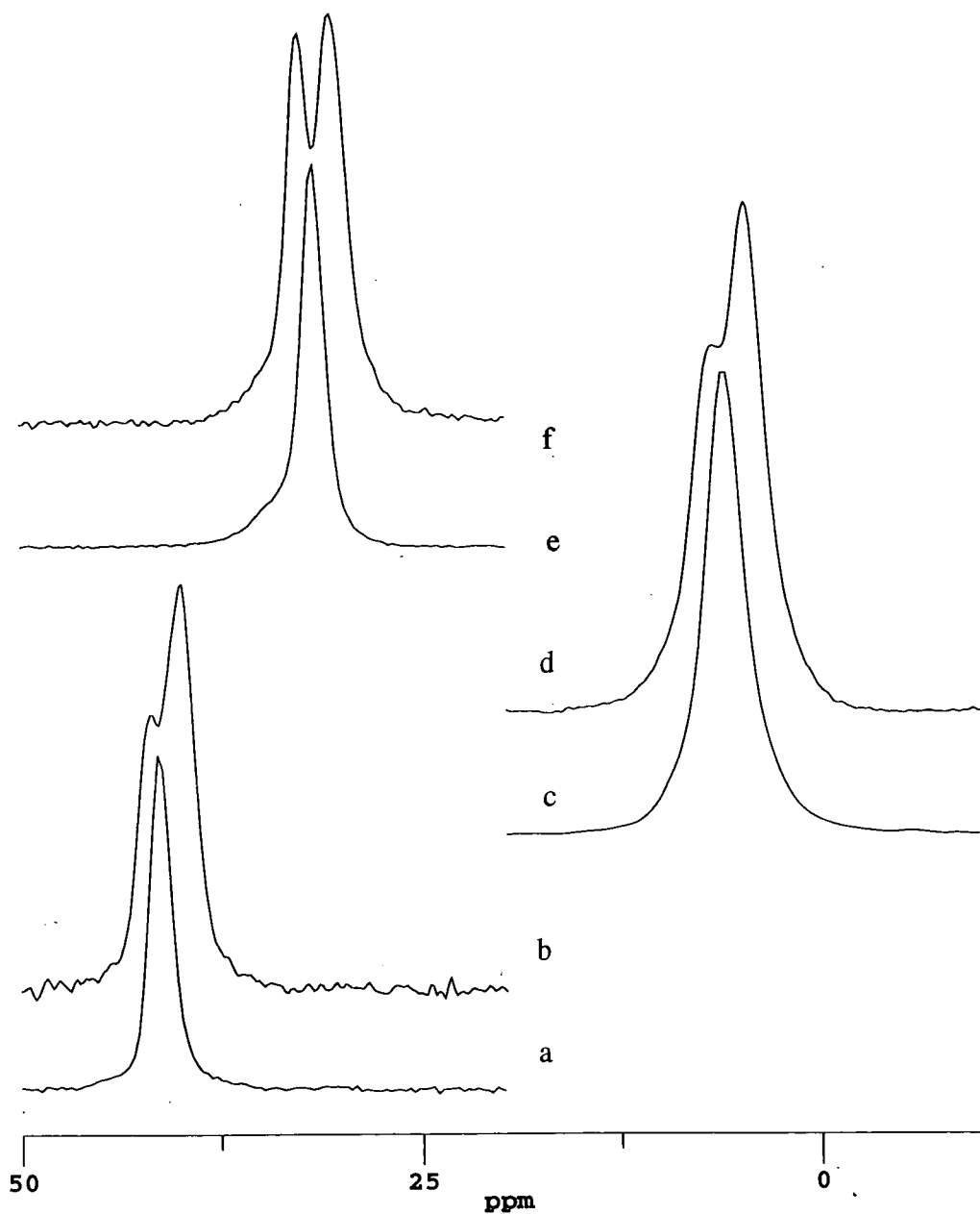


Figure 18

^{15}N CP/MAS spectra for; III a/ at 40 MHz, b/ at 20 MHz; VII c/ at 40 MHz, d/ at 20 MHz; V e/ at 40 MHz, f/ at 20 MHz. Spectra were acquired with between 40 and 128 transients, recycle delays between 2 s and 5 s, contact times between 5 ms and 10 ms, and spin rates between 3.5 kHz and 5 kHz.

One must know all of the above parameters to make an accurate estimate of the splitting, the unknowns usually being r_{IS} , χ , η , α^D and β^D . Osokin and co-workers³⁶ have previously obtained NQR parameters for some phenylhydrazones, and found that the magnitude of the amino ^{14}N nuclear quadrupolar coupling constant was $\chi = 4.68$ MHz, with an associated asymmetry of the electric field gradient of $\eta = 0.31$. Since the asymmetry is non-zero, one must be careful in the analysis of such RDC. The relative orientation of the EFG tensor, at the ^{14}N nuclear site, to the ^{15}N - ^{14}N dipolar vector must be determined if one wishes to apply the above equation. The Z_{EFG} axis will be co-linear to the orientation with the greatest electron density, namely along the lone pair. Thus, assuming planarity of the molecule, $\beta^D = 90^\circ$, *i.e.* perpendicular to the molecular plane. Two alternatives have been proposed for hydrogen-bonded N-H amino groups depending on whether 1/ the X_{EFG} axis or 2/ the Y_{EFG} axis points along the direction of the N-H bond. If the Y_{EFG} points along the N-H bond then $\alpha^D = 30^\circ$, while for X_{EFG} along the N-H bond the corresponding angle would be 120° . Therefore, using the above parameters, and the experimental splitting, it is possible to both orient the EFG tensor and evaluate the bond length.

The results are given in Table 7. From these two sets of results one can assume that the N-N bond length is between 1.3 Å and 1.5 Å, and that the Y_{EFG} axis points along the N-H bond. This result has been obtained from the facts that typical N=N double bond distances,^{29, 37, 38} as obtained for azobenzenes, are between 1.2 Å and 1.27 Å, while those for N-N single bonds in hydrazones are lie between 1.3 Å and 1.4 Å.^{39, 40} The error in estimating the bond length is actually rather significant in this case because the splitting is small. Errors as large as ± 0.05 Å for each sample

are expected. Olivieri and co-workers,⁴¹ and Garcia *et al.*⁴² have suggested that formation of a strong intra-molecular hydrogen bond may possibly result in a reduction of the nuclear quadrupole coupling constant, which would possibly allow the X_{EFG} axis to be directed along the N-H bond. However, Olivieri suggests that it is more likely that the Y_{EFG} axis lies along the N-H bond for phenylazo-naphthol, in accordance with the results found here. Interestingly, *trans*-azobenzenes show no $^{13}\text{C} - ^{14}\text{N}$, or $^{15}\text{N} - ^{14}\text{N}$ RDC, not due to the small quadrupolar coupling constants, but rather due to the relative orientations of the EFG tensor with the dipolar vector. The quadrupolar coupling constant is rather large, $\chi = -5$ MHz,⁴³ and given the N=N bond length of 1.25 Å, a splitting of ~ 5 Hz is expected (assuming an asymmetry of $\eta = 0.5$), which is far too small to be generally observed by ^{15}N solid-state NMR.

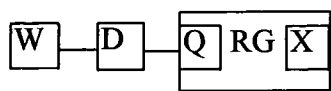
Sample	S / Hz	α^{D}	β^{D}	χ / MHz	η	$r_{\text{N-N}}$ / Å
III	37	30	90	4.68	0.31	1.32
		120	90	4.68	0.31	1.47
V	41	30	90	4.68	0.31	1.38
		120	90	4.68	0.31	1.53
VII	47	30	90	4.68	0.31	1.43
		120	90	4.68	0.31	1.59

Table 7

Estimation of the N-N bond length for the hydrazo fragment of III, V, VII for both possible orientations of the EFG tensor (as discussed in text).

5.3 The solid-state structure of a typical reactive azo dyestuff.

Reactive azo dyes contain one or more groups which are capable of forming one or more covalent bonds between a carbon atom of the dye anion, and an oxygen atom of a hydroxy group in cellulose (for example). The characteristic structural features of a reactive dye are shown schematically in Figure 19.



RG: electrophilic leaving group

Q: bridge link

X: nucleofugic leaving group

D: chromogen

W: water solubilising group

Figure 19

The sulphonic acid azobenzenes discussed previously constitute the W and D sections of the reactive dye shown in Figure 20, with its corresponding ^{13}C CP/MAS spectrum. A propyl linkage (Q) joins the chromogen (W+D) to the reactive triazene group (RG). For simplicity the molecule has been broken up into two fragments; A and B. Solution-state ^{13}C NMR suggests that there are two conformations present. No solid-state ^{13}C NMR studies have been published on any reactive dyes. The most complex dyes analysed previously by solid-state NMR have been a series of bisazo pigments.⁴⁴

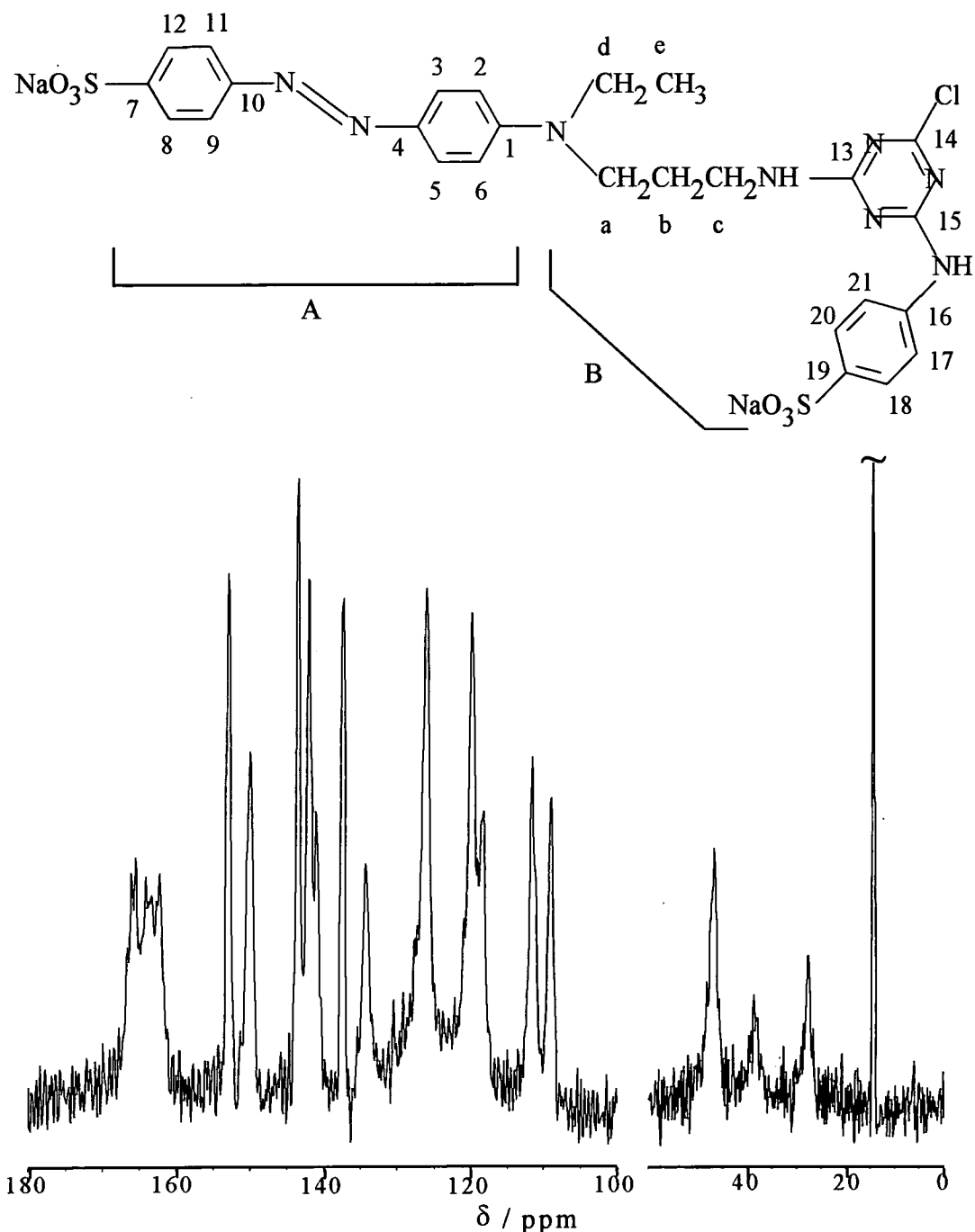


Figure 20

Molecular structure of ASG 12974/94 with corresponding numbering scheme and ^{13}C CP/MAS spectrum obtained at 50.3 MHz. The spectrum was acquired with a contact time of 6 ms, recycle delay of 10 s, 2000 transients and a spin rate of 6 kHz. Resolution enhancement was carried out by applying 20 Hz Gaussian (centre of 0.2 virtual) and -20 Hz exponential damping functions.

In comparing the solution-state and solid-state ^{13}C shifts it is apparent that there are no major structural changes, and that the structure is present as the azo form, as drawn in Figure 20. The presence of the triazene group and the several NH linkages around the molecule reduce the spectral resolution, because of ^{13}C - $^{37(35)}\text{Cl}$, and ^{13}C - ^{14}N RDC. This is most evident at ~ 160 ppm where no positive assignments can be made relating to the triazene ring. An assignment of the ^{13}C solution and solid-state NMR shifts is given in Table 8. Only six signals were observed for the protonated carbon in the ^{13}C CP/ MAS spectrum. This could probably be explained by the fact that all the protonated signals are averaged by rotations about the axes of the respective phenyl rings. From consideration of the resonance frequencies this cannot be the case. The resonance at 134.2 ppm suggests that one, or two, pairs of CH signals ortho to the azo linkage are separated due to hindered rotation. Additionally, the signal intensities appear rather anomalous when comparing the quaternary and protonated signals. This is presumably due to the fact that the proton-proton homonuclear dipolar coupling is very small, as evidenced by the narrow Bloch decay spectrum for the protons. As a consequence the Hartmann-Hahn matching profile breaks up into many narrow sidebands, and the signals may cross polarise very differently. Thus the protonated signals cannot be confidently assigned.

Fragment A			Fragment B		
Carbon No.	Solution d ₆ - DMSO	Solid	Carbon No.	Solution d ₆ - DMSO	Solid
1	150.42+150.37	150.0	13	168.52+167.87*	165.5*
2	111.23+111.27		14	165.37	163.7*
3	125.21		15	163.67+163.33*	162.2*
4	142.83	142.0	16	139.13+139.07	141.0
5	125.21		17	119.31+119.10	119.7
6	111.23+111.27		18	126.09+126.04	~126
7	152.31	152.9	19	142.25	137.4
8	121.23		20	126.09+126.04	~126
9	126.60		21	119.31+119.10	119.7
10	148.68	143.5	a	47.52	46.7
11	126.60		b	26.87+26.45	27.6
12	121.23		c	44.63	46.7
			b	38.52+38.34	38.3
			e	12.34+12.30	14.3

Table 8

¹³C solution-state and solid-state chemical shift assignments (in ppm) for the reactive dyestuff shown in Figure 20.

** indicates that assignments are interchangeable*

References.

- 1 P. Jonsen, *PhD. Thesis*, University of East Anglia, (1984).
- 2 R.K. Harris, P. Jonsen and K.J. Packer, *Org. Magn. Reson.*, **22**, 269, (1984).
- 3 A. Lycka and V. Macháček, *Dyes and Pigments*, **7**, 171-185, (1986).
- 4 M. Nepras, M. Titz, M. Necas, S. Lunak jr, R. Hrdina and A. Lycka, *Coll. Czech. Comm.*, **53**, 213, (1988).
- 5 J. Kelemam, S. Moss, H. Sauter, T. Winkler, *Dyes and Pigments*, **3**, 27, (1982).
- 6 D.F. Ewing, *Org. Magn. Reson.*, **12**, 499, (1979).
- 7 A. Lycka, *Coll. Czech. Comm.*, **47**, 1112, (1987).
- 8 A.M. Chippendale, A. Mathias, R.K. Harris, K.J. Packer and B.J. Say, *J.C.S. Perkin Trans II*, 1031, (1981).
- 9 L.A. Ferorov, P. Savarino, V.I. Dostovalova, G. Viscardi, R. Carpignano and E. Barni, *Zunal. Strukt. Khimii*. **33**, 91-101, (1992).
- 10 L.A. Fedorov, A.I. Rebrov and S. Lainfang, *Dyes and Pigments*, **18**, 207-226, (1992).
- 11 L.A. Fedorov, *J. Anal. Chem. USSR.*, **40**, 23, (1985).
- 12 J. Keleman, *Dyes and Pigments*, **2**, 73-91, (1981).
- 13 A. Lycka, *Org. Magn. Reson.*, **15**, 17, (1981).
- 14 A. Lycka, D. Snobl, V. Macháček and M. Vecera, *Org. Magn. Reson.*, **16**, 17, (1981).
- 15 A. Lycka, J. Jirman, B. Schneider and J. Straka, *Magn. Reson. Chem.*, **26**, 507-510, (1988).
- 16 Y. Koruda, H. Lee and A. Kuwae, *J. Phys. Chem.*, **84**, 3417, (1980).
- 17 Y. Kosugi and T. Takeuchi, *Org. Magn. Reson.*, **12**, 435, (1979).
- 18 Y. Kosugi, *Anal. Sci.*, **4**, 353, (1988).

- 19 P. Savarino, G. Viscardi, E. Barni, R. Carpignano and L.A. Fedorov, *Dyes and Pigments*, **13**, 71-80, (1990).
- 20 L.A Fedorov, S.A. Sokolovskii, S.I. Dvoskin and V.M. Chertov, *J. Org. Chem. USSR.*, **23**, 2067, (1987).
- 21 A.M. Chippendale, *Private Communication*.
- 22 A.R. Monahan and D.F. Blossey, *J.Phys. Chem.*, **74**, 4014, (1970).
- 23 A.R. Monahan, N.J. Germano and D.F. Blossey, *J.Phys. Chem.*, **75**, 1227, (1971).
- 24 J.E. Kuder, *Tetrahedron*, **26**, 1973-1981, (1972).
- 25 V. Bekarek, K. Rothschein, P. Vatesnik and M. Vecerea, *Tetrahedron Letters.*, 3771, (1968).
- 26 G. Gabor, Y. Frei, D. Gegiou, M. Kaganowitch and E. Fischer, *Israel J. Chem.*, **5**, 193, (1967).
- 27 J. Ospenson, *Acta Chem. Scand.*, **5**, 491, (1951).
- 28 D. Hadzi, *J. Chem. Soc.*, 2143, (1956).
- 29 A.W. Hanson, *Acta. Cryst.*, **B29**, 454, (1973).
- 30 N. Ehlinger and M. Perrin, *Acta Cryst. C*, **51**, 1846, (1995).
- 31 Y. Saito, B. Kim, K. Machida and T. Uno, *Bull. Chem. Soc. Jpn.*, **44**, 2111, (1974).
- 32 S. Chattopadhyay, G.S. Kastha and S.K. Brama, S. Chattopadhyay, G.S. Kastha and S.K. Brama, *J. Raman Spectrosc.*, **22**, 449, (1991).
- 33 P.K Bajpai, B. Pal and T.S. Basu Baul, *J. Raman Spectrosc.*, **26**, 217, (1995).
- 34 P. Gregory and D. Thorp, *J. Chem. Soc. Perkin Trans. I*, 1990, (1979).
- 35 R. Challoner and R. K. Harris, *Solid State NMR*, **4**, 65, (1995).

- 36 D.A. Osokin, I.A. Saphin, B.I. Buzoikin and P. Kitaev, *Dokl. Akad. Nauk. USSR.*, **223**, 920, (1975).
- 37 C. J. Brown, *Acta Crystallogr.*, **21**, 146, (1966).
- 38 J.A. Bouwstra, A. Schouten and J. Kroon, *Acta Crystallogr.*, **C39**, 1121, (1983).
- 39 A.C. Olivieri, R.B. Wilson, C. Paul and D.V. Curtin, *J. Am. Chem. Soc.*, **111**, 5525, (1989).
- 40 R.G. Cooke, C.L. Raston and A.H. White, *Aust. J. Chem.*, **33**, 441, (1980).
- 41 S.H. Alarcón, A.C. Olivieri and P. Jonsen, *J. Chem. Soc. Perkin Trans II*, 1783, (1993).
- 42 M.L. Garcia, J.A.S. Smith, P.M.G. Bavin, C.R. Genelin, *J. Chem. Soc. Perkin II*, 1391, (1983).
- 43 T. Eguchi, M. Kishita, N. Nakamura and H. Chihara, *J. Phys. Soc. Jpn.*, **57**, 227, (1988).
- 44 K.-Y. Law, S. Kaplan, R. Crandall and I. W. Tarnawski, *Chem. Mater.*, **5**, 557-565, (1993).

6. Analysis of Dipolar Coupled Spin Systems Using N-15 NMR.

6.1 Introduction.

Nitrogen NMR spectroscopy affords a variety of information, due to its magnetic and electronic properties, and has been studied extensively by a range of NMR techniques. Nitrogen forms bonds with all non-inert elements, leading to an unusual variety of bond types, which generates a great variety of electronic environments and consequently a chemical shift range of over 1500 ppm for diamagnetic compounds. This is a result of nitrogen's greater electronegativity in comparison to ^{13}C , and its ability to carry lone-pair electrons with s character. Many texts exist reviewing nitrogen spectroscopy of both ^{14}N and ^{15}N nuclei,¹⁻⁵ with the majority of work being carried out on biologically important molecules, and focusing recently on the spin-1/2 ^{15}N nucleus (typically upon enriched samples). Table 1 shows the NMR properties of the two active nitrogen nuclei.

Nitrogen-14 is quadrupolar, $I=1$, and the rapid quadrupolar relaxation causes significant linebroadening of the spectrum. In the solid state it is generally not feasible to obtain ^{14}N spectra by standard CP/ MAS techniques. Double-quantum techniques have been developed which remove the effect of the first-order quadrupolar interaction.^{6,7} However, these techniques are only useful for nuclear species in highly symmetric environments where there is no second-order quadrupolar interaction.

	¹⁴ N	¹⁵ N
Spin I	1	0.5
Natural abundance (%)	99.635	0.365
Magnetic moment μ (μ _N)	0.57099	-0.4903
Magnetogyric ratio (10 ⁷ rad T ⁻¹ s ⁻¹)	1.9338	-2.712
Receptivity relative to that of ¹³ C	5.69	2.19 x 10 ⁻²
Nuclear quadrupole moment (10 ⁻²⁸ m ²)	1.99 x 10 ⁻²	0
NMR frequency Ξ (MHz)	7.26329	10.136783

Table 1
NMR properties of the ¹⁴N and ¹⁵N nuclei.⁸

6.2 Shielding Theory:- Special Emphasis on Nitrogen.

The shielding range for nitrogen is over three times greater than that for carbon, but similar trends in shielding constants are observed. The shielding contribution $\sigma_{\alpha\beta}$, can be decomposed into two terms according to whether the shielding opposes ($\sigma_{\alpha\beta}^d$) or assists ($\sigma_{\alpha\beta}^p$) the static magnetic field. The diamagnetic term does not vary greatly for a particular nuclear species, and is given by equation (1).

$$\sigma_{\alpha\beta}^d = \frac{\mu_o}{4\pi} \cdot \frac{e^2}{2m_e^2} \left\langle \Psi_0 \left| \left[\mathbf{r}_k \cdot \mathbf{r}_{Nk} \mathbf{1} - (\mathbf{r}_k)_\alpha (\mathbf{r}_k)_\beta \right] r_{Nk}^{-3} \right| \Psi_0 \right\rangle \quad (1)$$

However, the paramagnetic term which dominates the nitrogen shielding can vary significantly and is given by equation (2),

$$\sigma_{\alpha\beta}^p = -\frac{\mu_o}{4\pi} \cdot \frac{e^2}{2m_e^2} \sum_{n \neq 0} \frac{1}{(E_n - E_0)} \left\langle \Psi_0 \left| (\mathbf{L}_k)_\alpha \right| \Psi_n \right\rangle \left\langle \Psi_n \left| (\mathbf{L}_{Nk})_\beta r_{Nk}^{-3} \right| \Psi_0 \right\rangle \quad (2)$$

where the shielding tensor σ is defined by

$$\sigma_{\alpha\beta} = \frac{\partial^2 E}{\partial \mu_\alpha \partial B_\beta} = \sigma_{\alpha\beta}^d + \sigma_{\alpha\beta}^p$$

and where, r_{Nk} is the position of electron k relative to nucleus N , L_{Nk} is the angular momentum operator of electron k as determined relative to nucleus N , L_k is the angular momentum operator relative to a chosen gauge origin, and Ψ_0 and Ψ_n are the ground-state and excited-state electronic wavefunctions. Equations (1) and (2) are the single-electron shielding equations defined by Ramsey,⁹ and should be summed over all the electrons in the molecule.

The diamagnetic term results from the circulation of the electrons within closed, low-lying, shells resulting in a relatively constant screening of the nucleus, and this term will not be considered any further. The paramagnetic shielding term arises from the mixing of certain excited states with the ground electronic state in the presence of a magnetic field. Because of the nature of the projection operators in equation (2), the only excited states which can contribute to the paramagnetic term are those which are connected to the ground state by magnetic-dipole-allowed transitions. This paramagnetic shielding, which reinforces the static field, causes a deshielding of the nucleus, and is only present for non-spherical electronic distributions surrounding the relative nucleus. The shielding varies significantly for nitrogen nuclei due to the asymmetry of the p orbitals, which is dominated by the bonding and non-bonding, electrons. The $(E_n - E_0)$ term is an effective excitation energy for the paramagnetic circulation, and higher excited states obviously contribute less to the deshielding of the nucleus than low-lying states. These excitation energies vary more widely for nitrogen than for carbon, which is the

primary reason why nitrogen shielding constants exhibit a greater variety. The effects of the energy term are observed as δ/λ correlations, *i.e.* there is a direct relation between the nitrogen shift and the wavelength of the electronic transitions observed in visible spectroscopy within a series.⁵ This is particularly relevant in the present analysis of coloured azobenzene dyes.¹⁰ The weakly allowed $n_{\text{N}} \rightarrow \pi^*$ excitations, in which there is a component of the $s \rightarrow p$ type, gives the well-known long-wavelength bands of the azo chromophore, and causes a high-frequency shift of the nitrogen resonance. In nitrogen atoms which possess both π -bonding orbitals and lone-pair electrons, the energy difference between the ground and excited states is significantly reduced in comparison to singly-bonded, symmetric molecules, resulting in far larger paramagnetic contributions to the observed shifts. It is only possible to use these hand-waving arguments to discuss the actual frequency of the isotropic shift. To try to estimate the frequencies of the individual tensor components one must actually evaluate the wavefunction for the molecule. For symmetric molecules it is possible to utilise the symmetry to simplify the system and separate out the individual components at which point it may be possible to make comparisons in relation to the geometrical features. For planar systems, such as condensed aromatic hydrocarbons,¹¹ it is well established that the σ_{33} component of the ^{13}C shielding tensor is dominated by the σ -electron system. Hence, for azobenzenes the most shielded component for the ^{15}N azo nitrogen, which is known to be perpendicular to the plane of the azo group, mixes σ and σ^* orbitals (large energy-separation) resulting in small amount paramagnetic shielding, *ie.* a low frequency signal.

Consequently, the other two components observed for polycrystalline samples, reflect the π -delocalisation of the system centred around the azo group. The strongest deshielding (largest paramagnetic shielding) is observed for axes (σ_{11}) which mix n_N and π^* orbitals with a small ΔE . The energy of the $n_N \rightarrow \pi^*$ transition tends to increase upon decreasing the electronegativity of the partner in the double bond, within a homologous series, correspondingly lowering the ^{15}N resonance frequency in comparison to similar ^{13}C NMR. The σ_{22} axis points along the lone-pair orbital in these systems. These considerations assume that the azobenzene fragment is wholly planar, but this will not generally be the case, with the aromatic rings often rotating out of the plane. This rotation will effect the π^* energy by reducing the conjugation through the system, thus raising its energy. Additionally, it renders the $n_N \rightarrow \pi^*$ transition allowable. This approach is very simplistic, and will generally only give information regarding trends in a series of similar molecules.

A significant selection of literature has now been built up on nitrogen shifts, with the shifts for ^{14}N and ^{15}N being used interchangeably. An exact understanding of these shifts in relation to the previous discussion surrounding the paramagnetic shifts is not generally simple. Computation of ^{15}N shielding tensors via theoretical calculation methods has been applied with varying success. Generally, experimental agreement is good for singly-bonded molecules with high electronic excitation energies.³ However, in systems with multiple bonds and lone pairs, a poor correlation is observed due to the extensive mixing of several excited states, requiring accurate calculation of the electronic wavefunctions. Additionally, one tends to consider the molecular structure of an isolated molecule, which can lead to

large errors for nitrogen nuclei, where inter-molecular hydrogen bonding is known to be the principal governing factor in the tertiary structure of biomolecules. Therefore these interaction should be taken into account when looking at the tensors. Webb and co-workers¹² have looked extensively into how the interaction of solvents effects the shielding constants, whilst Facelli and co-workers have analysed the hydrogen bonding affects on benzamide,¹³ and uracil¹⁴ in the crystal state. The solid-state calculations show quite significant variations from the experimental values if hydrogen-bonding is ignored. A selection of experimental shielding tensors for the ¹⁵N nucleus are shown in Table 2.

Compound	δ_{iso}	σ_{iso}	σ_{11}	σ_{22}	σ_{33}	Ω	κ	Ref.
NH ₃ (g)	-400	254	238	278	278	40	1	Kukolich ¹⁵
P≡N (g)	213	-349	-689	-689	350	1048	-1	Raymonda ¹⁶
<i>trans</i> -PhN=NPh	131	-267	-789	-146	136	925	0.39	Wasylishen ¹⁷
C ₆ H ₄ ¹⁵ NO ₂	-2	-134	-399	-32	30	429	0.71	Freidrich ¹⁸
NH ₄ ¹⁵ NO ₃	-4	-132	-220	-189	11	321	-0.74	Delmotte ¹⁹
Pyridine- ¹⁵ N	-83	-53	-387	-168	395	782	-0.44	Spiess ²⁰
Nylon-6	-268	132	34	154	29	275	0.37	Powell ²¹
-(CO ¹⁵ NH)-								
O ₂ N(C ₆ H ₄)C≡ ¹⁵ N	-117	-19	-153	-143	240	393	-0.95	Sardashti ²²

Table 2

Principal components of nitrogen shielding tensors for a range of systems. Shifts (δ) and shielding (σ) are related according to $\sigma = -135.8 - \delta(\text{MeNO}_2)$. Ω and κ are defined on page 122.

6.3 ^{15}N Tensor Analysis of Azo and Imine Groups.

The low receptivity of ^{15}N at natural abundance negates the possibility of acquiring most shielding tensors from natural-abundance ^{15}N solid-state NMR, particularly by static techniques. In the future, the application of the dynamic nuclear polarisation technique²³ will allow tensors to be evaluated at natural abundance in a whole range of samples, and also the detection of signals from very dilute spin systems. This would be important in biomedical applications where one wishes to look at biopeptides in situ, and also for the observation of the ^{15}N signal from dyes located within dye fibres. At the moment, the majority of tensor analyses are carried out on ^{15}N -enriched, polycrystalline samples, via static bandshape,²⁴ and spinning sideband analyses (SSB).²⁵

The only ^{15}N tensor analyses that have been carried out on azobenzenes, or hydrazones, were those reported by Wasylishen and co-workers on both *trans*- and *cis*-phenylazo-benzene.^{17, 26} Wasylishen's study of *trans*-azobenzene was applied to a doubly-labelled sample, which consequently resulted in the creation of a ^{15}N - ^{15}N isolated spin-pair. This is a highly advantageous situation because application of a tensor analysis upon isolated spins, with no other interactions, does not allow one to orient the shielding tensor relative to the molecular frame. In the above analysis, it was possible to orient the shielding tensor relative to the N=N bonding vector. Simulations of static lineshapes from dipolar-coupled spin-pairs have been carried out regularly, and complex fitting routines generally fit the first, or second, derivative spectra, as these are more sensitive to the presence of dipolar coupling.²⁷⁻

³⁰ Theory suggests that the most shielded component, σ_{33} , points perpendicular to

the C-N=N-C plane ($\beta^{\text{CS}} = 90^\circ$), and this is what was observed from the results of the static spectrum where β^{CS} was found to be $\sim 80^\circ$. The deviation from 90° for the σ_{33} component is probably a result of the non-planarity of the aromatic rings. Additionally, the σ_{22} component was thought to point along the nitrogen lone pair orbital corresponding to a $\alpha^{\text{CS}} = \sim 30^\circ$ (assuming a 120° N=N-C dihedral angle), and an experimental value of $\sim 40^\circ$ was found. Throughout this chapter the convention used is that of Mason³¹ whereby the principal components of the shift tensor are defined according to $\delta_{11} \geq \delta_{22} \geq \delta_{33}$, and the following properties are useful in understanding the symmetry of the electronic environment:

$$\text{Span; } \quad \Omega = \delta_{11} - \delta_{33}, \quad \text{Skew; } \quad \kappa = \frac{3(\delta_{22} - \delta_{\text{iso}})}{(\delta_{11} - \delta_{33})}$$

In the present analysis, the samples described in the previous three chapters have been treated via both static bandshape analysis, using a fitting routine based on the POWDER interpolation scheme,²⁴ and SSB analysis, using a program developed at Durham.³² As in Wasylishen's analysis, it is impossible to directly obtain the principal components of the shift tensor for these nitrogen environments without consideration of direct dipolar interactions, either heteronuclear (^{14}N - ^{15}N), or homonuclear (^{15}N - ^{15}N). Examples of both systems can be prepared by specific isotopic enrichment. The initial results are presented as obtained from singly-labelled samples, either at the α or β positions, along with one example of a ^{15}N - ^{15}N isolated spin pair, *i.e.* doubly-labelled at the α , β positions.

6.3.1 DR278 Polymorph II: α (II α), β (II β) and α , β (II d) ^{15}N -labelled samples.

A static analysis of these singly-labelled samples proved to be impossible at 20 MHz due to the fact that the two overlapping powder patterns, arising from the conformations previously discussed, could not be resolved. Increasing the static field strength to 40 MHz provided a significant improvement in the resolution, presumably due to the fact that the chemical shift is scaled in frequency while the dipolar coupling is invariant to field strength; therefore the coupling will contribute less at the higher field. At 40 MHz two δ_{22} components could be observed for each of the singly-labelled samples, which is rather surprising if one considers that there is a dipolar coupling of ~ 600 Hz present. This suggests that the orientation of the dipolar vector, in the principal axis system of the shift tensor, is such that no splitting is observed for the δ_{22} component. The two δ_{11} components could be seen for II α , while the δ_{33} components were resolved for II β , with the third pair for each sample not being observed, as shown in Figure 1, due to the quadupolar coupling which broadens the turning points. The spectrum of II d , which is a doubly-labelled sample, is also shown for comparison. To show these effects, a simulation of the best estimate for II α , in which $\alpha^{\text{D}} = 35^\circ$ and $\beta^{\text{D}} = 90^\circ$, is compared to that of an arbitrary orientation of the dipolar vector in Figure 2. The accuracy of β^{D} is rather low and the splittings obtained are actually dependent upon both the α^{D} and β^{D} values. Correspondingly, if β^{D} is chosen to be 80° then the value for α^{D} would increase to 36° to maintain the structure of the δ_{22} components.

In fitting these static powder patterns to obtain the shift tensor values the dipolar coupling was ignored to simplify the situation. This is a valid simplification when one looks at the actual powder patterns, and also when comparing the SSB results to the static values. A simulation of the static powder pattern for $\text{II}d_1$, Figure 3, shows the effect of ignoring the dipolar coupling. A satisfactory fit could not be obtained if all three principal components were allowed to be variables in the fitting process, and so δ_{iso} and δ_{22} were fixed. The results of the fitting routine are shown in Table 3, along with the results obtained from the SSB analysis at various spin rates. It should be noted that heteronuclear dipolar coupling is an inhomogeneous interaction, which for weak couplings, is spun out at slow spin rates, and therefore, the resultant spectral intensities arise purely from shielding anisotropy. This is not the case for the homonuclear interaction as will be discussed later. The errors in the results obtained from the fitting routines can generally be considered to be ~ 5 ppm for each program, but arise from different origins. The digital resolution of the static spectra is ~ 100 Hz (3 ppm) and the consequent goodness of fit can be no better than the resolution of the original data. In the SSB case the surface over which one fits is relatively flat, and even if a good correlation between experimental and simulation appeared to exist there may be a large range of possible solutions that lie close to the minimum. Figure 4 shows a representative ^{15}N CP/ MAS spectrum of DR278.

In comparing the four different signals some significant deviations can be observed. The signals for $\text{II}\beta$ produce similar spans of ~ 900 ppm, but the corresponding skews vary by 0.1, while the signals for $\text{II}\alpha$ show the same skews, but

have different spans. The spectrum for $\text{II}d$ (Figure 1b) appears to be purely a superposition of the two singly-labelled spectra, again indicating that the orientation of the dipolar vector in the principal axis system of the shift tensor is such that the splittings are minimised.

If one tries to analyse these values in relation to the previous discussion relating to electronic transitions some curious features are revealed. $\text{II}\alpha$ is the ^{15}N nucleus which undergoes hydrogen bonding, and therefore, the non-bonding orbital on the azo-nitrogen, n_{N} , would be expected to change its energy rather significantly. Additionally, the lone-pair electrons of the amide also act to stabilise the aromatic ring, raising the π^* energy level. As a result, the two separate interactions cooperate to change the energy of the $n_{\text{N}} \rightarrow \pi^*$ transition, but this change does not manifest itself upon the σ_{11} component as the two values are very similar. A large paramagnetic shift is observed in going from $\text{II}\alpha$ to $\text{II}\beta$ for the σ_{11} components, which can be explained by a reduction of the same transition energy. However, the exact nature of the change of the energy levels cannot be precisely determined

Figure 1 a/ and d/ show very interesting features, which at first appearance seem rather beguiling, and uninterpretable in terms of the expected lineshapes arising from dipolar-coupled powdered samples. The apparent discrepancies in the intensities of the high-frequency region of the spectra are a result of the very high quality of the probe used for these measurements.

This is an unusual problem for a spin-1/2 nucleus, because typically the dominant criterion, which affects signal intensities, in the experimental setup is the strength of the X-channel rf field. This is due to the fact that a pulse of duration τ

excites over a bandwidth defined by the Fourier transform of a truncated cosine wave. The shape of this excitation profile, in the frequency domain, is represented by a sinc function, and the frequency at which a signal is attenuated by a factor of $1/2$ is at the -3 dB point, in comparison to the maximum of the sinc function (on resonance). This is simply four times the nutation frequency of the rf field, if a 90° tip angle is used in a Bloch-decay experiment. Application of CP to generate the X-channel signal however, removes this problem because the X channel is not used for an excitation pulse, but purely to give a matching field which satisfies the Hartmann-Hahn condition, and to produce sufficient spin-locking of the nuclear spins. Correspondingly, assuming one applies a strong enough rf field to the proton spin system to excite over the whole dipolar-coupled proton reservoir, then all X nuclear spins will be equally excited (with the obvious modification due to CP dynamics).

Linear response theory dictates that if a system is subjected to a stimulus the detected signal is a convolution of the input signal with the input response of the system. The response function will be exponential in nature, and subsequent Fourier transformation of this damped oscillation (probe acoustic ring-down) produces a Lorentzian line. The width, $\Delta\omega_{1/2}$, of this band determines the bandwidth of the probe, and hence the frequency range over which signals can be detected. This is not entirely true, because probes generally do not react in a perfectly linear manner to a pulse, and higher order effects need to be considered. However, this first-order approach was used to simulate the response function for the probe, when tuned to ^{15}N .

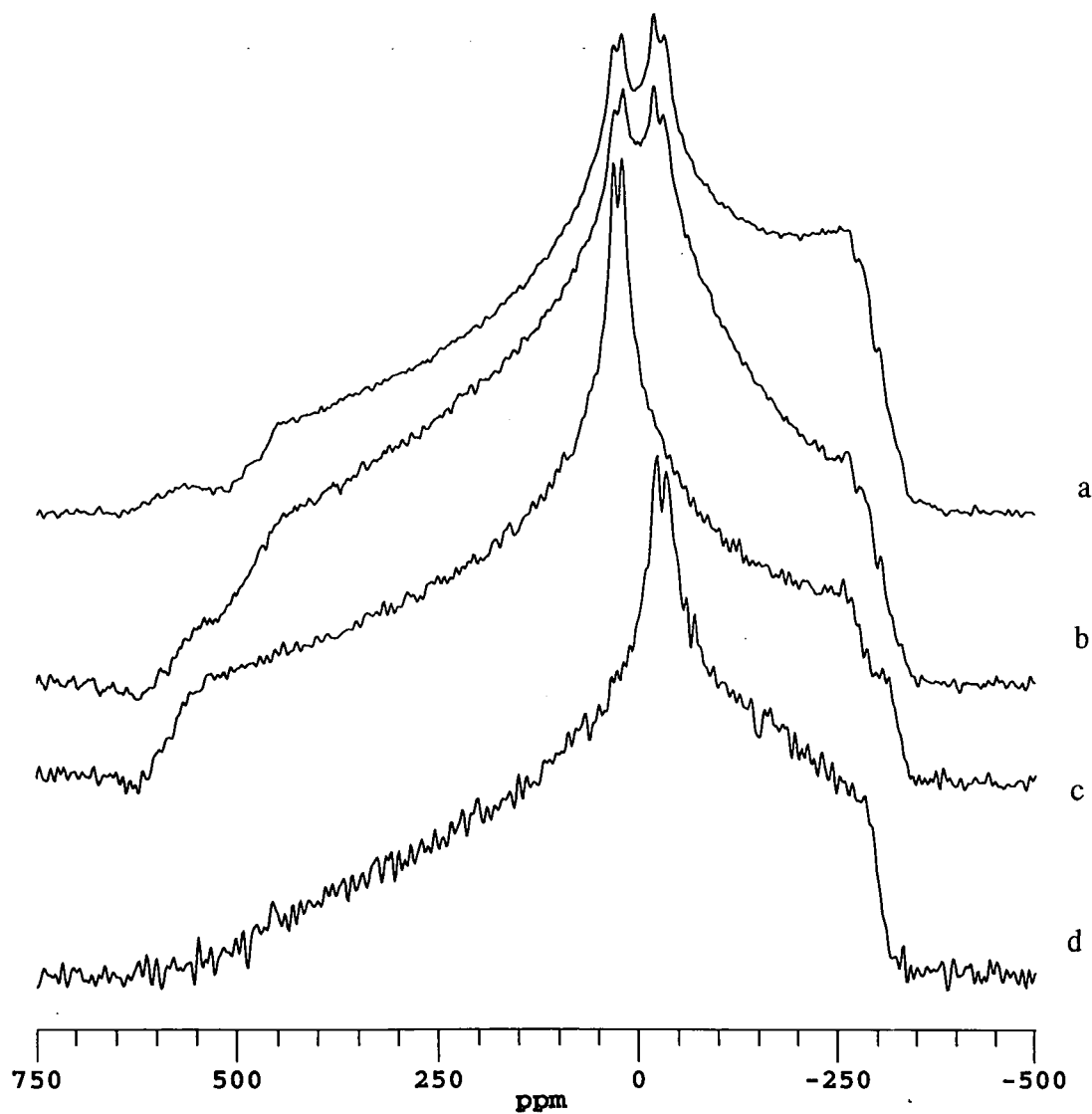


Figure 1

^{15}N static powder patterns for a/ IIdI at 40.57 MHz, b/ IIdI at 40.58 MHz c/ II β and d/ II α , at 40.57 MHz using a Hahn-echo pulse sequence.

Sample	Method	δ_{iso}	δ_{11}	δ_{22}	δ_{33}	Ω	κ
II α	Static	60	500	-23	-297	797	-0.31
	SSB 2kHz	60	505	-21	-304	809	-0.30
	Static	44	470	-34	-304	774	-0.30
	SSB 2 kHz	44	476	-36	-307	783	-0.31
II β	Static	89	577	22	-323	900	-0.22
	SSB 1 kHz	89	575	22	-328	903	-0.22
	SSB 4.2 kHz	89	579	16	-327	906	-0.24
	Static	121	614	32	-279	893	-0.30
	SSB 1 kHz	121	599	36	-272	871	-0.29
	SSB 4.2 kHz	121	613	31	-281	894	-0.30
	Static	131	653	10	-272	925	-0.39
AB	Static	131	653	10	-272	925	-0.39
Diazene	Calculated	379	1234	226	-322	1556	-0.29

Table 3

Principal components (in ppm) of the shift tensor for the two conformations present in II α and II β . The corresponding values for trans-azobenzene (AB) and the calculated shifts for diazene (N₂H₂) (from reference 17) are given for comparison.

Figure 5 shows a series of simulations for an arbitrary static powder pattern (similar to the azo ¹⁵N powder patterns), which has been convoluted with Lorentzian broadening functions of differing width, centred near the isotropic shift (a-c), and differing centre, but constant width (d-h). These simulations are rather dramatic, and reflect the need for careful experimental procedure when one wishes to obtain accurate tensor patterns from high Q-probes. The transmitter position can be

optimised such that it is placed near to the centre of the spinning sideband manifold, not the isotropic shift position.

However, the Q of the probe is inherent in the reactive components within it, and as such cannot be readily modified. The Q can be reduced by addition of resistive elements within the tuning circuit, but reduction should not be attempted by mis-matching the probe circuitry. This is a problem which will become more important in the future, with the need for multi-purpose probes at higher field strengths.

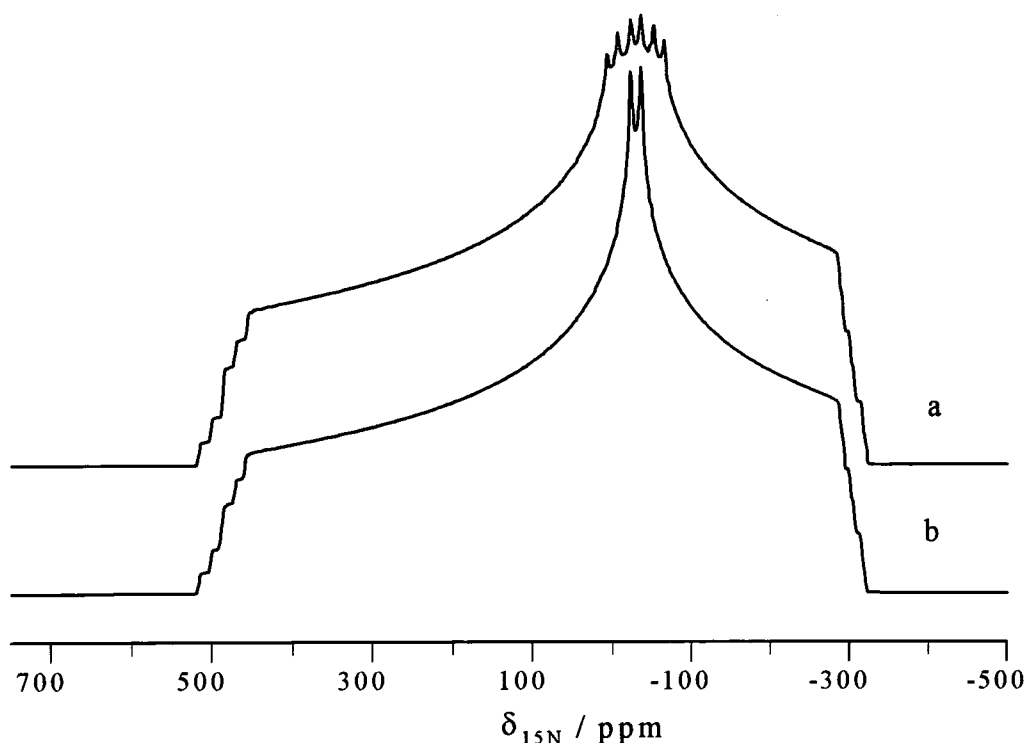


Figure 2

Simulation of the static ^{15}N spectrum of $\text{II}\alpha$, coupled to a single ^{14}N nucleus. The simulations were carried out at 40.6 MHz and correspond to two different orientations of the dipolar vector; a/ ($\alpha^D=90^\circ$, $\beta^D=90^\circ$) and b/ ($\alpha^D=35^\circ$, $\beta^D=90^\circ$), using the principal components obtained by averaging the entries in Table 3 for each resonance.

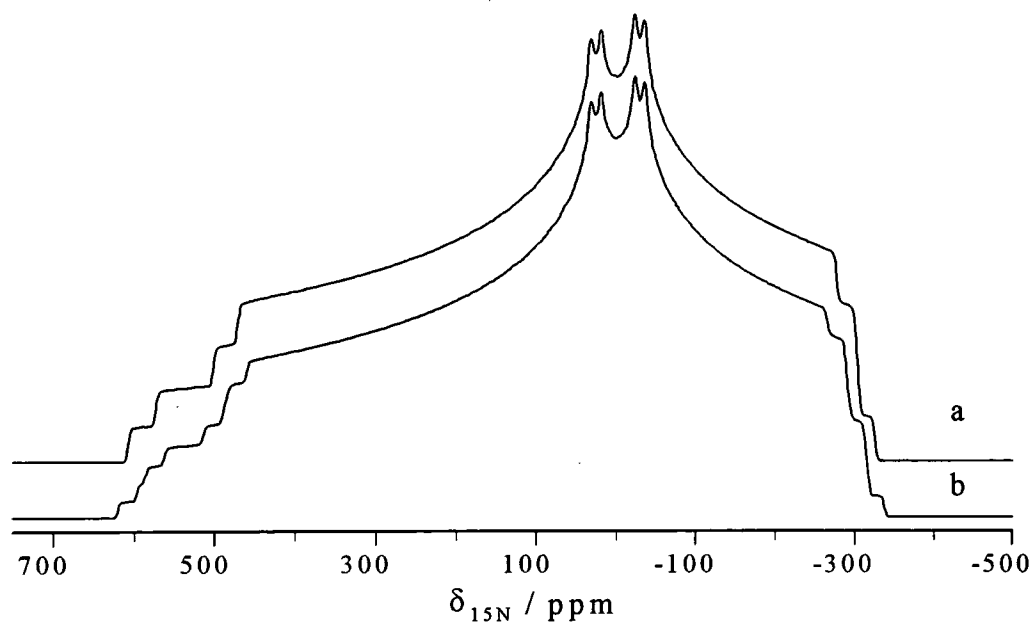


Figure 3

Simulations of DR278 II α , β double label at 40.6 MHz using the average of all the principal components from Table 3 for each resonance assuming; a/ no dipolar interaction, and b/ homonuclear dipolar coupling as discussed in text.

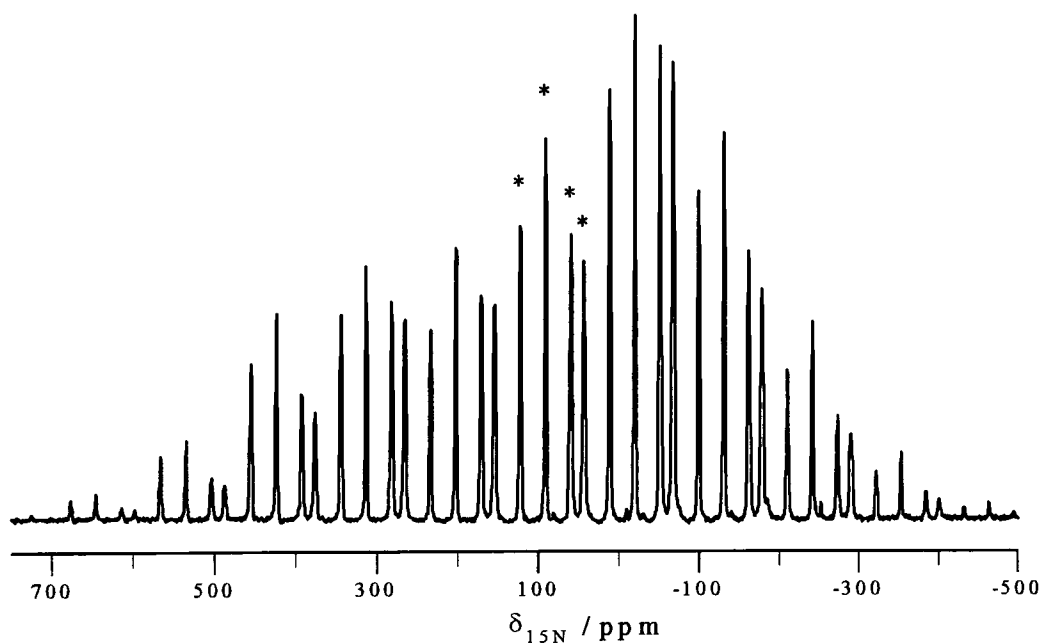


Figure 4

*^{15}N CP/MAS spectrum of IIdl obtained at 40.6 MHz, with a spin rate of 4.5 kHz. * denote the isotropic shifts.*

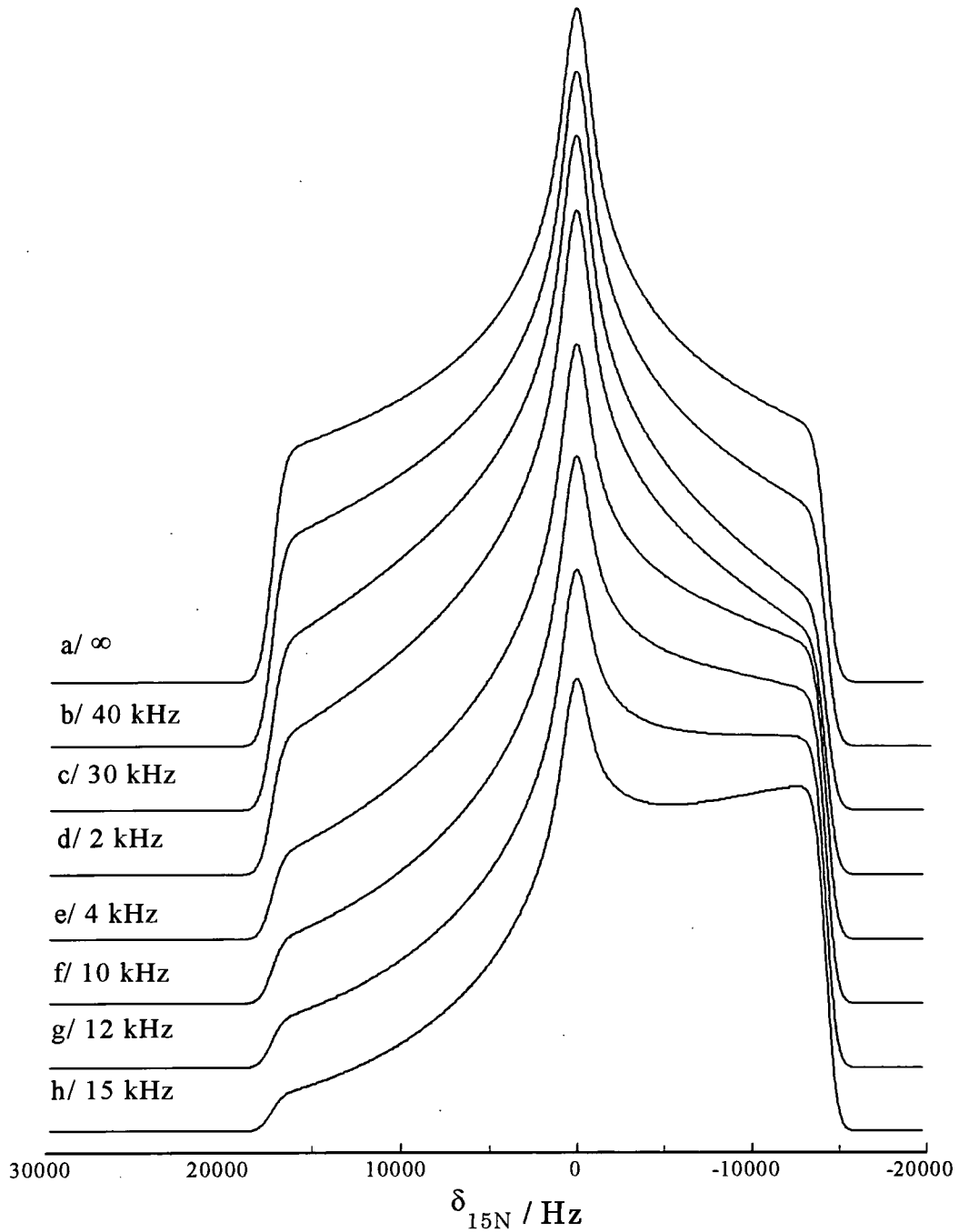


Figure 5

^{15}N static simulations with an additional Lorentzian broadening function simulating the effects of probe bandwidth; a/, b/ and c/ with centre at zero and varying broadening, and d/-h/ with a fixed broadening function of 30 kHz and varying centre.

6.3.2 DR278 Polymorph VI: β (VI β) labelled samples.

Consideration of the same principles as used in the analysis of the previous samples, produced a rather good fit, as can be seen from the data in Table 4. The MAS results are all consistent with each other within experimental error for each field strength used. There is an apparent increase in the span for the higher field SSB experiments, in relation to the results obtained at 20 MHz. However, this trend was not observed for the static spectrum, which showed a significant decrease in the span, which can possibly be accounted for by the aforementioned probe bandwidth problem.

Method	δ_{iso}	δ_{11}	δ_{22}	δ_{33}	Ω	κ
Static	106.9	613	27	-317	930	-0.26
	a					
SSB 2 kHz	a	625	25	-335	960	-0.26
SSB 3 kHz	a	627	27	-334	961	-0.25
SSB 2 kHz	b	621	27	-327	948	-0.25
SSB 3 kHz	b	619	27	-326	945	-0.25
SSB 4 kHz	b	620	31	-330	950	-0.24

Table 4

Principal components (in ppm) of the shift tensor for VI β obtained at

^a 40 MHz and ^b 20 MHz.

This sample is thought to exist in the non-hydrogen bonded conformation, and the results should therefore be very similar to those obtained for the 89 ppm peak in II β . Direct comparison of the principal components for each sample shows that δ_{33} and δ_{22} are very similar for the two cases, while the δ_{11} components are

significantly different. They are in fact ~50 ppm different, which wholly accounts for the difference in the isotropic shifts. Thus, the interaction which leads to this extra shielding for VI β must be a component of the paramagnetic shielding constant which affects the electron density perpendicular to the molecular frame. In the non-intra-molecular hydrogen-bonded conformation it is possible for the amide group to rotate freely if it is not involved in the formation of an inter-molecular hydrogen bond. The amide nitrogen's lone pair will form stronger π -orbital overlap if it is oriented co-linearly with the aromatic π -system, and when this occurs the π^* anti-bonding orbital will increase in energy. This would result in a reduction of the paramagnetic contribution to the δ_{33} shift component, which is observed for II β . Secondly, the planarity of the molecule will affect the observed shifts, from similar considerations as above, with non-planarity reducing the conjugation through the system. Additionally, a slight change in the π - π stacking separation could produce a similar effect, as just discussed. These are, however, only speculative proposals, because the crystal structures of these polymorphs are different. The origins of these changes cannot be explained without knowledge of the crystal structures.

6.3.3 Sulphonic acid azobenzene derivatives: β -labelled samples.

These sulphonates, from the ^{13}C and ^{15}N isotropic shifts, were found to be present in either the azo or hydrazo tautomers. From comparison with the principal components of the shift tensors for the previous samples, it is simple to determine which tautomer is present. The previous β -labelled samples show that there is a large variation of shifts for the three principal components, with the spans varying between 850 and 950 ppm, and the skews varying between 0.2 and 0.3. The hydrazo, $\text{N-}^{15}\text{N}=\text{C}$, ^{15}N shift tensor components have not been reported in the literature. The principal components, and their orientation in the molecule, for the ^{15}N shift tensor, were obtained by Curtis *et al.*, for the simple Schiff base, *trans*-benzylideneaniline.³³ This $\text{C}=\text{N}$ moiety will possibly allow the orientation of the imine shift in the hydrazo form to be determined, and it will serve as a comparison for the relative magnitudes of the shifts.

In the previous chapter the solid UV/ Vis spectra for IIa and III were presented to try to understand the structures of the relevant molecules. It should be noted that the spectral transitions have $\pi \rightarrow \pi^*$ character, and therefore do not relate in any way to the discussion regarding chemical shift relationships to electronic spectra.

Table 5 shows the principal components of the ^{15}N shift tensor for the acids and salts of the substituted *p*-hydroxyazobenzene sulphonates, and an example of the fitting accuracy of the SSB method is given in Figure 6. The SSB spectra shown are purely Lorentzian convolutions, with an arbitrary linewidth, of the normalised input and output intensities for the SSB fitting routine.

Sample	Method	δ_{iso}	δ_{11}	δ_{22}	δ_{33}	Ω	κ
Salts (Na)							
IIb/ p-OH	SSB 2.5 kHz	130.0	659	11	-279	938	-0.38
IV/ p-OH, o-CH ₃	SSB 2 kHz	128.0	670	5	-290	960	-0.38
	SSB 4 kHz		679	0	-294	973	-0.39
VI/ o, p-diOH	SSB 2 kHz	107.0	576	24	-282	858	-0.29
	SSB 4.1 kHz		586	14	-282	868	-0.32
Acids							
III/ p-OH	Static (fit)	40.9	437	21	-321	763	-0.08
	SSB 3.5 kHz		434	20	-330	764	-0.08
	SSB 5 kHz		425	19	-320	745	-0.09
V/ p-OH, o-CH ₃	Static (fit)	31.2	396	15	-319	715	-0.07
	SSB 3.5 kHz		423	14	-343	766	-0.07
	SSB 5 kHz		425	16	-347	772	-0.06
VII/ o, p-diOH	Static (fit)	5.8	338	5	-314	652	0.00
	SSB 4 kHz		368	8	-359	727	0.01
	SSB 5.5 kHz		373	3	-359	732	-0.01
Benzylideneaniline a	Static	-48	229	-60	-316	545	0.06

Table 5

Principal components (in ppm) of the shift tensor for the sulphonated phenylazobenzene dyes. (a From Ref 33)

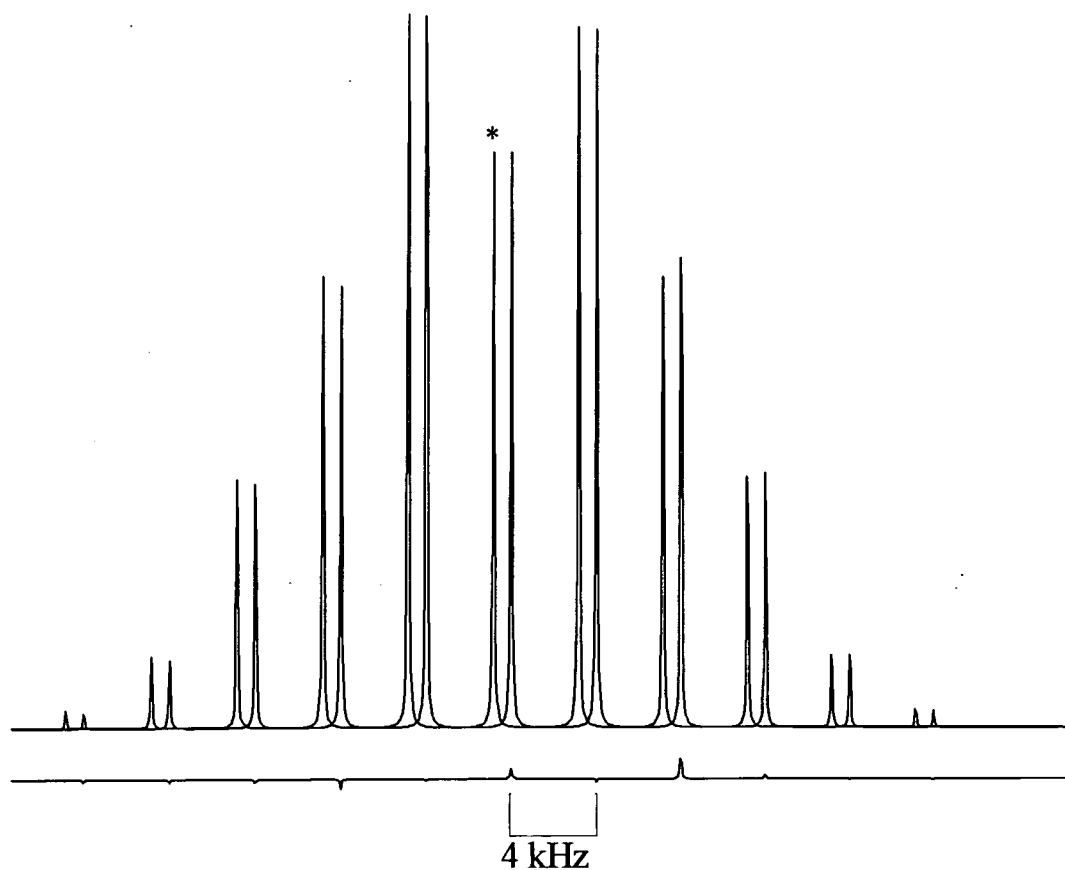


Figure 6

*Comparison of the experimental and the best-fit spinning sideband manifold for VII spinning at 4 kHz. The best-fit tensor components are given in Table 5. The difference spectrum is shown with an error, represented as a sum square difference, of 0.5. The total signal intensity was normalised to 100. The isotropic shift is indicated by * above the isotropic shift for the experimental spectrum..*

Prior to trying to understand the shift tensor components in relation to the structures, care should be taken with regard to which data one should use for the acid samples. It can be seen that for V and VII there is a large difference between the static and SSB outermost tensor components. It can be shown, by application of a moments analysis, that the symmetric distortion of the powder pattern due to the narrow bandwidth of the probe reduces the span of the calculated powder pattern. If one considers a probe bandwidth of ~ 30 kHz, then δ_{11} and δ_{33} will be reduced by ~ 50 ppm, which is in line with the observed differences between the static and SSB values. This same narrowing of the powder pattern (15-20 ppm) was also observed for VI β . It is rather unclear how the distortion affects the fitted values when using the POWDER algorithm,²⁴ because comparison of the best fit with the actual experimental bandshape seems to indicate that the fitting compensates for the intensity distortions. The SSB fitting routine is known to be less sensitive to these distortions. The outermost sidebands which will be affected are generally weak, and therefore contribute less to the least-squares parameter which the simplex algorithm wishes to minimise. This was verified by restricting the range over which the program reads the signal intensities for its optimisation, and virtually no change in the output values was detected. Thus, it would seem valid to assume that the static tensors are incorrect, and that the SSB values should be used for these samples.

A direct comparison of the results for the salts and the acids shows that δ_{22} is virtually independent of the nature of the nitrogen environment, but large changes are readily observed for δ_{11} and δ_{33} . The δ_{33} component changes by ~ 50 ppm, which is marginal for nitrogen shifts. The dominant change is that of the δ_{11} component,

which reduces by ~ 200 ppm in going from the salt to the acid. This low-frequency shift creates a highly asymmetric powder pattern, with a skew of ~ 0 , *i.e.* the powder pattern is centrosymmetric, which is very similar to the case of benzylideneaniline. The 200 ppm lower shift for the acid is dominated by the electronegativity of the atom involved in the double-bond formation, as previously mentioned. The reduced electronegativity of the carbon atom, in relation to nitrogen, increases the π^* energy relative to that of the n orbital, reducing the paramagnetic shielding of the σ_{11} component. This result is concurrent with the results obtained by Curtis³³ and Wasylishen,¹⁷ and also with azobenzene and several other molecular groups³⁴.

In looking at these principal components the orientation of the tensor must be evaluated for the acid systems, since it will not be the same as for the azobenzene cases. In the static spectra no splittings were observed for the δ_{22} components, which indicates that this component is again oriented along the nitrogen lone pair. Similarly, the δ_{33} component is likely to remain approximately perpendicular to the plane of the molecule. The δ_{11} component does not necessarily need to be oriented in the same direction, and will probably point in the opposite direction, *i.e.* $\alpha^D = 145^\circ$. One cannot distinguish between the two possible orientations from the static powder pattern, due to the symmetric nature of the splitting of the δ_{22} component (even symmetry around $\alpha^D = 90^\circ$). However, from the benzylideneaniline case, where $\alpha^D = 42^\circ$, it is clear that the angle is $\sim 140^\circ$ in the present hydrazo molecules. The angle α^D in benzylideneaniline is with respect to the C=N vector, not the N-N dipolar vector as in our case.

6.4 Reintroduction of Dipolar Interactions Under MAS Conditions.

The magic-angle spinning spectra in the previous sections have all been fitted by assuming that the dipolar interaction does not contribute to the sideband intensities. This is a valid assumption due to the fact that all the spin rates exceeded the strength of the dipolar coupling.³⁵ Over the past decade it has proven popular to try to reintroduce the dipolar interaction by mechanical manipulation, or by the application of complex pulse sequences. This development was initiated as a result of the fact that static lineshapes only yield accurate information for small dipolar coupled spin systems. In complex spin systems with multiple couplings it is impossible to disentangle the dipolar couplings from each other, and also from the shielding components. Excellent review articles by Griffin and co-workers^{36, 37} summarise the manner in which these interactions can be reintroduced and how they manifest themselves as complex spectral features in an NMR spectrum, in either one or two dimensions. Additionally, if one can accurately predict multiple dipolar couplings within MAS spectra then it may be possible to carry out experiments which map out the whole dipolar coupling network within a molecule, and therefore determine the structure, in a similar fashion to the NOESY³⁸ experiments in solution state NMR.

To determine weak homonuclear coupling constants under MAS several experiments can be applied, depending upon the nature of the system, and they can be categorised into two groups. The first class involves the periodic application of rf pulses which interfere with the spatial averaging effects of MAS, and therefore restore homonuclear and heteronuclear dipolar couplings to the spectrum. In these

experiments the dipolar coupling prevents the complete refocusing of the rotor echoes, and an oscillatory dephasing of the magnetisation is observed, with the resultant curves being well understood.³⁹ The second class involves a rotor-driven exchange of magnetisation, which occurs when the MAS rate satisfies the condition of rotational resonance, i.e. $n\omega_R = \Delta\omega_{iso}$.

6.4.1 Rotational Resonance: R^2

The theory of rotational resonance has been explained in detail elsewhere by Levitt,⁴⁰ Vega⁴¹ and McDowell.⁴² To determine accurate results one must apply Floquet theory and carry out some rather complex matrix calculations. In the present analysis only a phenomenological discussion of the rotational resonance experiment will be described, because the Floquet method has not been used and accurate lineshape calculations were not carried out.

The Hamiltonian for two homonuclear dipole-coupled, chemically-shifted spins I and S is given by:

$$H(t) = \omega_I(t)I_Z + \omega_S(t)S_Z + \omega_A(t)2I_ZS_Z + \omega_B(t)\frac{1}{2}(I_+S_- + I_-S_+)$$

where the first two terms are the individual Zeeman terms which are proportional to the resonance frequencies, $\omega_I(t)$ and $\omega_S(t)$, and the dipolar prefactors $\omega_A(t)$ and $\omega_B(t)$ can be expressed in terms of the dipolar Fourier components. The flip-flop term renders the dipolar interaction homogeneous and spin rates substantially greater than the dipolar interaction are required to average the interaction to zero. For weak couplings this is often the case, and contributions from the flip-flop term can be

ignored because it is not energy conserving. Hence, the dipolar interaction reduces to that of the heteronuclear case which involves only the bilinear term. However, when a multiple of the spin rate equals the frequency difference between the two isotropic shifts, *i.e.* $n\omega_R = \Delta\omega_{iso}$, for the spins under consideration, then the energy mismatch for the flip-flop component is compensated for by an effective absorption of a quantum of energy from the spinning perturbation. This reintroduces the homogeneous nature of the dipolar Hamiltonian and a powder pattern is observed for the isotropic shifts (and corresponding sidebands). The magnitude of the powder pattern is dependent upon the Fourier component $\omega_B(t)$, which under rotational resonance drives the transfer of coherence between the two states connected by the flip-flop component of the dipolar Hamiltonian. This component can be obtained by comparison of the equation for a time-dependant dipolar interaction determined by Munowitz and Griffin.³⁵

$$\omega_B(t) = \omega^D \left(G_1 \cos(\omega_R t + \phi_{ij}) + G_2 \cos(2\omega_R t + 2\phi_{ij}) \right)$$

$$G_1 = \frac{3}{4} \sin 2\theta_m \sin 2\phi_{ij}$$

where:

$$G_2 = -\frac{3}{4} \sin^2 \theta_m \sin^2 \phi_{ij}$$

θ_m is the angle of the rotor axis with respect to the magnetic field and ϕ_{ij} is the angle which the dipole axis makes with the rotor axis.

G_1 and G_2 are relevant for the cases for $n=1$ and $n=2$ rotational resonance respectively. Hence, for $n=1$ rotational resonance the maximum dipolar splitting possible is (assuming that θ_m is the magic-angle):

$$S_{MAX} = 2\pi D' G_1 = \left(1/\sqrt{2}\right) 2\pi D'$$

Challoner⁴³ derived this maximum splitting and it was observed in his analysis of a linear diazomium cation. Using the same assumptions for DR278, which are not perfectly valid, gives an upper estimate of the coupling constant, and thus the lower N=N bond length. The ¹⁵N spectrum for polymorph A of doubly-labelled DR278 exhibits a splitting at the n=1 rotational resonance condition for the 121 ppm and 44 ppm resonances, corresponding to a spin rate of 2330 Hz as shown in Figure 7. An experimental splitting of ~200 Hz was observed by averaging the splittings from several sidebands in the ¹⁵N R² spectrum. Hence, the effective dipolar coupling constant D' was found to be 566 Hz corresponding to a bond length of 1.3 Å which is in line with the results obtained from the single crystal X-ray study (1.25 Å). This value should be considered speculative at best, but a full lineshape calculation is underway and will produce reasonably accurate results. However, the accuracy will not be as high as in the paper by Challoner⁴³ due to the poor spectral resolution so other techniques may have to be attempted. The presence of molecular exchange will also complicate the issue quite considerably and conversion to polymorph C would produce significantly better results, due to the absence of molecular motion and also the reduced linewidth of the ¹⁵N resonances.

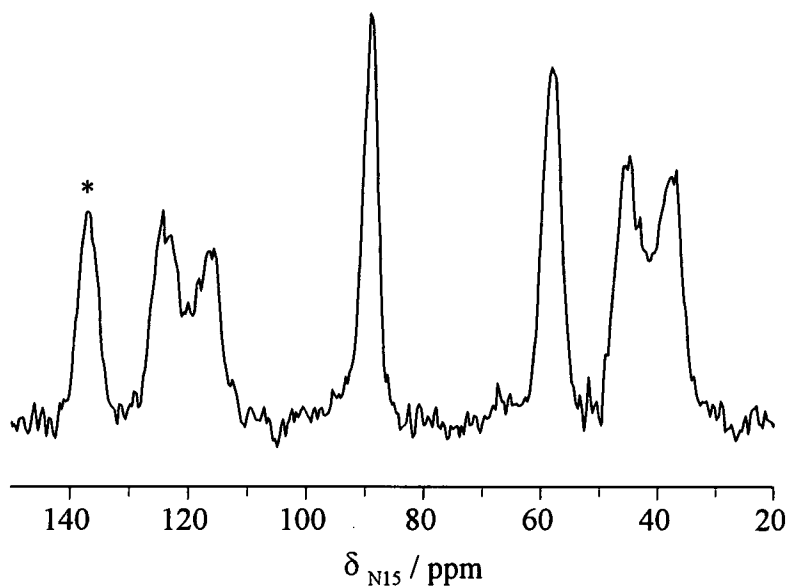


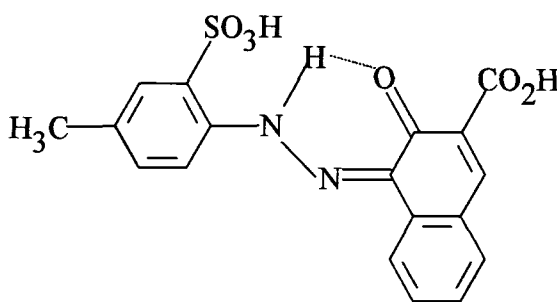
Figure 7

*¹⁵N CP/MAS spectrum of DR278 form A at the $n=1$ rotational resonance condition and 30.3 MHz. A spin rate of 2330 Hz was used which matches the 121 and 44 ppm resonances. * indicates a spinning sideband from the 60 ppm resonance.*

For systems which have even poorer spectral resolution and/ or smaller dipole coupling constants the lineshape calculation technique becomes a highly inaccurate method of extracting bond lengths. A far more accurate method for these systems is analogous to the chemical exchange driven selective polarisation inversion experiment discussed in Chapter 4. This experiment involves the transfer of coherence order from one spin to the other, which it is directly coupled to, under conditions of rotational resonance. Polarisation transfer between the two spins results in a dephasing of the individual spin intensities, and the difference signal is oscillatory in nature. The exact time dependence of the difference magnetisation under R^2 conditions is determined by a number of parameters: the homonuclear dipolar coupling constant (D'), the principal values of the I and S shift tensors, the

relative orientations of the shift and dipolar tensors and the zero-quantum relaxation time (T_2^{ZQ}).

The ^{15}N CP/ MAS spectrum of the monohydrate calcium salt of the pigment 1-(2-sulpho-4-methylphenylazo)-2-hydroxynaphthalene-3-carboxylic acid (CI PR 57:1), (II), shows a rather broad lineshape, with a linewidth of over 200 Hz. Consequently, determination of an ~ 60 Hz splitting would be impossible, negating the use of lineshape calculations.



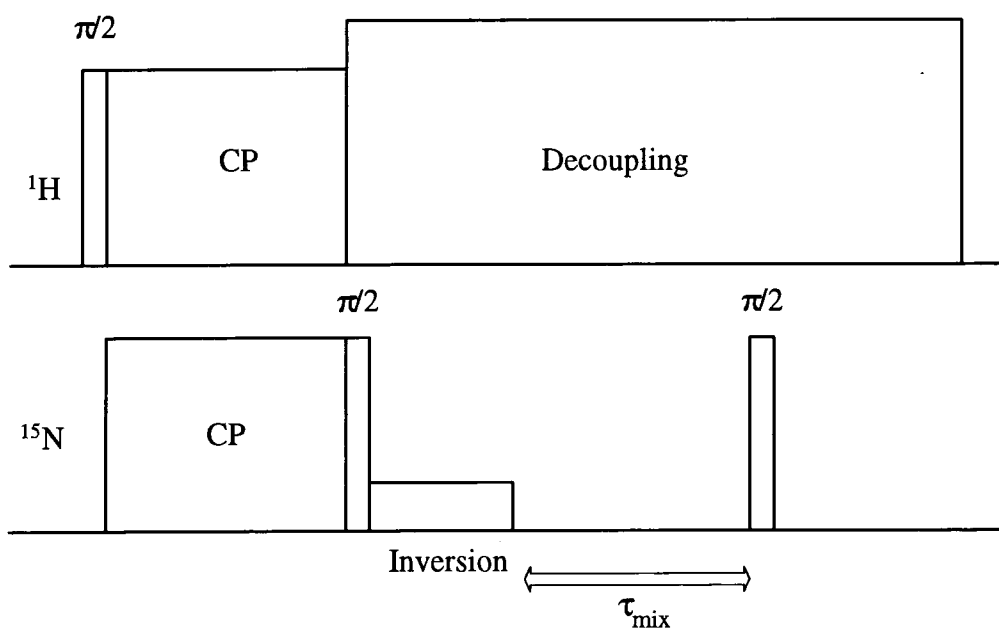
II

The magnetisation transfer pulse sequence shown below was used to obtain the difference magnetisation curves. The hard $\pi/2$ pulse places this magnetisation along the z-axis. The polarisation inversion, in this case, is created via a weak selective pulse. A hard read pulse is finally applied after a variable mixing time, τ_{mix} , which allows for the transfer of coherence between the two spins. The difference magnetisation is plotted as a function of the mixing time in Figure 8. As expected from theory a damped oscillation is observed.

The equation for the time evolution of the difference magnetisation is given in the paper by Levitt,⁴⁰ and for the case given here it was found to be (equation 86 in ref.40):

$$\langle I_z - S_z \rangle(t) \cong e^{-rt/2} \cos\left\{ \left| \tilde{\omega}_B^{(n)} \right| t \right\}$$

where $r = (T_2^{ZQ})^{-1}$ and $\tilde{\omega}_B^{(n)}$ is the resonant fourier component



Magnetisation transfer sequence used to obtain the R^2 difference signal.

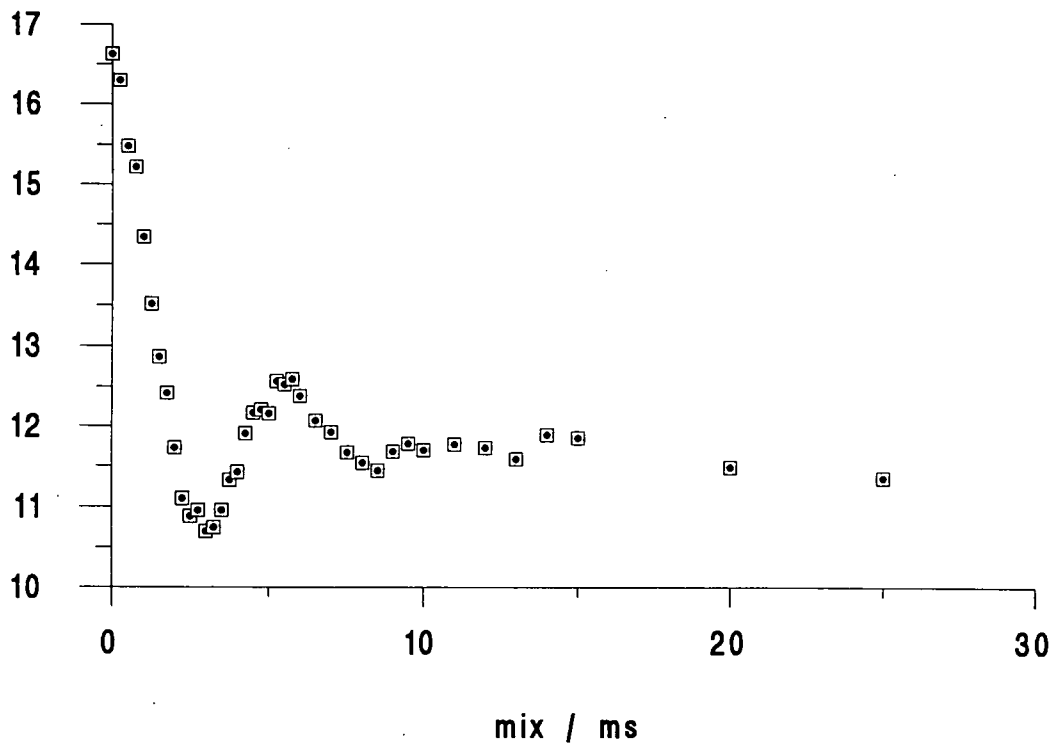


Figure 8

Experimental magnetisation exchange curve for doubly labelled PR 57:1 at the $n=1$ rotational resonance condition. The data were recorded at 30.4 MHz with a spin rate of 5.13 kHz. The spectra were acquired with 1200 transients per point, a contact time of 10 ms, a 200 μ s inversion pulse, a recycle delay of 2 s. 40 data points were obtained.

References.

- 1 G.C. Levy and R. L. Lichter, '¹⁵N NMR Spectroscopy', Wiley Interscience, New York, (1979).
- 2 G.J. Martin, M.L. Martin and J. P. Gouesnard, *NMR Basic Principles Prog.*, **18**, 341, (1981).
- 3 J. Mason, 'Nitrogen NMR', in '*Encyclopedia of Nuclear Magnetic Resonance*', eds D. M. Grant and R. K. Harris, Wiley, London, (1996).
- 4 M. Witanowski and G.A. Webb (eds), 'Nitrogen NMR', Plenum Press, London, (1973).
- 5 J. Mason, in 'Multiuclear NMR', ed J. Mason, Plenum Press, New York, Chap. 12, 335-367, (1987).
- 6 R. Tycko, P. L. Stewart and S. J. Opella, *J. Am. Chem. Soc.*, **108**, 5419-5424, (1986).
- 7 R. Tycko and S. J. Opella, *J. Am. Chem. Soc.*, **108**, 3531-3532, (1986).
- 8 I. Mills, T. Cvitas, K. Homann, N. Kally and K. Kuchitsu, 'Quantities, Units and Symbols in Physical Chemistry', Blackwell (for IUPAC), Oxford, 98-104, (1993).
- 9 N.F. Ramsey, *Phys. Rev.*, **77**, 567, (1950); **78**, 699-703, (1950); **83**, 540-541, (1951); **86**, 243-246, (1952)
- 10 J. Kroner, W. Schneid, N. Wiberg, B. Wrackmeyer and G. Ziegler, *J. Chem. Soc. Faraday Trans. 2.*, **74**, 1909-1919, (1974).
- 11 J. Facelli and D. M. Grant, *Theor. Chim. Acta.*, **71**, 277, (1987).
- 12 M. Witanowski, Z. Biedrzycka, W. Sicinska, Z. Grabowski, G. A. Webb, *J. Magn. Reson.*, **120**, 148, (1996)
- 13 J. C. Facelli, R. J. Pugmire and D. M. Grant, *J. Am. Chem. Soc.*, **118**, 23, 5488-5489, (1996).

- 14 K. L. Anderson-Altmann, C. G. Phung, S. Mavromoustakos, Z. Zheng, J. C. Facelli, C. D. Poulter and D.M. Grant, *J Phys. Chem.*, **99**, 10454, (1995).
- 15 S. G. Kukolich, *J. Am. Chem. Soc.*, **97**, 5704, (1975).
- 16 J. Raymonda and W. Klemperer, *J. Chem. Phys.*, **55**, 232, (1971).
- 17 R. E. Wasylishen, W. P. Power, G. H. Penner and R. D. Curtis, *Can. J. Chem.*, **67**, 1219, (1989).
- 18 J. O. Freidrich and R. E. Wasylishen, *J. Chem. Phys.*, **83**, 3707, (1985).
- 19 L. Delmotte, M. Soulard and H. Kessler, *Chem. Lett.*, 1215, (1990).
- 20 D. Schweitzer and H. W. Speiss, *J. Magn. Reson.*, **15**, 529, (1974).
- 21 D. G. Powell and L. J. Mathias, *J. Am. Chem. Soc.*, **112**, 669, (1990).
- 22 M. Sardashti and G. E. Maciel, *J. Phys. Chem.*, **92**, 4620, (1988).
- 23 J. Z. Hu, B. Yang, L. Li, J. Qui, C. Ye, R. J. Pugmire, M. S. Solum, R. Wind and D. M. Grant, *Solid State NMR*, submitted for publication.
- 24 D. W. Aldermann, M. S. Solum and D.M. Grant, *J. Chem. Phys.*, **84**, 3717, (1986).
- 25 J. Herzfeld and A. Berger, *J. Chem. Phys.*, **73**, 6021, (1980).
- 26 R. D. Curtis, J. W. Hilborn, G. Wu, M. D. Lumsden, R. E. Wasylishen and J. A. Pincork, *J. Phys. Chem.*, **97**, 1856, (1993).
- 27 T. G. Oas, C. J. Hartzell, T. J. McMahon, G. P. Drobny and F. W. Dahlquist, *J. Am. Chem. Soc.*, **109**, 5956, (1987).
- 28 T. G. Oas, C. J. Hartzell, G. P. Drobny and F. W. Dahlquist, *J. Am. Chem. Soc.*, **109**, 5962, (1987).
- 29 C. J. Hartzell, M. Whitfield, T. G. Oas and G. P. Drobny, *J. Am. Chem. Soc.*, **109**, 5966, (1987).
- 30 K. W. Zilm and D. M. Grant, *J. Am. Chem. Soc.*, **103**, 2913, (1981).
- 31 J. Mason, *Solid State NMR*, **2**, 285, (1993).

- 32 a. L. H. Merwin, *PhD Thesis*, University of Durham, (1987).
b. H. Bai, *PhD Thesis*, University of Durham, (1991).
- 33 R. D. Curtis, W. P. Power, G. H. Penner and R. E. Wasylshen, *J. Phys. Chem.*, **94**, 4000, (1990).
- 34 a. R. E. Wasylshen, G. H. Penner, W. P. Power and R. D. Curtis, *J. Am. Chem. Soc.*, **111**, 6082, (1989).
b. J. Mason, D. M. Mingas, J. Schaefer, D. Sherman and E. O. J. Stejskal, *J. Chem. Soc. Chem. Com.*, 444, (1985).
c. P. A. Duffin, L. F. Lankworthy, J. Mason, A. N. Stephens and R. M. Thompson, *Inorg. Chem.*, **26**, 2034, (1987).
- 35 M. G. Munowitz and R. G. Griffin, *J. Chem. Phys.*, **76**, 2848, (1982).
- 36 J. M. Griffiths and R. G. Griffin, *Anal. Chimica Acta.*, **283**, 1081-1101, (1993).
- 37 A. E. Bennet, R. G. Griffin and S. Vega, *NMR Basic Principles Prog.*, **33**, 1-77, (1994).
- 38 R. R. Ernst, G. Bodenhausen and A. Wokaun, pp 516, 'Principles of Nuclear Magnetic Resonance in One and Two Dimensions.', Clarendon Press, Oxford, 1991.
- 39 a. R. Tycko and G. Dabbagh, *Chem. Phys. Lett.*, **173**, 461, (1990).
b. A. E. Bennet, J. H. Ok, S. J. Vega and R. G. Griffin, *J. Chem. Phys.*, **96**, 8634, (1992).
c. T. Gullion and J. Schaefer, *J. Magn. Reson.*, **81**, 196, (1989).
d. T. Gullion and S. Vega, *Chem. Phys. Lett.*, **194**, 423, (1992).
- 40 M. H. Levitt, D. P. Raleigh, F. Cruzet and R. G. Griffin, *J. Chem. Phys.*, **92**, 6347, (1990).
- 41 A. Schmidt and S. Vega, *J. Chem. Phys.*, **96**, 2655, (1992).
- 42 A. Kubo and C. A. McDowell, *J. Chem. Phys.*, **93**, 7156, (1990).
- 43 R. Challoner and R. K. Harris, *Chem. Phys. Lett.*, **228**, 589, (1994).

7. Magic-Angle Turning Spectroscopy.

7.1 Introduction.

In the previous chapter it was shown that knowledge of the principal components of the shift tensor can provide useful structural information. However, increasing the number of overlapping powder patterns in a static spectrum, or spinning sideband manifolds in a MAS spectrum, can significantly increase the complexity of the observed spectrum. The spectral congestion that arises renders it virtually impossible to accurately determine the shift tensor components for such systems.

Several ingenious techniques have been developed to allow the determination of the anisotropic shielding components for multiple sites. These include magic-angle hopping,¹ stop-and-go,² spin-lock rotational resonance,³ and rotor-synchronised multiple pulse trains.⁴ One additional class of experiment is based on the magic-angle turning (MAT) technique introduced by Gan,⁵ where the sample is slowly rotated, and a multiple-pulse sequence is applied during the evolution period within a two-dimensional pulse sequence. Several modifications of the MAT sequence have been developed by Hu *et al.*^{6, 7} to improve the signal-to-noise ratio and other spectral features. For a review of these techniques, including the previously mentioned alternatives the reader is directed to articles by Orendt,⁸ Hu⁹ and Speiss.¹⁰

7.2 Theory of MAT.

It was realised by Bax *et al.*¹¹ that if during the evolution time the sample was placed successively, “hopped”, at 120° intervals about the magic-angle axis then it was possible to obtain the pure isotropic shift. This is a result of the fact that in the molecular frame the static field is rotated by 90°, and the average of three orthogonal orientations is simply the trace of the tensor. The magic-angle hopping (MAH) experiment provides good results, but it cannot be used on commercial systems. This problem was solved by Gan, who subtly modified the technique to involve slow continuous rotation of the sample, along with suitable pulse timing during the evolution period of the sequence, such that the magnetisation was stored at one third fractions of the rotor period (same sequence as MAH). The spin-rate is sufficiently slow such that a pseudo-static powder pattern is obtained. A distinct advantage of MAT is that it can be carried out on standard commercial probes, unlike the MAH experiment.

The prototype MAT sequence is given in Figure 1. The initial X channel magnetisation is created via a standard CP preparation sequence. This point in the sequence can be considered to be $t=0$. Following this the magnetisation is allowed to precess through an angle Φ_1 during a time $t_1/3$. A component of this magnetisation is stored in the z direction for a fixed period by a projection pulse p_1 , and then returned to the transverse plane at $t=T/3$ by the read pulse r_1 . Free precession then occurs again for $t_1/3$, with the magnetisation acquiring a phase angle of Φ_2 , before being projected back along the z axis by pulse p_2 . At $t=2T/3$ this process is repeated such that a phase angle of Φ_3 is acquired by the magnetisation, which is then stored

along the Z- axis. The final magnetisation is then returned to the transverse plane and the spectrum is recorded.

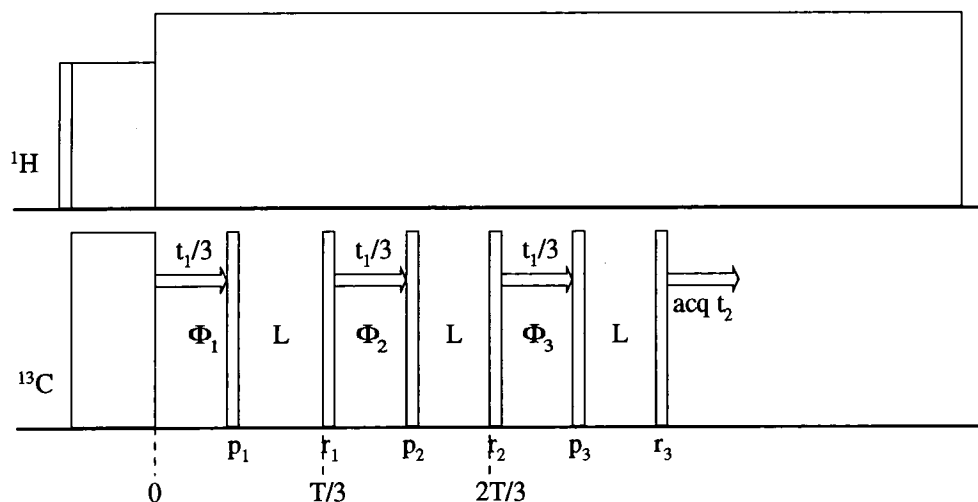


Figure 1

Pulse sequence for the prototype MAT. Narrow rectangles represent 90° pulses and the magnetisation is stored along the longitudinal axis as indicated by L. T is the rotor period.

The acquired phase angles Φ_1 , Φ_2 and Φ_3 can be written as time integrals of the time-dependent angular frequency $\omega(\gamma(t))$, which is a function of the rotor position $\gamma(t)$. Thus

$$\begin{aligned}\Phi_1 &= \int_0^{t_1/3} \omega(\gamma(t)) dt \\ \Phi_2 &= \int_{T/3}^{T/3+t_1/3} \omega(\gamma(t)) dt = \int_0^{t_1/3} \omega(\gamma(t+T/3)) dt \\ \Phi_3 &= \int_{2T/3}^{2T/3+t_1/3} \omega(\gamma(t)) dt = \int_0^{t_1/3} \omega(\gamma(t+2T/3)) dt\end{aligned}\quad (1)$$

The sum of these precession angles is the sum of the integrals

$$\Phi_1 + \Phi_2 + \Phi_3 = \int_0^{t_1/3} \omega(\gamma(t)) dt + \int_0^{t_1/3} \omega(\gamma(t+T/3)) dt + \int_0^{t_1/3} \omega(\gamma(t+2T/3)) dt$$

and combining these integrals gives

$$\Phi_1 + \Phi_2 + \Phi_3 = \int_0^{t_1/3} [\omega(\gamma(t)) + \omega(\gamma(t + T/3)) + \omega(\gamma(t + 2T/3))] dt$$

Because the static field is aligned along 3 mutually perpendicular orientations, for each component within the integral, then the expression simplifies to

$$\Phi_1 + \Phi_2 + \Phi_3 = \int_0^{t_1/3} 3\omega_{iso} dt = \omega_{iso} t_1$$

To obtain an amplitude modulation of the FIDs by $\cos(\Phi_1 + \Phi_2 + \Phi_3)$ and $\sin(\Phi_1 + \Phi_2 + \Phi_3)$ one must phase-cycle the projection pulses p_1 , p_2 and p_3 according to the triple-angle formulas

$$\begin{aligned} \cos(\Phi_1 + \Phi_2 + \Phi_3) &= \cos(\Phi_1) \cos(\Phi_2) \cos(\Phi_3) \\ &\quad - \sin(\Phi_1) \sin(\Phi_2) \cos(\Phi_3) \\ &\quad - \sin(\Phi_1) \cos(\Phi_2) \sin(\Phi_3) \\ &\quad - \cos(\Phi_1) \sin(\Phi_2) \sin(\Phi_3) \end{aligned} \quad (2)$$

and

$$\begin{aligned} \sin(\Phi_1 + \Phi_2 + \Phi_3) &= \sin(\Phi_1) \cos(\Phi_2) \cos(\Phi_3) \\ &\quad + \cos(\Phi_1) \sin(\Phi_2) \cos(\Phi_3) \\ &\quad + \cos(\Phi_1) \cos(\Phi_2) \sin(\Phi_3) \\ &\quad - \sin(\Phi_1) \sin(\Phi_2) \sin(\Phi_3) \end{aligned} \quad (3)$$

Thus, a 2D amplitude-modulated hypercomplex FID $F(t_1, t_2)$ is obtained. Since the rotation frequency of the sample is ~ 30 Hz then the t_2 dimension yields a pseudo-static powder spectrum, while t_1 yields the isotropic spectrum, free of spinning sidebands only, upon Fourier transformation. Additionally, since the rotation frequency is slow, in comparison to dipolar couplings, then weak scalar dipolar couplings are not removed from the anisotropic dimension.

In this prototype MAT experiment the transverse magnetisation is stored along the longitudinal axis three times, with each projection losing a portion of the magnetisation, which significantly reduces the signal-to-noise ratio. This is a real drawback since it is a low-sensitivity experiment due to the observation of broad lines. By applying only two projection pulses then there would be a significant increase in signal-to-noise. Two such techniques have been developed which address this issue- triple-echo MAT^{6, 12} and PHase cORrected MAT (PHORMAT). The method of choice used here is the PHORMAT technique given by the two sequences given in Figure 2.

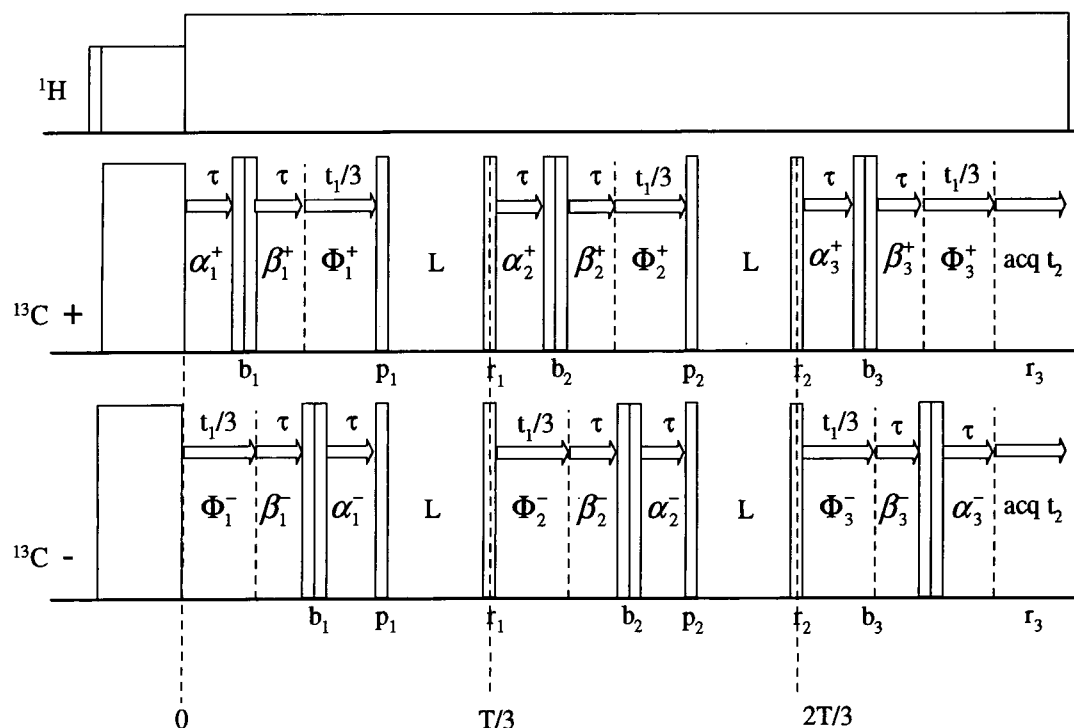


Figure 2

Pulse sequences for the PHORMAT experiment. 90° pulses are represented by narrow rectangles, and two adjacent rectangles denote a 180° pulse. The magnetisation is stored along the Z-axis during the periods labelled L, and it precesses in the transverse plane at all other times.

It is impossible to obtain an amplitude modulation, while retaining the pure absorption-absorption lineshape desired with quadrature detection of the evolution dimension, using only one sequence as in the prototype sequence. Phase cycling of the two projection pulses p_1 and p_2 in the + pulse sequence yields an amplitude modulation of the FID by the cosines and sines of the phase angles $(-\alpha_1 + \beta_1 + \Phi_1)$ and $(-\alpha_2 + \beta_2 + \Phi_2)$. However, during the final third of the evolution period the FID is phase modulated by the phase angle $(-\alpha_3 + \beta_3 + \Phi_3)$. The evolution of the t_1 dimension occurs after the 180° refocusing pulse during the Φ components. The four individual FIDs for the + sequence are thus

$$F_{cc}^+ = \cos(-\alpha_1^+ + \beta_1^+ + \Phi_1^+) \cos(-\alpha_2^+ + \beta_2^+ + \Phi_2^+) \exp[i(-\alpha_3^+ + \beta_3^+ + \Phi_3^+)] F(t_2)$$

$$F_{cs}^+ = \cos(-\alpha_1^+ + \beta_1^+ + \Phi_1^+) \sin(-\alpha_2^+ + \beta_2^+ + \Phi_2^+) \exp[i(-\alpha_3^+ + \beta_3^+ + \Phi_3^+)] F(t_2)$$

$$F_{sc}^+ = \sin(-\alpha_1^+ + \beta_1^+ + \Phi_1^+) \cos(-\alpha_2^+ + \beta_2^+ + \Phi_2^+) \exp[i(-\alpha_3^+ + \beta_3^+ + \Phi_3^+)] F(t_2)$$

$$F_{ss}^+ = \sin(-\alpha_1^+ + \beta_1^+ + \Phi_1^+) \sin(-\alpha_2^+ + \beta_2^+ + \Phi_2^+) \exp[i(-\alpha_3^+ + \beta_3^+ + \Phi_3^+)] F(t_2)$$

Combination of these FIDs as follows gives the signal-averaged FID F^+

$$F^+ = F_{cc}^+ - F_{ss}^+ + iF_{cs}^+ + iF_{sc}^+$$

where multiplication by i means a 90° phase shift of the acquisition FID. Addition of the individual FIDs results in the following simplified equation

$$F^+ = \{ \cos(\omega_{iso} t_1) + i \sin(\omega_{iso} t_1) \} F(t_2) \quad (4)$$

By allowing the evolution to occur prior to the 180° refocusing pulse, which is equivalent to a time reversal of the chemical shift evolution, a similar series of FIDs can be written for the - pulse sequence shown in Figure 2.

$$F_{cc}^- = \cos(+\alpha_1^- - \beta_1^- - \Phi_1^-) \cos(+\alpha_2^- - \beta_2^- - \Phi_2^-) \exp[i(+\alpha_3^- - \beta_3^- - \Phi_3^-)] F(t_2)$$

$$F_{cs}^- = \cos(+\alpha_1^- - \beta_1^- - \Phi_1^-) \sin(+\alpha_2^- - \beta_2^- - \Phi_2^-) \exp[i(+\alpha_3^- - \beta_3^- - \Phi_3^-)] F(t_2)$$

$$F_{sc}^- = \sin(+\alpha_1^- - \beta_1^- - \Phi_1^-) \cos(+\alpha_2^- - \beta_2^- - \Phi_2^-) \exp[i(+\alpha_3^- - \beta_3^- - \Phi_3^-)] F(t_2)$$

$$F_{ss}^- = \sin(+\alpha_1^- - \beta_1^- - \Phi_1^-) \sin(+\alpha_2^- - \beta_2^- - \Phi_2^-) \exp[i(+\alpha_3^- - \beta_3^- - \Phi_3^-)] F(t_2)$$

Application of the same combination of these FIDs gives the signal-averaged FID F^-

$$F^- = F_{cc}^- - F_{ss}^- + iF_{cs}^- + iF_{sc}^-$$

which simplifies to

$$F^- = \{\cos(\omega_{iso}t_1) - i \sin(\omega_{iso}t_1)\} F(t_2) \quad (5)$$

The F^+ and F^- FIDs can be combined to form the real and imaginary components of a hypercomplex 2D FID F_R and F_I

$$F_R = +\frac{1}{2}(F^+ + F^-) = \cos(\omega_{iso}t_1) F(t_2)$$

$$F_I = -\frac{i}{2}(F^+ - F^-) = \sin(\omega_{iso}t_1) F(t_2)$$

The final 2D hypercomplex FID is simply written, using $j = \sqrt{-1}$ as a second imaginary unit, as

$$F = F_R + jF_I = \exp(j\omega_{iso}t_1) F(t_2) \quad (6)$$

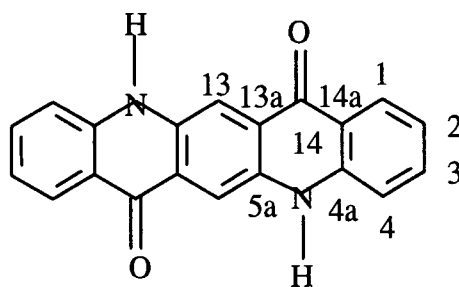
With this minimum phase cycle of four for each sequence artifacts can occur from several sources. Hu *et al.* have used a phase cycle of 32 which significantly improves the quality of the resultant spectra. The pulse sequences and acquisition macros, as written for a Chemagnetics CMX II, are shown in the appendix. These sequences were written by members of Grant's research group at the University of Utah. The manipulation of the + and - datasets can be carried out directly on the

CMX spectrometer using the Spinsight software. The program to carry out this manipulation is also given in the appendix.

7.3 Application of ^{13}C and ^{15}N PHORMAT to Dyes and Pigments.

7.3.1 CI-PV19: γ Linear-*trans*-quinacridone.

Linear-*trans*-quinacridone, I, is a pigment (a colourant which is insoluble in the medium in which it is applied to the substrate) used in the motor industry as a car paint. The Colour Index name is Pigment Violet 19 (PV19), and it exists in three crystal modifications α , β and γ with each having different colours, ranging from violet to deep purple. The presence of an inversion centre implies that, if intermolecular interactions are negligible, only half of the signals will be observed. This is experimentally observed in the solids, but the resolution of the spectra is rather poor, which may suggest that a small deviation from centrosymmetry is present.



(I)

This sample is amenable to the PHORMAT technique due to the fact that the isotropic shifts cover only a short range, ~ 80 ppm, which requires an increase in the dwell time in the second-dimension, thus reducing the experimental time needed to obtain suitable resolution in the indirectly detected dimension. This one fact is the single most important point in the PHORMAT experiment. Figure 3 shows the

comparison between the isotropic ^{13}C shift spectra as obtained by a normal CP/ MAS sequence, and by summation over the isotropic dimension in a PHORMAT experiment. This clearly shows that the isotropic spectrum can be faithfully recreated in the PHORMAT experiment, with obvious degradation of the resolution. Figure 4 shows the contour plot for the ^{13}C PHORMAT experiment obtained at 100.6 MHz. Extraction of the individual slices through the evolution dimension allows one to separate out the individual powder patterns according to isotropic shifts, as shown in Figure 5.

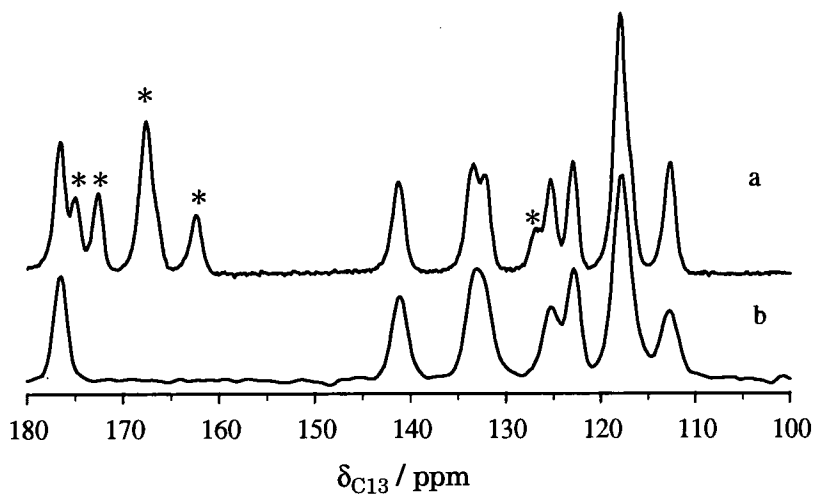


Figure 3

^{13}C spectra of PV19 γ obtained by a/ a normal CP/ MAS sequence and b/ a summation over the slices in the indirectly detected (isotropic) dimension in a PHORMAT experiment. * Indicate sidebands.

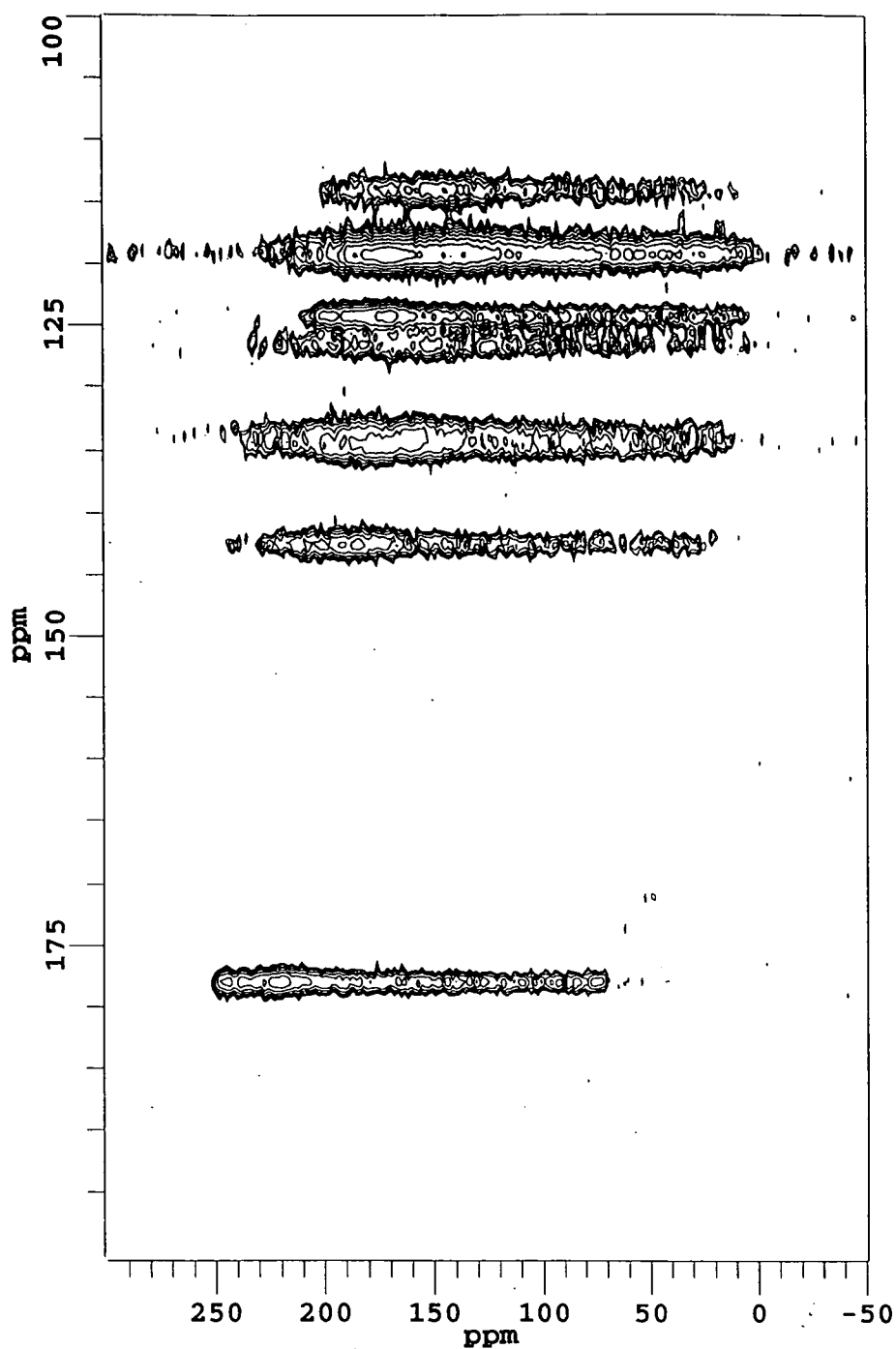


Figure 4

Contour plot of the ^{13}C PHORMAT spectrum of PV19 γ . A spectral width of 80 kHz was used in the t_2 dimension and 12.5 kHz in the t_1 dimension. 100 points were obtained in the evolution dimension to produce a digital resolution of 120 Hz. 100 Hz Gaussian line broadening was applied to both dimensions. The lowest contour level is 10% of the maximum peak height.

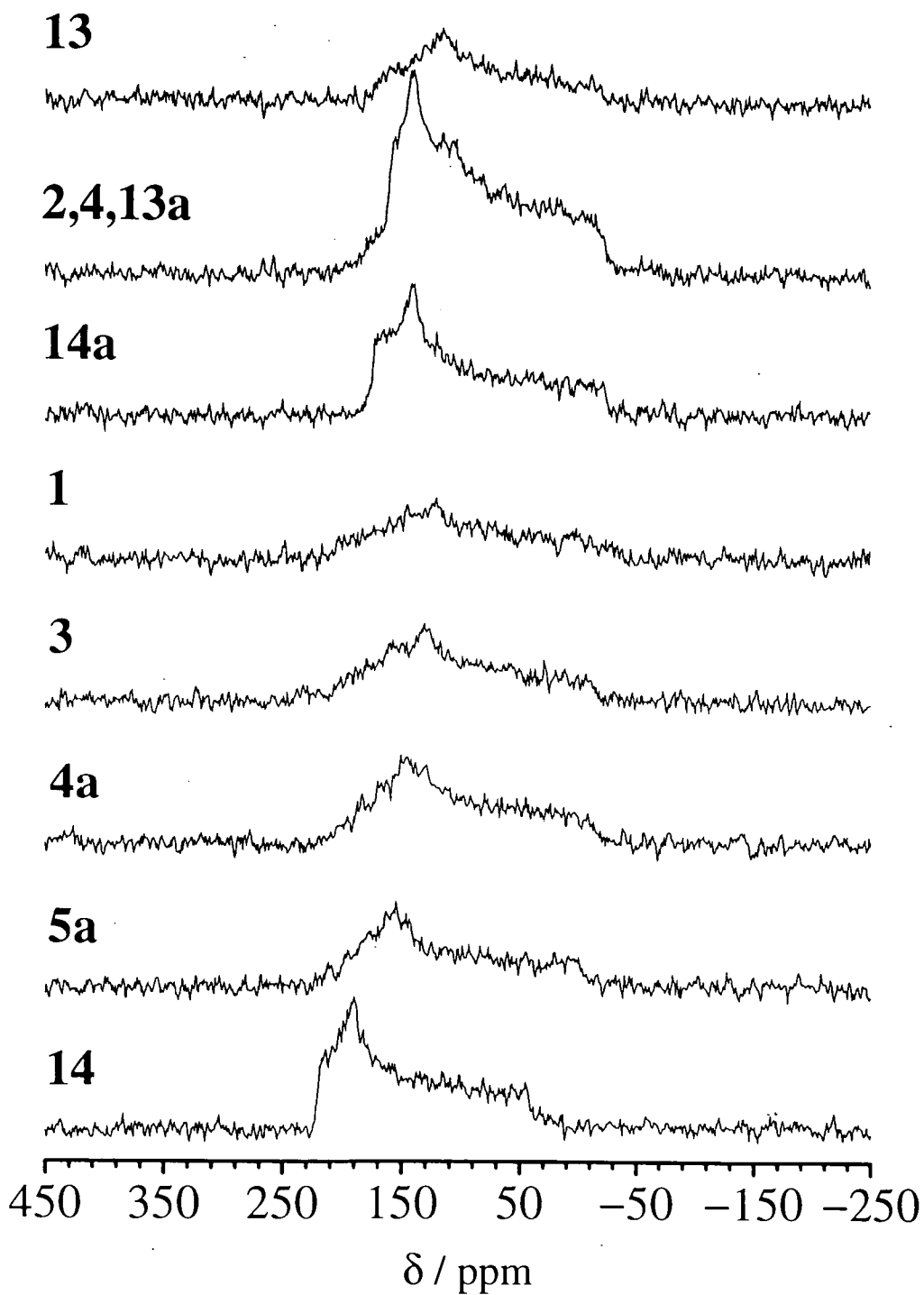


Figure 5

Slices taken through the PHORMAT spectrum as shown in Figure 4 to give the individual powder patterns.

Table 1 shows both the chemical shift assignment of ^{13}C resonances for PV19 γ and their corresponding principal components of the shift tensor. The shift components were obtained by fitting the individual slices independently using the program outlined earlier. The slice at 118 ppm is a superposition of three peaks and it would be possible to fit the lineshape to several lines. However, in the present case it was fitted to one powder pattern for the sake of simplicity. All of the fitted isotropic shifts are within 5 ppm of the actual values as obtained from the isotropic dimension in the PHORMAT experiment, which shows that the quality of the fitting is rather good.

	δ_{11}	δ_{22}	δ_{33}	$\delta_{\text{iso}}(\text{fit})$	$\delta_{\text{iso}}(\text{actual})$
C1	223	149	-6	122	125.4
C2,4, 13a	181	166	-1	115	118.0
C3	223	156	8	129	132.5
C4a	215	164	8	129	133.4
C5a	224	179	13	139	141.2
C14a	199	164	-2	121	122.9
C13	194	139	4	112	112.8
C14	244	214	61	173	176.6

Table 1

Principal components of the shift tensor for PV19 γ as obtained by fitting the slices from the PHORMAT data as shown in Figure 5.

Values are given in ppm relative to TMS.

7.3.2 DR278 VI

It was hoped that it would be possible to acquire a good quality PHORMAT spectrum from this polymorph of DR278, since it has a significantly shorter T_1 relaxation time in comparison to the other two polymorphs. The presence of both aromatics and aliphatics requires a large spectral width in the evolution dimension, and to resolve the aromatic signals sufficiently requires a high number of points to be collected in the second dimension. Truncation of the FID in the second dimension produces Gibbs wiggles which interfere in such a manner that the isotropic lines may be obscured.

In the static ^{13}C spectrum, Figure 6a, one can see two distinct spectral features. These arise from the aliphatic and aromatic signals. However, due to the complexity of the spectral features it is impossible to obtain the principal components of the ^{13}C shift tensor. Thus, it would seem a suitable candidate for application of the PHORMAT sequence. The ^{13}C PHORMAT spectrum for DR278 VI is shown as a contour plot in Figure 6b. The narrow SA of the aliphatic signals produces suitably strong intensities in that region, but the aromatic ^{13}C resonances, having significantly larger SA, show up as much weaker signals. The combination of Gibbs wiggles in the indirectly detected dimension and low signal intensity produces rather poor-quality results in the aromatic region as seen in Figure 6b.

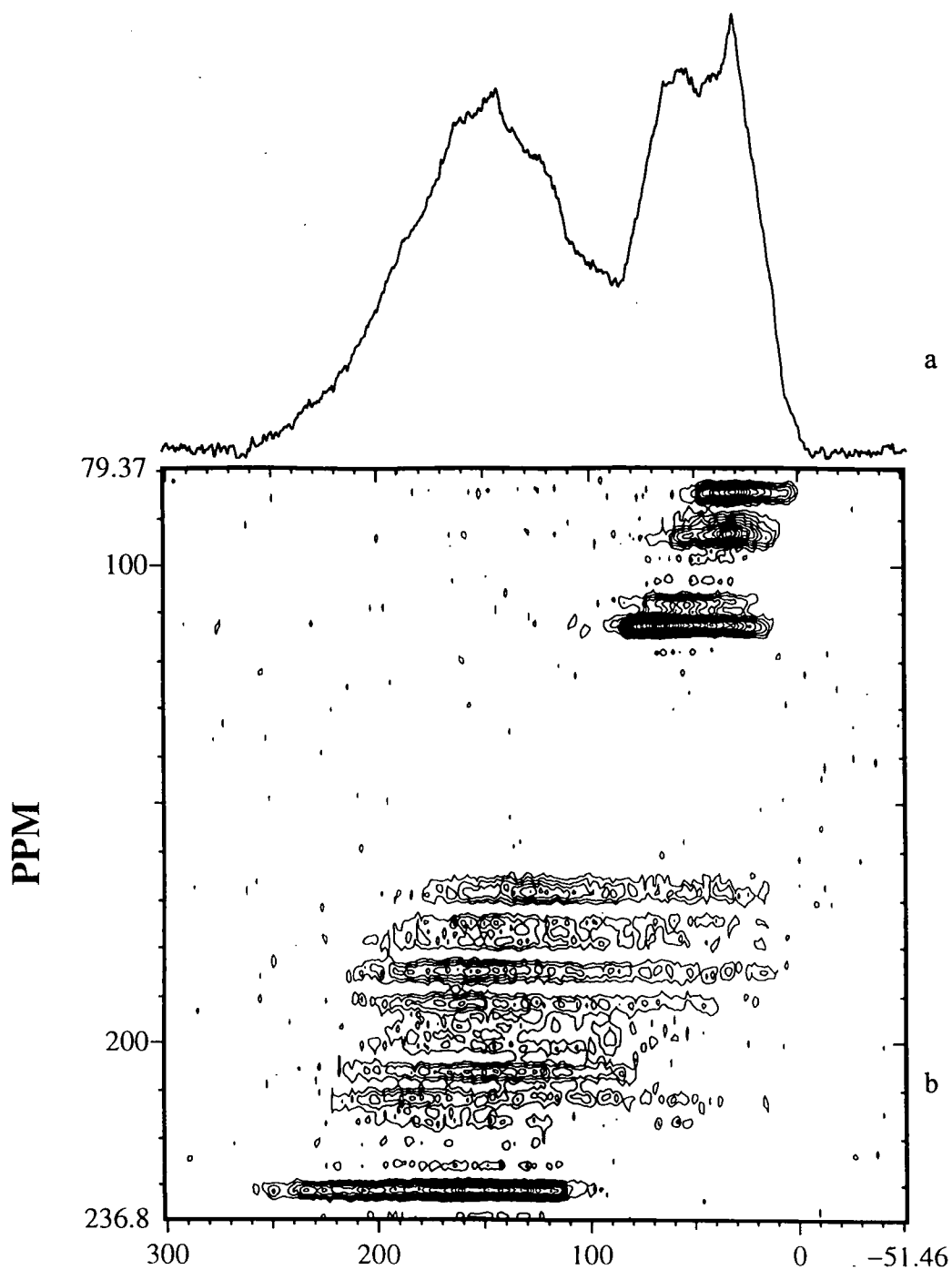
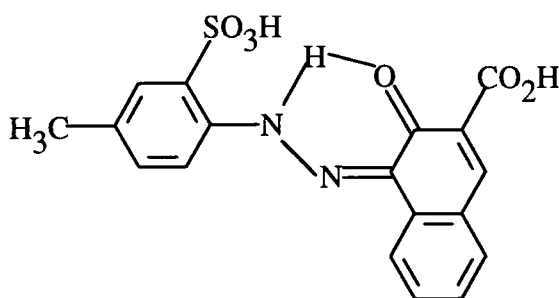


Figure 6

^{13}C spectra of DR278 VI recorded at 100.6 MHz. a/ is the static spectrum recorded with a Hahn-echo sequence and b/ is a contour plot of the PHORMAT experiment.

7.3.3 CI Pigment Red 57:1

In Chapter 5 the azo and hydrazone ^{15}N shift tensors were analysed for the phenylazophenol derivatives. With this work as a starting point it was decided to try to understand the equilibrium conformation of the monohydrate calcium salt of the pigment 1-(2-sulpho-4-methylphenylazo)-2-hydroxynaphthalene-3-carboxylic acid (CI PR 57:1), II. A doubly ^{15}N -enriched sample was synthesised by Jonsen who suggested that the equilibrium position favoured the hydrazo tautomer, as drawn.¹³



II

The two ^{15}N powder patterns overlap at ~ 0 ppm making it difficult to determine the low-frequency component of the $\text{N}=\text{C}$ signal, and high-frequency component of the $\text{N}-\text{H}$ signal. Application of the PHORMAT sequence is shown in Figure 7 as a contour plot. The low signal-to-noise ratio, and the fact that the dipolar coupling only slightly perturbs the spectral structure makes it valid to fit the individual slices by considering the shielding tensor only. The results of this fitting are shown in Table 2. Comparison of the $\text{N}=\text{C}$ principal components with those given in Table 5 in Ch.6 for the acid samples confirms that PR 57:1 is indeed present as the hydrazo tautomer. Due to lack of investigations that have been carried out on the shift tensors of these systems the exact equilibrium constant for the azo/ hydrazone tautomerism cannot be obtained.

	δ_{11}	δ_{22}	δ_{33}	δ_{iso} (fit)	δ_{iso} (actual)
N-H	-6	-189	-318	-171	-169.4
N=C	339	3	-347	-2	-1.2

Table 2

Principal components of the ^{15}N shift tensor for PR 57:1. Values are given in ppm relative to the signal for CH_3NO_2 .

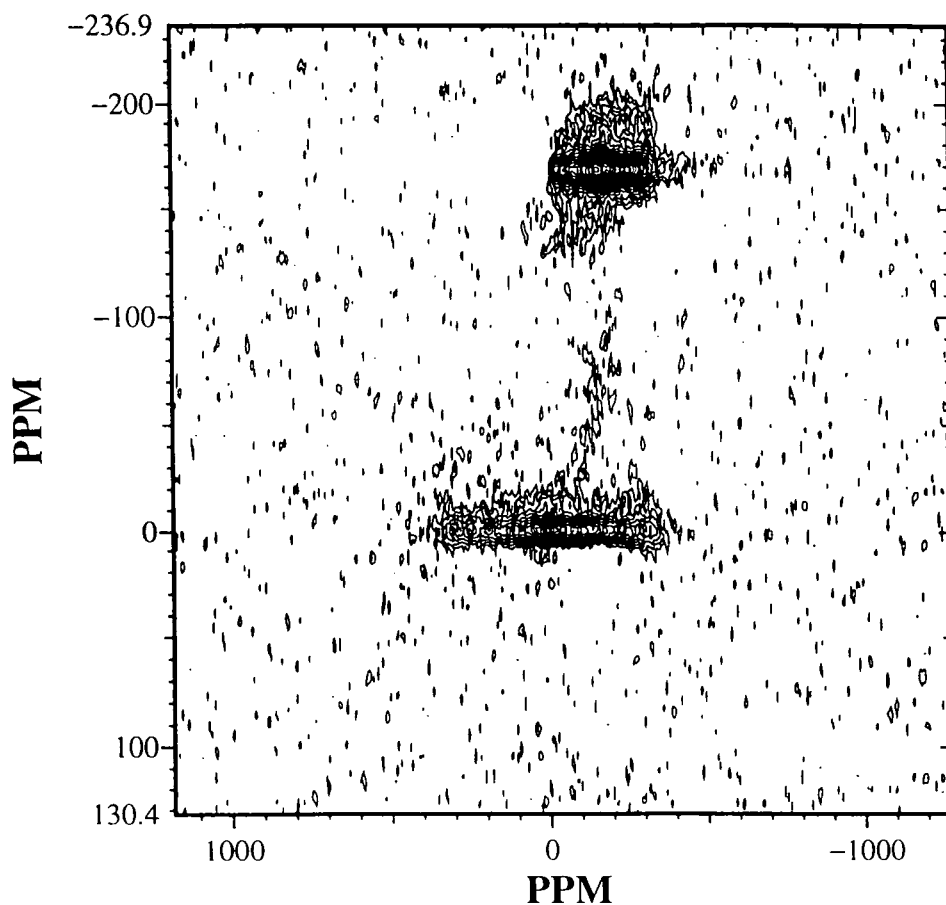


Figure 7

^{15}N PHORMAT spectrum of PR 57:1 as represented by a contour plot.

Conclusions.

For multiple spin systems where one-dimensional techniques negate the determination of the principal components of the shift tensor, PHORMAT has proven to be a useful, yet time-consuming, technique for separating out the individual powder patterns. The sequence can be modified quite simply by including a dipolar dephasing window during the evolution period (to select quaternary signals), and also to extend to three dimensions. Future applications will no doubt concentrate on high-sensitivity nuclei which will reduce the acquisition time to more manageable values, with ^{31}P and ^{19}F being obvious examples.

Acknowledgements.

I would like to thank Professor D. M. Grant at the University of Utah for the invitation to carry out the PHORMAT experiments within his lab. I am extremely grateful to Dr. M. S. Solum for teaching me how to use the PHORMAT experiment and also for the kind use of his fitting routine for the static lineshape calculations. Thanks are also due to Dr. P. Jonsen for synthesising the PR57:1 pigment.

References

- 1 N. M. Szeverenyi, A. Bax and G. E. Maciel, *J. Magn. Reson.*, **51**, 400, (1983).
- 2 R. C. Zeigler, R. A. Wind and G. E. Maciel, *J. Magn. Reson.*, **79**, 299-306, (1988).
- 3 Z. Gan, D. M. Grant and R.R. Ernst, *Chem. Phys. Lett.*, **254**, 349, (1996).
- 4 R. Tycko, G. Dabbagh and P. A. Mirau, *J. Magn. Reson.*, **85**, 265-274, (1989).
- 5 Z. Gan, *J. Am. Chem. Soc.*, **114**, 8307, (1992).
- 6 J. Z. Hu, A. M. Orendt, D. W. Alderman, R. J. Pugmire, C. Ye and D. M. Grant, *Solid State Nucl. Magn. Reson.*, **3**, 181, (1994).
- 7 J. Z. Hu, W. Wang and R. J. Pugmire, 'Magic Angle Turning and Hopping', in 'Encyclopedia of Nuclear Magnetic Resonance', eds D. M. Grant and R. K. Harris, Wiley, London, (1996).
- 8 A. Orendt, 'Chemical Shift Tensor Determination', in 'Encyclopedia of Nuclear Magnetic Resonance', eds D. M. Grant and R. K. Harris, Wiley, London, (1996).
- 9 J. Z. Hu, W. Wang, F. Lui, M. S. Solum, D. W. Alderman, R. J. Pugmire and D. M. Grant, *J. Magn. Reson.*, **113**, 210-222, (1995).
- 10 K. Schmidt-Rohr and H. W. Spiess, *Multidimensional Solid-State NMR and Polymers*, Ch. 6, Academic Press, London, (1994).
- 11 N. M. Szeverenyi, A. Bax and G. E. Maciel, *J. Magn. Reson.*, **52**, 147-152, (1983).
- 12 W. Wang, J. Z. Hu, D. W. Alderman, R. J. Pugmire and D. M. Grant, *Solid State Nucl. Magn. Reson.*, **5**, 257, (1995).
- 13 P. Jonsen, *PhD. Thesis*, University of East Anglia, (1984).

Appendix.

Index of the Appendix.

Research Conducted Outside the Department.	169
Publications.....	170
Papers Presented and Conferences Attended.	170
Colloquia, Lectures and Seminars from Invited Speakers.....	172
PHORMAT Pulse Sequences	180
PHORMAT Acqpars Files.....	184
PHORMAT Acquisition Macro.....	185
PHORMAT Processing Macro.	186
Acquisition Parameters for the PHORMAT Spectra Discussed in Chapter 7.....	188

Research Conducted Outside the Department.

Several short visits to *Zeneca Specialties* Research Centre, extending over all three years, were carried out to fulfil conditions set out in the CASE award scheme. During these industrial placements a diverse range of goals was achieved, which included synthesis of ^{15}N -enriched azobenzene dyestuffs, molecular modelling of motion and dyeing of polyester fibres.

During the final year (1996) a three-month visit to the University of Utah was undertaken in which it was possible to learn about the new PHORMAT experiment discussed in Chapter 7, and also to take advantage of the various field capabilities that exist in Utah. This was made possible by funds supplied from both EPSRC and Prof. D. M. Grant (within whose laboratory I was working).

Publications.

1. Solution- and Solid-State Proton Transfer from Phenols to Triphenylphosphine Oxide Studied by ^1H , ^{13}C and ^{31}P NMR Spectroscopy,
C. M. Lagier, U. Scheler, G. McGeorge, M. G. Sierra, A. C. Olivier and R. K. Harris, *J. Chem. Soc. Perkin Trans II*, 1325, (1996).
2. G. McGeorge, R. K. Harris, A. M. Chippendale and J. F. Bullock,
Conformational Analysis by Magic-Angle Spinning NMR spectroscopy for a Series of Polymorphs of a Disperse Azobenzene Dye stuff,
J. Chem. Soc. Perkin Trans II, 1733, (1996).
[Note: This work is not described in the present thesis.]

Papers Presented and Conferences Attended.**Oral Presentations.**

A Solid-State NMR Analysis of an Azobenzene Dye stuff,

Durham University Final Year Graduate Colloquia, May 1996.

N-15 as a Useful Probe to Understanding the Molecular Structures of Dyes,

University of Utah, Informal Seminar, January 1996.

Investigation of Dynamic Processes in the Solid State by NMR,

Zeneca Specialties, Coordination/ Colour CASE Conference, Delph, 31st May, 1995.

Poster Presentations.

Structural Investigations of an Azobenzene Dye by C-13 and N-15 Solid-State NMR,
G. McGeorge, R. K. Harris, A. M. Chippendale and J. F. Bullock,
37th Experimental Nuclear Magnetic Resonance Conference, Asilomar Conference
Center, California, USA, March 1996.

Understanding Solid-State Structures Without Crystallography,
G. McGeorge, R. K. Harris, A. M. Chippendale and J. F. Bullock,
ICI Sponsored Poster Competition, University of Durham, December, 1995.

*Structural Investigations of an Azobenzene Dye by C-13 and N-15 Solid-State
NMR, G. McGeorge, R. K. Harris, A. M. Chippendale and J. F. Bullock,
ISMAR, Sydney, July, 1996.

Structural Investigations by Solid-State NMR of Dyes,
G. McGeorge, R. K. Harris and A. M. Chippendale.
Royal Society of Chemistry's 12th International Meeting on NMR Spectroscopy,
UMIST, Manchester, July, 1995.

* Presented by Prof. R. K. Harris.

Colloquia, Lectures and Seminars from Invited Speakers

1993 - 1996 (August 1 - July 31)

1993.

September 13 *Prof. Dr. A.D. Schlüter, Freie Universität Berlin, Germany
Synthesis and Characterisation of Molecular Rods and Ribbons

September 13 *Dr. K.J. Wynne, Office of Naval Research, Washington, USA
Polymer Surface Design for Minimal Adhesion

September 14 *Prof. J.M. DeSimone, University of North Carolina, Chapel Hill,
USA
Homogeneous and Heterogeneous Polymerisations in
Environmentally Responsible Carbon Dioxide

September 28 Prof. H. Ila, North Eastern Hill University, India
Synthetic Strategies for Cyclopentanoids via Oxoketene Dithioacetals

October 4 *Prof. F.J. Feher, University of California, Irvine, USA
Bridging the Gap between Surfaces and Solution with Sessilquioxanes

October 14 Dr. P. Hubberstey, University of Nottingham
Alkali Metals: Alchemist's Nightmare, Biochemist's Puzzle and
Technologist's Dream

October 20 *Dr. P. Quayle, University of Manchester
Aspects of Aqueous ROMP Chemistry

October 21 Prof. R. Adams, University of South Carolina, USA
Chemistry of Metal Carbonyl Cluster Complexes : Development of
Cluster Based Alkyne Hydrogenation Catalysts

- October 27 *Dr. R.A.L. Jones, Cavendish Laboratory, Cambridge
Perambulating Polymers
- November 10 *Prof. M.N.R. Ashfold, University of Bristol
High Resolution Photofragment Translational Spectroscopy : A New
Way to Watch Photodissociation
- November 17 *Dr. A. Parker, Rutherford Appleton Laboratory, Didcot
Applications of Time Resolved Resonance Raman Spectroscopy to
Chemical and Biochemical Problems
- November 24 Dr. P.G. Bruce, University of St. Andrews
Structure and Properties of Inorganic Solids and Polymers
- November 25 *Dr. R.P. Wayne, University of Oxford
The Origin and Evolution of the Atmosphere
- December 1 Prof. M.A. McKervey, Queen's University, Belfast
Synthesis and Applications of Chemically Modified Calixarenes
- December 8 Prof. O. Meth-Cohn, University of Sunderland
Friedel's Folly Revisited - A Super Way to Fused Pyridines
- December 16 Prof. R.F. Hudson, University of Kent
Close Encounters of the Second Kind

1994

- January 26 *Prof. J. Evans, University of Southampton
Shining Light on Catalysts
- February 2 *Dr. A. Masters, University of Manchester
Modelling Water Without Using Pair Potentials
- February 9 Prof. D. Young, University of Sussex
Chemical and Biological Studies on the Coenzyme Tetrahydrofolic Acid
- February 16 Prof. K.H. Theopold, University of Delaware, USA
Paramagnetic Chromium Alkyls : Synthesis and Reactivity
- February 23 Prof. P.M. Maitlis, University of Sheffield
Across the Border : From Homogeneous to Heterogeneous Catalysis
- March 2 *Dr. C. Hunter, University of Sheffield
Noncovalent Interactions between Aromatic Molecules
- March 9 *Prof. F. Wilkinson, Loughborough University of Technology
Nanosecond and Picosecond Laser Flash Photolysis
- March 10 Prof. S.V. Ley, University of Cambridge
New Methods for Organic Synthesis
- March 25 *Dr. J. Dilworth, University of Essex
Technetium and Rhenium Compounds with Applications as Imaging Agents
- April 28 Prof. R. J. Gillespie, McMaster University, Canada
The Molecular Structure of some Metal Fluorides and Oxofluorides:
Apparent Exceptions to the VSEPR Model.
- May 12 *Prof. D. A. Humphreys, McMaster University, Canada
Bringing Knowledge to Life

- October 5 *Prof. N. L. Owen, Brigham Young University, Utah, USA
Determining Molecular Structure - the INADEQUATE NMR way
- October 19 *Prof. N. Bartlett, University of California
Some Aspects of Ag(II) and Ag(III) Chemistry
- November 2 Dr P. G. Edwards, University of Wales, Cardiff
The Manipulation of Electronic and Structural Diversity in Metal
Complexes - New Ligands
- November 3 Prof. B. F. G. Johnson, Edinburgh University
Arene-metal Clusters
- November 9 Dr G. Hogarth, University College, London
New Vistas in Metal-imido Chemistry
- November 10 Dr M. Block, Zeneca Pharmaceuticals, Macclesfield
Large-scale Manufacture of ZD 1542, a Thromboxane Antagonist
Synthase Inhibitor
- November 16 Prof. M. Page, University of Huddersfield
Four-membered Rings and β -Lactamase
- November 23 Dr J. M. J. Williams, University of Loughborough
New Approaches to Asymmetric Catalysis
- December 7 *Prof. D. Briggs, ICI and University of Durham
Surface Mass Spectrometry

1995

- January 11 Prof. P. Parsons, University of Reading
Applications of Tandem Reactions in Organic Synthesis
- January 18 *Dr G. Rumbles, Imperial College, London
Real or Imaginary Third Order Non-linear Optical Materials
- January 25 Dr D. A. Roberts, Zeneca Pharmaceuticals
The Design and Synthesis of Inhibitors of the Renin-angiotensin System
- February 1 *Dr T. Cosgrove, Bristol University
Polymers do it at Interfaces
- February 8 *Dr D. O'Hare, Oxford University
Synthesis and Solid-state Properties of Poly-, Oligo- and Multidecker Metallocenes
- February 22 Prof. E. Schaumann, University of Clausthal
Silicon- and Sulphur-mediated Ring-opening Reactions of Epoxide
- March 1 Dr M. Rosseinsky, Oxford University
Fullerene Intercalation Chemistry
- March 22 Dr M. Taylor, University of Auckland, New Zealand
Structural Methods in Main-group Chemistry
- April 26 Dr M. Schroder, University of Edinburgh
Redox-active Macrocyclic Complexes : Rings, Stacks and Liquid Crystals
- May 4 Prof. A. J. Kresge, University of Toronto
The Ingold Lecture Reactive Intermediates : Carboxylic-acid Enols and Other Unstable Species

- October 11 *Prof. P. Lugar, Frei Univ Berlin, FRG
Low Temperature Crystallography
- October 13 *Prof. R. Schmoltzer, Univ Braunschweig, FRG.
Calixarene-Phosphorus Chemistry: A New Dimension in Phosphorus
Chemistry
- October 18 Prof. A. Alexakis, Univ. Pierre et Marie Curie, Paris,
Synthetic and Analytical Uses of Chiral Diamines
- October 25 Dr.D.Martin Davies, University of Northumbria
Chemical reactions in organised systems.
- November 1 Prof. W. Motherwell, UCL London
New Reactions for Organic Synthesis
- November 3 Dr B. Langlois, University Claude Bernard-Lyon
Radical Anionic and Psuedo Cationic Trifluoromethylation
- November 8 Dr. D. Craig, Imperial College, London
New Stategies for the Assembly of Heterocyclic Systems
- November 15 Dr Andrea Sella, UCL, London
Chemistry of Lanthanides with Polypyrazoylborate Ligands
- November 17 Prof. David Bergbreiter, Texas A&M, USA
Design of Smart Catalysts, Substrates and Surfaces from Simple
Polymers
- November 22 *Prof. I Soutar, Lancaster University
A Water of Glass? Luminescence Studies of Water-Soluble Polymers.
- November 29 Prof. Dennis Tuck, University of Windsor, Ontario, Canada
New Indium Coordination Chemistry
- December 8 Professor M.T. Reetz, Max Planck Institut, Mulheim
Perkin Regional Meeting

1996

- January 10 Dr Bill Henderson, Waikato University, NZ
Electrospray Mass Spectrometry - a new sporting technique
- January 17 Prof. J. W. Emsley, Southampton University
Liquid Crystals: More than Meets the Eye
- January 24 Dr Alan Armstrong, Nottingham University
Alkene Oxidation and Natural Product Synthesis
- January 31 Dr J. Penfold, Rutherford Appleton Laboratory,
Soft Soap and Surfaces
- February 7 Dr R.B. Moody, Exeter University
Nitrosations, Nitrations and Oxidations with Nitrous Acid
- February 12 Dr Paul Pringle, University of Bristol
Catalytic Self-Replication of Phosphines on Platinum(O)
- February 14 Dr J. Rohr, Univ Gottingen, FRG
Goals and Aspects of Biosynthetic Studies on Low Molecular Weight
Natural Products
- February 21 Dr C R Pulham, Univ. Edinburgh
Heavy Metal Hydrides - an exploration of the chemistry of stannanes
and plumbanes
- February 28 Prof. E. W. Randall, Queen Mary & Westfield College
New Perspectives in NMR Imaging
- March 6 Dr Richard Whitby, Univ of Southampton
New approaches to chiral catalysts: Induction of planar and metal
centred asymmetry
- March 7 Dr D.S. Wright, University of Cambridge
Synthetic Applications of Me₂N-p-Block Metal Reagents

- March 12 RSC Endowed Lecture - Prof. V. Balzani, Univ of Bologna
Supramolecular Photochemistry
- March 13 Prof. Dave Garner, Manchester University
Mushrooming in Chemistry
- April 30 Dr L.D.Pettit, Chairman, IUPAC Commission of Equilibrium Data
pH-metric studies using very small quantities of uncertain purity

* indicates lectures attended.

PHORMAT Pulse Sequences

```

/* phmatfbp.sm4 WW 941204 based on 940906 +tau2 */

.title    phormat flip back plus synchronized

.a_mode      0
.channels    2
.include     defs.inc
.lpct        al
.time        pw pw1 pw2 tm2 tau2 tau tau8 tau9 ct rd ad pd
aqtm=((dw*al)+1u)
          DS=((tau9/3.)-pw-1u-ct+(pw1/2.))
          DC=(pw1/2.)
          DE1=(tau-(pw2/2.))
          DB=((tm2-tau2)/3.)+tau-(pw2/2.)-(pw1/2.)
          DD=((tau9/3.)-tau8-(2.*tau)-((tm2-tau2)/3.)-pw1)
          DE=(tau-(pw1/2.)-(pw2/2.))
          RD=(rd+((tm2-tau2)/3.))
          AD=(ad+tau-(pw2/2.)-rd)

.amp        a a1 a2

/* extm=(pd+pw+ct+(5*tau)+(3*pw2)+tm1+(2*tau8)+(2*TAU9)+ad+rd+aqtm)*/
/* .float  txduty2=((pw+ct+(5*tau)+(3*pw2)+tm1+(2*TAU9)+ad+rd+aqtm)/extm)*/

.program
start:      A1(SE Xecho)                T1(1m);
            A1(SE Xproj1)  A2(SE H90)    T1(1u);
            A1(SE Xproj2)  A2(SE Hfb)    T1(1u);
loop:       A1(AT Xcp)    A2(CU H90)     S2(TB) T1(pd);
wmm:        S2(TB) T1(.1u) I1(jump xl wmm);
amm:        S2(TB) T1(.1u) I1(jump xh amm);
wm:         S2(TB) T1(.1u) I1(jump xl wm);
am:         S2(TB) T1(.1u) I1(jump xh am);
            S2(TB) T1(DS);
            S2(TG) T1(pw);
            S2(TG) T1(1u);
wz:         A2(AT Hcp)    S1(TG)          S2(TG) T1(1u) I1(jump xl wz);
az:         S1(TG)       S2(TG) T1(.1u) I1(jump xh az);
            S1(TG)       S2(TG) T1(DC);
            A1(CU Xecho)  A2(AT Hdec)    S2(TG) T1(DE1);
            S1(TG)       S2(TG) T1(pw2);
            A1(CU Xproj1) S1(TG)          S2(TG) T1(DB);
            S1(TG)       S2(TG) T1(pw1);
            A1(AT Xread)  S2(TG) T1(DD);
wf:         S2(TG) T1(.1u) I1(jump xl wf);
af:         S2(TG) T1(.1u) I1(jump xh af);
            S1(TG)       S2(TG) T1(pw1);
            A1(AT Xecho)  S2(TG) T1(DE);
            S1(TG)       S2(TG) T1(pw2);
            A1(CU Xproj2) S2(TG) T1(DB);
            S1(TG)       S2(TG) T1(pw1);
            A1(AT Xread)  S2(TG) T1(DD);
ws:         S2(TG) T1(.1u) I1(jump xl ws);

```

```

as:
      S1(TG)      S2(TG) T1(.1u) I1(jump xh as);
      A1(AT Xecho) S1(TG)      S2(TG) T1(pw1);
      A1(AT rcvr)  S1(TG)      S2(TG) T1(DE);
      S1(TB)      S2(TG) T1(pw2);
      S1(TB RE)   S2(TG) T1(RD);
      S1(TB RE AE) S2(TG) T1(AD);
      A2(CU Hfb)  S2(TG) T1(aqtm);
      S2(TB) T1(1u) I1(jump loop);

```

```

.list1 Xcp P(0);
.list1 rcvr P(0);
.list1 Xecho P(0); P(0); P(0); P(0); P(0); P(0); P(0); P(0);
      P(180); P(180); P(180); P(180); P(180); P(180); P(180); P(180);

.list1 Xproj1 P(90); P(90); P(270); P(270); P(90); P(90); P(270); P(270);
      P(180); P(180); P(0); P(0); P(180); P(180); P(0); P(0);
      P(180); P(180); P(0); P(0); P(180); P(180); P(0); P(0);
      P(90); P(90); P(270); P(270); P(90); P(90); P(270); P(270);

.list1 Xproj2 P(90); P(90); P(90); P(90); P(270); P(270); P(270); P(270);
      P(180); P(180); P(180); P(180); P(0); P(0); P(0); P(0);

.list1 Xread P(270);

.list2 H90 P(0) A(a); P(180) A(a);
.list2 Hfb P(180) A(a); P(0) A(a);
.list2 Hcp P(90) A(a1);
.list2 Hdec P(90) A(a2);

```

```

.strings
abph=02202002200202203113133131131331
pw<H 90 pulse
pw1<X 90 pulse
pw2<X 180 pulse
a<H 90 power
a1<H cp power
a2<H dec power
ct<contact time
tm2<evolution time
tau2<extra time
tau<echo time
tau9<rotor period
tau8<dec. off time
aqtm<acq time
pd<recycle delay
extm<time per scam
dw<dwell time

```

```
/* phmatfbm.sm4 WW 941204 based on 940906 +tau2 */
```

```
.title    phormat flip back minus synchronized
```

```
.a_mode    0
```

```
.channels  2
```

```
.include   defs.inc
```

```
.lpct     al
```

```
.time     pw pw1 pw2 tm2 tau2 tau tau8 tau9 ct rd ad pd
```

```
aqtm=((dw*al)+1u)
```

```
DS=((tau9/3.)-pw-1u-ct+(pw1/2.))
```

```
DC=(pw1/2.)
```

```
DE=(tau-(pw2/2.)-(pw1/2.))
```

```
DB1=(((tm2+tau2)/3.)+tau-(pw2/2.))
```

```
DD=((tau9/3.)-tau8-(2.*tau)-((tm2+tau2)/3.)-pw1)
```

```
DB=(((tm2+tau2)/3.)+tau-(pw1/2.)-(pw2/2.))
```

```
RD=rd
```

```
AD=(ad+tau-(pw2/2.)-rd)
```

```
.amp     a a1 a2
```

```
/*      extm=(pd+pw+ct+(5*tau)+(3*pw2)+tm1+(2*tau8)+(2*TAU9)+ad+rd+aqtm)*/
```

```
/* .float txduty2=((pw+ct+(5*tau)+(3*pw2)+tm1+(2*TAU9)+ad+rd+aqtm)/extm)*/
```

```
.program
```

```
start:   A1(SE Xecho)
```

```
T1(1m);
```

```
         A1(SE Xproj1) A2(SE H90)
```

```
T1(1u);
```

```
         A1(SE Xproj2) A2(SE Hfb)
```

```
T1(1u);
```

```
loop:    A1(AT Xcp)  A2(CU H90)
```

```
S2(TB) T1(pd);
```

```
wmm:
```

```
S2(TB) T1(.1u) I1(jump xl wmm);
```

```
amm:
```

```
S2(TB) T1(.1u) I1(jump xh amm);
```

```
wm:
```

```
S2(TB) T1(.1u) I1(jump xl wm);
```

```
am:
```

```
S2(TB) T1(.1u) I1(jump xh am);
```

```
S2(TB) T1(DS);
```

```
S2(TG) T1(pw);
```

```
         A2(AT Hcp)
```

```
S1(TG)
```

```
S2(TG) T1(1u);
```

```
wz:
```

```
S1(TG)
```

```
S2(TG) T1(.1u) I1(jump xl wz);
```

```
az:
```

```
S1(TG)
```

```
S2(TG) T1(.1u) I1(jump xh az);
```

```
S1(TG)
```

```
S2(TG) T1(DC);
```

```
         A1(CU Xecho)  A2(AT Hdec)
```

```
S2(TG) T1(DB1);
```

```
S1(TG)
```

```
S2(TG) T1(pw2);
```

```
         A1(CU Xproj1)
```

```
S2(TG) T1(DE);
```

```
S1(TG)
```

```
S2(TG) T1(pw1);
```

```
         A1(AT Xread)
```

```
S2(TG) T1(DD);
```

```
wf:
```

```
S2(TG) T1(.1u) I1(jump xl wf);
```

```
af:
```

```
S2(TG) T1(.1u) I1(jump xh af);
```

```
S1(TG)
```

```
S2(TG) T1(pw1);
```

```
         A1(AT Xecho)
```

```
S2(TG) T1(DB);
```

```
S1(TG)
```

```
S2(TG) T1(pw2);
```

```
         A1(CU Xproj2)
```

```
S2(TG) T1(DE);
```

```
S1(TG)
```

```
S2(TG) T1(pw1);
```

```
         A1(AT Xread)
```

```
S2(TG) T1(DD);
```

```
ws:
```

```
S2(TG) T1(.1u) I1(jump xl ws);
```

```
as:
```

```
S2(TG) T1(.1u) I1(jump xh as);
```

```
S1(TG)
```

```
S2(TG) T1(pw1);
```

```
         A1(AT Xecho)
```

```
S2(TG) T1(DB);
```

```
S1(TG)
```

```
S2(TG) T1(pw2);
```

```
         A1(AT rcvr)
```

```
S1(TB)
```

```
S2(TG) T1(RD);
```

```
S1(TB RE)
```

```
S2(TG) T1(AD);
```

```

                S1(TB RE AE) S2(TG) T1(aqtm);
                A2(CU Hfb)    S2(TG) T1(pw);
                               S2(TB) T1(1u) I1(jump loop);

.list1 Xcp P(0);
.list1 rcvr P(0);
.list1 Xecho P(0); P(0); P(0); P(0); P(0); P(0); P(0); P(0);
           P(180); P(180); P(180); P(180); P(180); P(180); P(180); P(180);

.list1 Xproj1 P(90); P(90); P(270); P(270); P(90); P(90); P(270); P(270);
            P(180); P(180); P(0); P(0); P(180); P(180); P(0); P(0);
            P(180); P(180); P(0); P(0); P(180); P(180); P(0); P(0);
            P(90); P(90); P(270); P(270); P(90); P(90); P(270); P(270);

.list1 Xproj2 P(90); P(90); P(90); P(90); P(270); P(270); P(270); P(270);
            P(180); P(180); P(180); P(180); P(0); P(0); P(0); P(0);

.list1 Xread P(270);

.list2 H90 P(0) A(a); P(180) A(a);
.list2 Hfb P(180) A(a); P(0) A(a);
.list2 Hcp P(90) A(a1);
.list2 Hdec P(90) A(a2);

.strings
abph=02202002200202203113133131131331
pw<H 90 pulse
pw1<X 90 pulse
pw2<X 180 pulse
ct<contact time
a< H 90 power
a1<H cp amplitude
a2<H dec power
tm2<evolution time
tau2<extra time
tau<echo time
tau9<rotor period
tau8<dec. off time
aqtm<acq time
pd<recycle delay
extm<time per scam
dw<dwel time

```

PHORMAT Acqpars Files.

```

# phmatfbp.acq #####
#
# The file format is as follows
#
# si_name;long name;value;units;min;max;decimal pnts;user level;data type
#
# a - is a blank field.
# tabs and spaces are allowed if you wish to seperate the fields a little
# but a line can be only 80 characters.
#
# first line = ppfn and na
#
na;number acqs;32;-;8;1000;0;1;long
#
# channel assignment and sf values
ch1;ppg ch1;1;-;1;4;0;1;long
ch2;ppg ch2;2;-;1;4;0;1;long
sf1;X freq;100.621916;MHz;10.0;600.0;6;1;float
sf2;H freq;400.129766;MHz;10.0;600.0;6;1;float
# timing variables
#
pw1;X 90 pulse;5.5;u;.1;100;1;1;float
pw;H 90 pulse;5.5;u;.1;100;1;1;float
pw2;X 180 pulse;10.5;u;.1;100;1;1;float
ct;contact time;3;m;.001;30;3;1;float
sw;spectrum width acq.;40;kHz;1;2000;1;1;float
sw2;spectrum width evo.;20;kHz;1;2000;1;1;float
dw;dwel time;25;u;.5;1000;2;1;float
dw2;dwel time 2nd dim.;50;u;.5;1000;2;1;float
#
a;H 90 power;255;-;0;255;0;1;long
a1;H cp power;200;-;0;255;0;1;long
a2;H dec. power;255;-;0;255;0;1;long
#
al;acq length;128;-;1;4096;0;1;long
al2;acq length 2nd dim.;64;-;1;1024;0;1;long
aqtm;acq time;12.801;m;.002;300;3;1;float
gain;receiver gain;1412;-;1;1414;0;1;float
ad;acq delay;25;u;1;500;1;1;float
rd;receiver delay;15;u;1;100;1;1;float
ff;filter width;26;kHz;1;2000;1;1;float
tau;echo time;15;u;.1;1000;1;1;float
tau8;dec. off time;1000;u;1;10000;1;1;float
tm2;evolution time;0.1;u;0.1;100000;1;1;float
tau9;rotor period;33333.3;u;10000.0;100000.0;1;1;float
tau2;extra time;0.1;u;0.1;10;1;1;float
#
dp;dummy pulses;0;-;0;32;0;1;long
pd;pulse delay;5;s;1;3600;1;1;float
#txduty2;trans duty;0.1;-;0.0;0.2;4;1;float
#
#si_name;long name;value;units;min;max;decimal pnts;user level;data type

```

PHORMAT Acquisition Macro.

```
/* phmatS2fb */
/* A macro to collect 2D data sets into 2 separate files */
/* acq has to be the active buffer before running this macro */
/* acq is buffer name for starting data parameters */
/* al is the length of the FID */
/* al2 is the number of fid pairs collected in the second dimension */
/* dw2 is the dwell time for the second dimension */
/* tm2 is the evolution time actually used in the pulse program */
/* Get filename to store data */

file_p = query "file name stem for + & - data: " -s;
strcpy(file_m, file_p);
strcat(file_p, "_p");
strcat(file_m, "_m");

/* Get current values from acq panel */
al2 = get_acq_val al2 -b acq;
al = get_acq_val al -b acq;
dw2 = get_acq_val dw2 -b acq;
tm2 = get_acq_val tm2 -b acq;

saip; /* Set the 2D acq in progress flag */

set_acq_val pPFN phmatfbp -b acq;
file_p = create al al2 acq; /* Create a new full sized file(+) */
set_acq_val pPFN phmatfbm -b acq;
file_m = create al al2 acq; /* Create a new full sized file(-) */

for(i=0; i < al2; i = i + 1) {
    set_ni i; /* Set ni value in acq info panel */
    set_acq_val pPFN phmatfbp -b acq;
    zgw acq;
    file_p = append acq -r i;
    set_acq_val pPFN phmatfbm -b acq;
    zgw acq;
    file_m = append acq -r i;
    tm2 = tm2 + dw2; /* Advance evolution time */
    set_acq_val tm2 tm2 -b acq;
}

caip; /* Clear the 2D acq in progress flag */
```


PHORMAT Processing Macro.

```

/* phormat process */
/* macro for processing 2 separately acquired + and - datasets */ /* GmcG October 1996 */
/* display 4 viewports */
/* process panel displayed to speed up processing */ panel_process;
format "2x2";
dis;
info "Click in top left viewport";
info "Read p dataset into top left viewport";
bufnamep = query "name of buffer for pdata?"; pdata = copy bufnamep;
dis pdata;
info "Click in top right viewport";
info "Read m dataset into top right viewport"; bufnamem = query "name of buffer for mdata?"; mdata
= copy bufnamem;
dis mdata;
/* parameters and definitions required for processing */ al = get_acq_val al -b pdata;
aldouble = al*2;
info "Click in top left viewport";
/* add p and m data */
real=pdata+mdata;
dis real;
info "Click in top right viewport";
/* subtract p and m data */ imag=pdata-mdata;
phase imag 90 0;
dis imag;
info "Click in top left viewport";
/* zero fill real dataset -> twice original al */ zf real aldouble;
dis real;
info "real zero filled -> 2xal";
info "Click in top right viewport";
/* zero fill imag dataset -> twice original al */ /* shift imag dataset al points to the right */ /* -> first
al points zero */
zf imag aldouble;
dsr imag al;
dis imag;
info "imag shifted al points to right";
info "Click in bottom left viewport";
/* add real and imag */
final = real +imag;
dis final;
info "real and imag combined";
/* set number of data points back to original al */ setsize final al;
dis final;
info "size of final -> al";
/* processing of t2 dimension */

/* line broadening */
lb = query "Enter line broadening required (Hz)"; em final lb;
dis final;
info "line broadening applied";
/* Complex FT of t2 */
size = query "Enter number of points for FT (must be >=al)";
zf final size;
ft final;

```

```
dis final;
info "Complex FT applied to t2";
/* Phase first row of F2 */
view -d1 final;
dis final;
info "Click on first row and phase, then click OK in phasing panel"; panel_phase;
info "Phasing applied to F2 dimension";
/* Phase sensitive sort */
phasesort = query "psort or psort -i?" -m psorttype;
if (phasesort == 1) {
    psort final;
}
if (phasesort == 2) {
    psort -i final;
}
dis final;
info "Phase sensitive sort applied";
/* processing of t1 dimension */
view -d2 final;
dis final;
/* line broadening */
lb = query "Enter line broadening required (Hz)";
em final lb;
dis final;
info "line broadening applied";
/* multiplication of first point in t1 by 0.5 */ view -d2 final;
mult_first_pt 0.5;
dis final;
info "first point multiplication applied";
/* Complex FT of t1 */
size = query "Enter number of points for FT (must be >=al)"; zf final size;
ft final;
dis final;
info "Complex FT applied to t1";
/* Phase F1 dimension */
view -d2 final;
dis final;
info "Click on rows to phase, then click OK in phasing panel"; panel_phase;
info "Phasing applied to F1 dimension";
/* Displays F2 dimension parallel to horizontal axis */ view -d1 final;
dis final;
panel_twod;
info "Processing finished";
```

Acquisition Parameters for the PHORMAT Spectra Described in Chapter 7.

The acquisition parameters given in this section use the nomenclature as defined for the CMX spectrometer, and are given in the acqpars file for the PHORMAT pulse sequence. Similarly, the processing applied for each system, as carried out using the processing macro already given, is summarised.

CI-PV19: γ **Acquisition**

na=	384	dw2=	80.0 μ s
pd=	3.0 s	al=	512
spin rate=	30 Hz	al2=	100
sf1=	100.625836 MHz	aqtm=	6.401 ms
sf2=	400.1265 MHz	ad=	14 μ s
pw1=	3.9 μ s	rd=	50.0 μ s
pw=	3.9 μ s	tau=	50.0 μ s
pw2=	7.8 μ s	tau8=	1.0 ms
ct=	7.0 ms	tm2=	0.1 μ s
sw=	80.0 kHz	tau9=	33.333 ms
sw2=	12.5 kHz	tau2=	8.0 μ s
dw=	12.5 μ s		

Processing.

Both dimensions were zero-filled to 512 points.

gb=100 Hz

gb1=100 Hz

CI-DR278 VI.

Acquisition.		dw=	12.5 μ s
na=	256	dw2=	59.5 μ s
pd=	4.0 s	al=	256
spin-rate=	30 Hz.	al2=	200
sf1=	100.621313 MHz	aqtm=	3.201 ms
sf2=	400.12525 MHz	ad=	12.0 μ s
pw1=	3.8 μ s	rd=	40.0 μ s
pw=	3.8 μ s	tau=	50.0 ms
pw2=	7.6 μ s	tau8=	1.0 ms
ct=	6.0 ms	tm2=	0.1 μ s
sw=	80.0 kHz	tau9=	33.333 ms
sw2=	16.8 kHz	tau2=	8.0 μ s

Processing.

Both dimensions were zero-filled to 512 points.

gb=100 Hz

gb1=30 Hz

CI-PR 57:1

Acquisition.		dw=	10.0 μ s
na=	800	dw2=	67.0 μ s
spin-rate=	30 Hz	al=	256
pd=	3.0 s	al2=	40
sf1=	40.55728 MHz	aqtm=	2.561 ms
sf2=	400.1265 MHz	ad=	13.0 μ s
pw1=	7.0 μ s	rd=	30.0 μ s
pw=	4.0 μ s	tau=	30.0 μ s
pw2=	14.0 μ s	tau8=	1.0 ms
ct=	6.0 ms	tm2=	0.1 μ s
sw=	100.0 kHz	tau9=	33.333 ms
sw2=	15.0 kHz	tau2=	4.0 μ s

Processing.

Both dimensions were zero-filled to 512 points.

gb=100 Hz

gb1=50 Hz

Addendum

Single-Crystal X-Ray Structure.

After completion of writing this thesis a single-crystal structure determination of DR278 polymorph A was obtained. In this addendum the preliminary results obtained from this structure will be presented along with information on how the NMR data are consolidated by the structural analysis. The structure determination was carried out Dr A. Batsanov within the Durham University crystallography service.

A single crystal of DR278 was obtained by recrystallisation from a 50/50 mixture of CD₂Cl₂ and MeOH. Over a period of one month thin red needle-like crystals were obtained. A suitable crystal was extracted for X-ray analysis. However, these crystals proved to be relatively poor diffractors.

The diffraction experiments were carried out on a Rigaku AFC6S 4-circle diffractometer with a Cryostream open-flow N₂ gas cryostat, using graphite-monochromated Cu-K_α radiation, $\bar{\lambda}=1.54184\text{\AA}$. The unit cell was refined on the setting angle of 25 reflections with $15<\theta<24^\circ$. The crystal structure was found to be monoclinic, with space group P2₁ / c (No. 14), Z=4. The room-temperature data were corrected for absorption by the empirical method (72 azimuthal scans of 2 reflections, minimum and maximum transmission factors of 0.79 and 1.00) using the TEXSAN software.¹ The structure was solved by direct methods and refined by full-matrix least squares against all positive F², using SHELXTL software.² The single-crystal

determinations were carried out at 296 and 150 K. The geometrical parameters were found to be essentially the same and are therefore discussed together (the data in brackets refer to the low-temperature study). The data collection, structure refinement and crystal data are given in Tables 1 to 6 for both structure determinations.

In both studies, N(1), N(2) and C(1) to C(6) of the aromatic ring were found to be disordered over two positions, A and B, with occupancies refined to 53 and 47% at 296 K, and 47 and 53% at 150 K, respectively. Additionally, at 296 K the O(3) and O(4) sites were considered to be disordered over two positions, A and B, with occupancies refined to 35 and 65%. The disordered aromatic rings were refined as idealised rigid bodies.

Results.

Notwithstanding the relatively small lattice volume (17.1 [16.6] \AA^3 per non-hydrogen atom versus 18 \AA^3), the crystal packing leaves considerable space for molecular disorder. Thus, the azo group is disordered between two planar *trans*-conformations, in one of which (A) the lone-pair of N(2) is directed away from N(3), while in the other (B) it points towards N(3). Consequently, the benzene ring linked to N(2) is also disordered over two positions, A and B, which differ by a rotation of *ca.* 17 [16] $^\circ$ around the C(4) atom as a pivot, and by a dihedral angle of 10 [7.5] $^\circ$ between the ring planes. This is shown in Figure 1, where the thermal ellipsoids are at 30%.

The conjugation, which extends over both aromatic rings, the azo group and the nitro group, results in an essentially planar system (ignoring the long ester chains

at N(5)). The amido group is inclined at 5.8 [5] degrees to the benzene ring plane. The twists around the C(1)-N(2) and N(1)-C(7) bonds are 14.7 [10.3] $^{\circ}$ and 3.7 [4.9] $^{\circ}$ for the A conformation, and are 12.7 [10.6] $^{\circ}$ and 4.3 [7.1] $^{\circ}$ for the B conformation.

The B configuration is stabilised by an intramolecular N(3)-H \cdots N(2) hydrogen bond. For the idealised position of the hydrogen atom the H \cdots N(2) distance is 2.13 [2.21] Å, the N(3) \cdots N(2) distance is 2.79 [2.84] Å, and the N(3)-H-N(2) angle is 133 [128] $^{\circ}$. Also, the A position results in a shorter internuclear contact for H \cdots N(1) of 2.05 [2.15] Å and a N(3)-N(1) separation of 2.50 [2.56] Å. However, the N(3)-H-N(1) angle of 112 [108] $^{\circ}$ is rather small for a normal hydrogen bond. The atomic coordinates, bond lengths and bond angles are given in Tables 2, 3 and 4 respectively.

The out-of-plane substituents at N(5) prevent a stacking arrangement of the entire molecule, but it is possible to discern partial stacks as shown in Figure 2. They include pairs of anti-parallel C(1-6) aromatic rings with a fairly short interplanar separation of *ca.* 3.3 Å, which brings about close contacts between the nitro and azo groups. This is a typical separation for π - π stacking. These dimers are interleaved by the amido group as shown in Figure 2. The two positions of the disordered azophenyl moiety occupy essentially the same space, and, additionally, there is not much room perpendicular to the plane of the aromatic rings. Hence, if interconversion occurs between A and B, as suggested by the NMR results, then it would seem likely that the mechanism for the inversion involves a linear, or near-linear, transition state. Consequently, the rotation mechanism proposed earlier appears to be less likely than thought.

For completeness, it should be noted that several other phenylazobenzene systems crystallise in the same $P2_1/c$ space group. Additionally, structural mimicry is common-place for structures based mainly on van der Waal interactions, such as these azobenzenes. This is a result of the fact that molecules which exhibit similar van der Waals surfaces crystallise in similar arrangements, assuming that hydrogen-bonding interactions do not dominate in the crystal formation. The similar *trans*-stilbene³ and N-salicylideneaniline⁴ molecules are both known to crystallise commonly in the $P2_1/c$ space group, and more often than not as monoclinic crystal systems.

In trying to relate the ^{15}N NMR shielding information to the crystal structure it appears plausible to suggest that the rotation of the C(1-6) aromatic ring from the plane of the azo linkage would shift the $\text{N}\alpha$ resonances more than those of the $\text{N}\beta$ resonances, irrespective of the electronegativity at each site. In Chapter 3 the shifts could not be predicated from the additivity relations for phenylazobenzene systems. Thus the increased shielding may be a result of the different stabilisation resulting from the π -orbital overlap across the system. As discussed earlier, however, it is clear that these hand-waving arguments cannot be considered at all accurate for predicting small shifts between similar environments, and a full quantum mechanical description of all of the interactions is required.

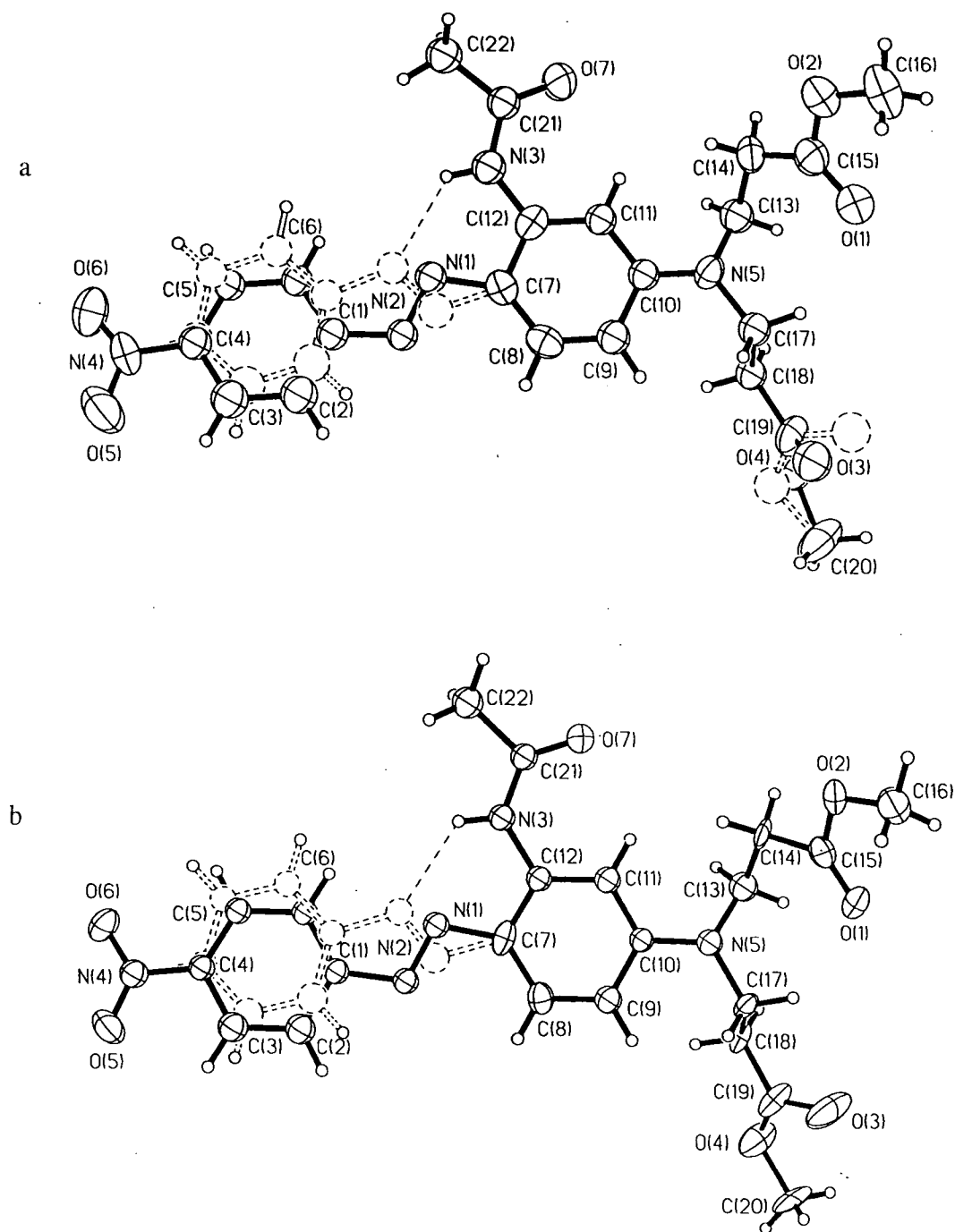


Figure 1.

ORTEP plots of the molecular conformations for the structure determination of DR278 form A at a/ 293 K and b/ 150 K. Thermal ellipsoids are shown at 30 % probability for clarity.

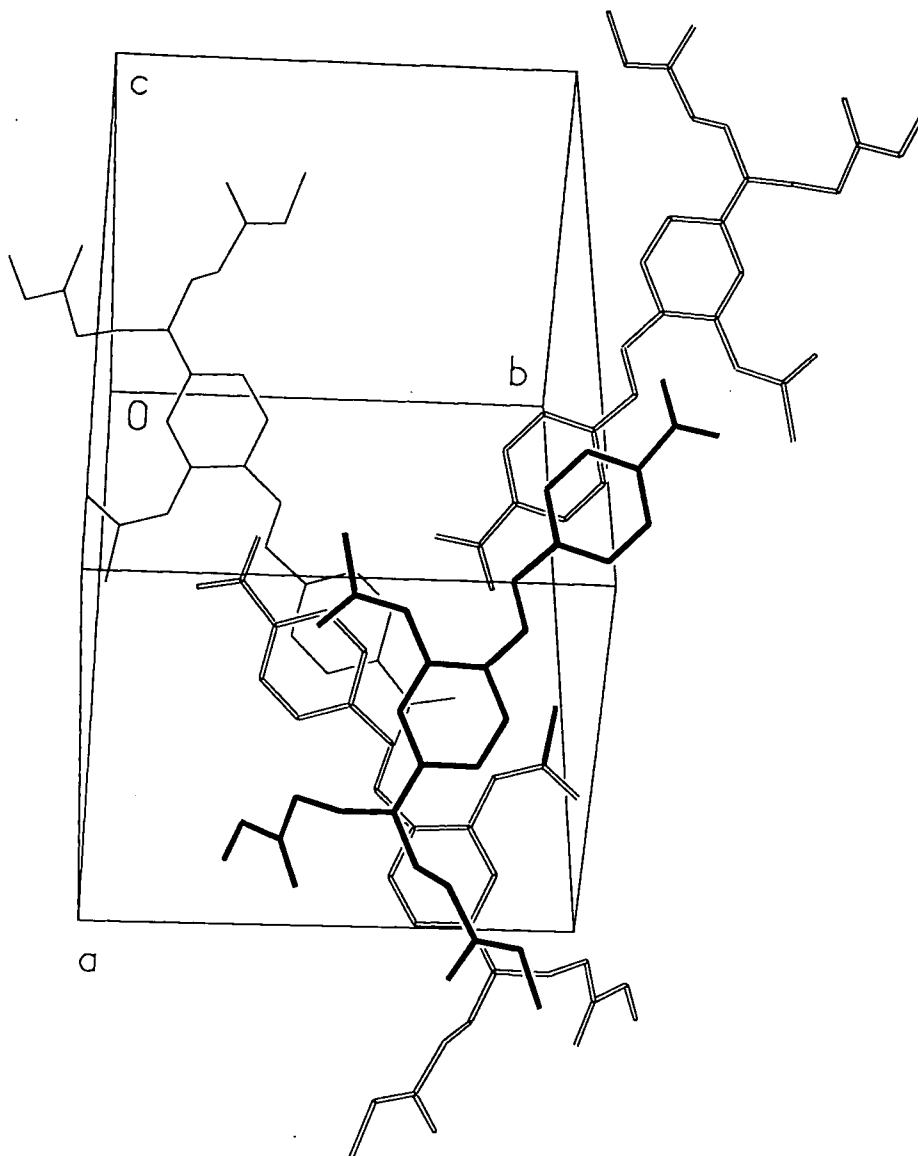


Figure 2.

Crystal packing of DR278 A as shown upon the (101) plane.

Table 1.
Crystal data and structure refinement for DR278 A at 293 K.

Identification	code96srv170	
Empirical formula	C ₂₂ H ₂₅ N ₅ O ₇	
Formula weight	471.47	
Temperature	293(2) K	
Wavelength	1.54184 Å	
Crystal system	Monoclinic	
Space group	P2(1)/c	
Unit cell dimensions	a = 18.353(2) Å	α = 90 deg.
	b = 12.230(2) Å	β = 98.40(1) deg.
	c = 10.475(2) Å	γ = 90 deg.
Volume	2326.0(7) Å ³	
Z	4	
Density (calculated)	1.346 g/cm ³	
Absorption coefficient	0.858 mm ⁻¹	
F(000)	992	
Crystal size	0.2 x 0.05 x 0.05 mm	
Theta range for data collection	4.36 to 75.01°	
Index ranges	-22 ≤ h ≤ 22,	-15 ≤ k ≤ 1,
	-1 ≤ l ≤ 11	
Reflections collected	4629	
Independent reflections	3398 [R(int) = 0.0908]	
Absorption correction	Semi-empirical from psi-scans	
Max. and min. transmission	1.000 and 0.789	
Refinement method	Full-matrix least-squares on F ²	
Data / restraints / parameters	1968 / 3 / 222	
Goodness-of-fit on F ²	1.021	
Final R indices [I > 2σ(I)]	R1 = 0.0702, wR2 = 0.1696	
R indices (all data)	R1 = 0.3085, wR2 = 0.2644	
Largest diff. peak and hole	.261 and -.187 e. Å ³	

Table 2. Atomic coordinates ($\text{\AA} \times 10^4$) and equivalent isotropic displacement parameters ($\text{\AA}^2 \times 10^3$) for DR278 A at 293 K. $U(\text{eq})$ is defined as one third of the trace of the orthogonalized U_{ij} tensor.

	x	y	z	$U(\text{eq})$
O(1)	1230(4)	-608(5)	6086(6)	115(2)
O(2)	2133(4)	-1744(6)	5731(8)	134(3)
O(3A)	128(9)	3228(15)	6136(13)	105(5)
O(4A)	-791(8)	3456(14)	4527(12)	96(7)
O(3B)	-301(5)	2492(8)	6029(9)	105(3)
O(4B)	-542(6)	3841(8)	4565(9)	96(4)
O(5)	4944(5)	7850(7)	-1714(8)	161(3)
O(6)	5140(4)	6580(7)	-2968(7)	129(3)
O(7)	2855(3)	-363(5)	976(6)	112(2)
N(1A)	3197(10)	3477(14)	991(17)	65(5)
N(2A)	3214(7)	4530(12)	1058(13)	62(4)
C(1A)	3668(7)	5043(10)	259(11)	69(3)
C(2A)	3806(8)	6147(10)	493(12)	91(4)
C(3A)	4213(9)	6737(8)	-292(15)	93(3)
C(4A)	4480(9)	6221(10)	-1312(15)	73(2)
C(5A)	4342(8)	5117(10)	-1546(12)	67(3)
C(6A)	3935(7)	4527(8)	-760(11)	69(3)
N(1B)	3059(8)	3928(17)	1249(15)	82(6)
N(2B)	3438(6)	3624(11)	445(12)	69(4)
C(1B)	3777(6)	4522(8)	-150(11)	69(3)
C(2B)	3708(7)	5610(10)	199(11)	91(4)
C(3B)	4052(8)	6426(7)	-417(13)	93(3)
C(4B)	4465(9)	6155(9)	-1383(14)	73(2)
C(5B)	4534(7)	5068(10)	-1733(11)	67(3)
C(6B)	4190(6)	4251(7)	-1116(11)	69(3)
N(3)	3149(3)	1432(5)	923(6)	76(2)
N(4)	4872(4)	6903(8)	-2062(9)	98(3)
N(5)	1312(3)	1297(5)	3834(5)	73(2)
C(7)	2704(4)	3098(8)	1814(8)	74(2)
C(8)	2298(4)	3571(7)	2659(8)	77(2)
C(9)	1847(4)	2994(6)	3343(7)	75(2)
C(10)	1778(4)	1844(6)	3196(7)	66(2)
C(11)	2205(4)	1351(6)	2354(7)	67(2)
C(12)	2684(4)	1922(8)	1690(6)	65(2)
C(13)	1081(4)	194(7)	3437(8)	83(3)
C(14)	1606(5)	-691(7)	3960(9)	113(4)
C(15)	1633(6)	-969(9)	5338(11)	101(3)
C(16)	2213(6)	-2080(9)	7059(12)	157(5)
C(17)	890(4)	1796(6)	4749(7)	72(2)
C(18)	209(4)	2383(6)	4071(6)	70(2)
C(19)	-186(5)	2975(9)	5003(8)	92(3)
C(20)	-1045(5)	4272(10)	5440(9)	148(5)
C(21)	3214(4)	382(7)	620(7)	72(2)
C(22)	3801(4)	138(7)	-216(7)	89(3)

Table 3.
Bond lengths [\AA] for DR278 A at 293 K.

O(1)-C(15)	1.234(10)	O(2)-C(15)	1.342(11)
O(2)-C(16)	1.437(10)	O(3A)-C(19)	1.279(10)
O(4A)-C(19)	1.290(11)	O(4A)-C(20)	1.503(11)
O(3B)-C(19)	1.271(8)	O(4B)-C(19)	1.293(10)
O(4B)-C(20)	1.488(9)	O(5)-N(4)	1.216(9)
O(6)-N(4)	1.197(9)	O(7)-C(21)	1.215(8)
N(1A)-N(2A)	1.29(2)	N(1A)-C(7)	1.42(2)
N(2A)-C(1A)	1.41(2)	C(1A)-C(2A)	1.39
C(1A)-C(6A)	1.39	C(2A)-C(3A)	1.39
C(3A)-C(4A)	1.39	C(4A)-C(5A)	1.39
C(4A)-N(4)	1.413(11)	C(5A)-C(6A)	1.39
N(1B)-N(2B)	1.23(2)	N(1B)-C(7)	1.39(2)
N(2B)-C(1B)	1.45(2)	C(1B)-C(2B)	1.39
C(1B)-C(6B)	1.39	C(2B)-C(3B)	1.39
C(3B)-C(4B)	1.39	C(4B)-C(5B)	1.39
C(4B)-N(4)	1.434(11)	C(5B)-C(6B)	1.39
N(3)-C(21)	1.332(8)	N(3)-C(12)	1.391(9)
N(5)-C(10)	1.340(8)	N(5)-C(17)	1.452(8)
N(5)-C(13)	1.456(9)	C(7)-C(8)	1.365(10)
C(7)-C(12)	1.444(10)	C(8)-C(9)	1.367(9)
C(9)-C(10)	1.419(9)	C(10)-C(11)	1.399(9)
C(11)-C(12)	1.387(9)	C(13)-C(14)	1.499(11)
C(14)-C(15)	1.477(12)	C(17)-C(18)	1.523(9)
C(18)-C(19)	1.486(9)	C(21)-C(22)	1.514(9)

Table 4.
Bond angles [deg] for DR278 A at 293 K.

C(15)-O(2)-C(16)	117.8(9)	C(19)-O(4A)-C(20)	112.8(9)
C(19)-O(4B)-C(20)	113.5(8)	N(2A)-N(1A)-C(7)	108(2)
N(1A)-N(2A)-C(1A)	115(2)	C(2A)-C(1A)-C(6A)	120.0
C(2A)-C(1A)-N(2A)	115.9(10)	C(6A)-C(1A)-N(2A)	124.0(10)
C(1A)-C(2A)-C(3A)	120.0	C(4A)-C(3A)-C(2A)	120.0
C(3A)-C(4A)-C(5A)	120.0	C(3A)-C(4A)-N(4)	115.2(10)
C(5A)-C(4A)-N(4)	124.8(10)	C(4A)-C(5A)-C(6A)	120.0
C(1A)-C(6A)-C(5A)	120.0	N(2B)-N(1B)-C(7)	115(2)
N(1B)-N(2B)-C(1B)	113(2)	C(2B)-C(1B)-C(6B)	120.0
C(2B)-C(1B)-N(2B)	123.4(9)	C(6B)-C(1B)-N(2B)	116.6(9)
C(3B)-C(2B)-C(1B)	120.0	C(2B)-C(3B)-C(4B)	120.0
C(5B)-C(4B)-C(3B)	120.0	C(5B)-C(4B)-N(4)	113.9(10)
C(3B)-C(4B)-N(4)	126.0(10)	C(6B)-C(5B)-C(4B)	120.0
C(5B)-C(6B)-C(1B)	120.0	C(21)-N(3)-C(12)	129.6(8)
O(6)-N(4)-O(5)	120.9(10)	O(6)-N(4)-C(4A)	123.2(11)
O(5)-N(4)-C(4A)	115.9(11)	O(6)-N(4)-C(4B)	119.1(11)
O(5)-N(4)-C(4B)	120.0(11)	C(10)-N(5)-C(17)	124.1(7)
C(10)-N(5)-C(13)	120.1(6)	C(17)-N(5)-C(13)	114.7(6)
C(8)-C(7)-N(1B)	107.6(10)	C(8)-C(7)-N(1A)	135.5(11)
C(8)-C(7)-C(12)	118.1(8)	N(1B)-C(7)-C(12)	134.3(11)
N(1A)-C(7)-C(12)	106.3(10)	C(7)-C(8)-C(9)	123.4(8)
C(8)-C(9)-C(10)	120.4(8)	N(5)-C(10)-C(11)	123.8(7)
N(5)-C(10)-C(9)	119.6(8)	C(11)-C(10)-C(9)	116.5(8)
C(12)-C(11)-C(10)	123.6(8)	C(11)-C(12)-N(3)	124.1(9)
C(11)-C(12)-C(7)	117.8(8)	N(3)-C(12)-C(7)	118.1(8)
N(5)-C(13)-C(14)	114.8(7)	C(15)-C(14)-C(13)	116.8(8)
O(1)-C(15)-O(2)	120.3(11)	O(1)-C(15)-C(14)	126.9(11)
O(2)-C(15)-C(14)	112.7(10)	N(5)-C(17)-C(18)	111.8(6)
C(19)-C(18)-C(17)	111.7(6)	O(3A)-C(19)-O(4A)	119.5(12)
O(3B)-C(19)-O(4B)	122.9(9)	O(3B)-C(19)-C(18)	119.1(9)
O(3A)-C(19)-C(18)	122.0(11)	O(4A)-C(19)-C(18)	116.3(9)
O(4B)-C(19)-C(18)	115.9(8)	O(7)-C(21)-N(3)	125.3(8)
O(7)-C(21)-C(22)	119.6(8)	N(3)-C(21)-C(22)	115.1(8)

Table 5.
Anisotropic displacement parameters ($\text{Å}^2 \times 10^3$) for DR278 A at 293 K.
The anisotropic displacement factor exponent takes the form:
 $-2\pi^2 [h^2 a^{*2} U_{11} + \dots + 2 h k a^* b^* U_{12} + \dots]$

	U11	U22	U33	U23	U13	U12
O(1)	135(6)	96(5)	121(6)	7(4)	45(5)	0(4)
O(2)	152(7)	97(5)	167(7)	36(5)	66(6)	12(5)
O(5)	220(9)	98(6)	174(8)	7(6)	63(6)	-42(6)
O(6)	124(6)	174(8)	97(5)	19(5)	42(4)	-13(5)
O(7)	109(5)	88(4)	150(5)	-16(4)	52(4)	-26(4)
N(4)	101(6)	90(7)	106(7)	19(6)	24(5)	-30(6)
N(5)	71(4)	85(5)	66(4)	-17(4)	22(3)	-13(4)
C(7)	78(6)	73(6)	68(6)	6(6)	5(5)	-10(6)
C(8)	78(6)	64(6)	85(6)	-1(5)	-6(5)	-2(5)
C(12)	53(5)	95(7)	46(5)	2(5)	-3(4)	7(5)
C(14)	168(10)	72(7)	121(8)	-6(6)	90(8)	-23(7)
C(15)	112(9)	74(8)	124(10)	-10(7)	46(8)	-24(7)
C(16)	194(12)	131(11)	152(11)	56(9)	49(9)	-16(9)
C(19)	95(7)	126(8)	57(5)	12(6)	16(5)	18(6)
C(20)	140(9)	199(13)	115(8)	2(8)	51(7)	76(9)

Table 6.
 Hydrogen coordinates ($\text{\AA} \times 10^4$) and isotropic displacement parameters ($\text{\AA}^2 \times 10^3$)
 for DR278 A at 293 K.

	x	y	z	U(eq)
H(2A)	3627(11)	6492(13)	1175(15)	110
H(3A)	4306(12)	7476(8)	-136(20)	112
H(5A)	4521(11)	4772(14)	-2228(15)	80
H(6A)	3843(10)	3788(8)	-917(16)	83
H(2B)	3432(9)	5791(13)	845(14)	110
H(3B)	4006(11)	7154(8)	-184(18)	112
H(5B)	4811(10)	4887(14)	-2379(14)	80
H(6B)	4236(9)	3524(8)	-1350(15)	83
H(3N)	3422(3)	1884(5)	579(6)	91
H(8)	2332(4)	4324(7)	2779(8)	93
H(9)	1583(4)	3358(6)	3905(7)	89
H(11)	2166(4)	598(6)	2233(7)	80
H(131)	1011(4)	160(7)	2502(8)	100
H(132)	608(4)	50(7)	3713(8)	100
H(141)	1481(5)	-1348(7)	3455(9)	136
H(142)	2096(5)	-473(7)	3821(9)	136
H(161)	2585(6)	-2636(9)	7207(12)	235
H(162)	1754(6)	-2365(9)	7249(12)	235
H(163)	2356(6)	-1464(9)	7606(12)	235
H(171)	1199(4)	2316(6)	5278(7)	87
H(172)	740(4)	1237(6)	5313(7)	87
H(181)	356(4)	2911(6)	3467(6)	84
H(182)	-115(4)	1855(6)	3585(6)	84
H(201)	-1447(5)	4688(10)	4991(9)	222
H(202)	-658(5)	4760(10)	5796(9)	222
H(203)	-1213(5)	3864(10)	6123(9)	222
H(221)	4033(4)	810(7)	-408(7)	133
H(222)	3580(4)	-201(7)	-1005(7)	133
H(223)	4163(4)	-345(7)	235(7)	133

Table 1.
Crystal data and structure refinement for DR278 A at 150 K.

Identification code	97srv013
Empirical formula	C ₂₂ H ₂₅ N ₅ O ₇
Formula weight	471.47
Temperature	150(2) K
Wavelength	1.54184 Å
Crystal system	Monoclinic
Space group	P2(1)/c
Unit cell dimensions	a = 18.042(2) Å α = 90 deg. b = 12.198(2) Å β = 99.22(1) deg. c = 10.387(2) Å γ = 90 deg.
Volume	2256.4(7) Å ³
Z	4
Density (calculated)	1.388 Mg/m ³
Absorption coefficient	0.884 mm ⁻¹
F(000)	992
Crystal size	0.8 x 0.1 x 0.05 mm
Theta range for data collection	4.39 to 50.02 deg.
Index ranges	-17 ≤ h ≤ 17, -12 ≤ k ≤ 1, -1 ≤ l ≤ 9
Reflections collected	3020
Independent reflections	2222 [R(int) = 0.1126]
Absorption correction	None
Refinement method	Full-matrix least-squares on F ²
Data / restraints / parameters	1377 / 0 / 219
Goodness-of-fit on F ²	1.089
Final R indices [I > 2σ(I)]	R1 = 0.0787, wR2 = 0.1885
R indices (all data)	R1 = 0.2823, wR2 = 0.3073
Largest diff. peak and hole	.472 and -.222 e.Å ⁻³

Table 2.
Atomic coordinates ($\text{\AA} \times 10^4$) and equivalent isotropic displacement parameters ($\text{\AA}^2 \times 10^3$) for DR278 A at 150 K. $U(\text{eq})$ is defined as one third of the trace of the orthogonalized U_{ij} tensor.

	x	y	z	U(eq)
O(1)	6223(5)	-572(8)	6098(8)	80(3)
O(2)	7110(6)	-1767(9)	5728(11)	102(4)
O(3)	4698(6)	2604(11)	6027(10)	131(5)
O(4)	4374(6)	3805(9)	4557(9)	96(4)
O(5)	9950(6)	7946(8)	-1745(10)	105(4)
O(6)	10145(4)	6619(8)	-3003(8)	76(3)
O(7)	7856(4)	-385(7)	960(8)	72(3)
N(3)	8175(5)	1406(7)	917(8)	47(3)
N(4)	9883(5)	6992(10)	-2074(10)	58(3)
N(5)	6303(5)	1293(7)	3850(9)	48(3)
N(1A)	8222(13)	3502(18)	1039(22)	46(6)
N(2A)	8221(10)	4562(16)	1134(17)	46(6)
C(1A)	8650(9)	5078(12)	209(15)	46(4)
C(2A)	8762(10)	6195(12)	425(15)	64(5)
C(3A)	9189(11)	6790(10)	-333(19)	63(4)
C(4A)	9503(12)	6268(13)	-1306(19)	47(3)
C(5A)	9390(11)	5151(13)	-1522(16)	49(4)
C(6A)	8964(9)	4557(10)	-765(15)	48(5)
N(1B)	8059(15)	3995(28)	1144(26)	64(9)
N(2B)	8460(11)	3652(18)	465(21)	52(6)
C(1B)	8817(11)	4572(13)	-112(17)	46(4)
C(2B)	8749(11)	5664(15)	235(17)	64(5)
C(3B)	9063(13)	6484(11)	-436(22)	63(4)
C(4B)	9444(14)	6213(14)	-1453(23)	47(3)
C(5B)	9512(12)	5121(16)	-1800(18)	49(4)
C(6B)	9199(10)	4301(12)	-1130(17)	48(5)
C(7)	7726(6)	3081(11)	1810(10)	50(3)
C(8)	7307(6)	3591(10)	2673(11)	58(3)
C(9)	6848(6)	3005(9)	3352(11)	51(3)
C(10)	6790(6)	1876(9)	3170(10)	41(3)
C(11)	7220(6)	1338(9)	2366(10)	48(3)
C(12)	7713(6)	1933(10)	1729(10)	44(3)
C(13)	6057(6)	210(10)	3432(11)	61(4)
C(14)	6577(7)	-698(10)	3952(12)	78(5)
C(15)	6604(9)	-957(12)	5402(16)	79(5)
C(16)	7202(8)	-2100(11)	7060(18)	107(6)
C(17)	5881(6)	1844(9)	4742(10)	53(3)
C(18)	5186(5)	2429(11)	4037(10)	52(3)
C(19)	4782(8)	3000(15)	4961(16)	79(5)
C(20)	3935(7)	4348(12)	5439(12)	93(5)
C(21)	8228(6)	366(10)	656(10)	49(3)
C(22)	8820(6)	120(10)	-238(11)	67(4)

Table 3.
Bond lengths [\AA] for DR278 A at 150 K.

O(1)-C(15)	1.17(2)	C(4A)-C(5A)	1.39
O(2)-C(15)	1.35(2)	C(5A)-C(6A)	1.39
O(2)-C(16)	1.43(2)	N(1B)-N(2B)	1.17(3)
O(3)-C(19)	1.24(2)	N(1B)-C(7)	1.49(3)
O(4)-C(19)	1.26(2)	N(2B)-C(1B)	1.47(3)
O(4)-C(20)	1.462(13)	C(1B)-C(2B)	1.39
O(5)-N(4)	1.214(11)	C(1B)-C(6B)	1.39
O(6)-N(4)	1.229(11)	C(2B)-C(3B)	1.39
O(7)-C(21)	1.207(11)	C(3B)-C(4B)	1.39
N(3)-C(21)	1.304(12)	C(4B)-C(5B)	1.39
N(3)-C(12)	1.430(12)	C(5B)-C(6B)	1.39
N(4)-C(4A)	1.436(14)	C(7)-C(12)	1.403(14)
N(4)-C(4B)	1.45(2)	C(7)-C(8)	1.41(2)
N(5)-C(10)	1.404(12)	C(8)-C(9)	1.371(14)
N(5)-C(13)	1.439(13)	C(9)-C(10)	1.391(13)
N(5)-C(17)	1.454(12)	C(10)-C(11)	1.393(13)
N(1A)-N(2A)	1.30(3)	C(11)-C(12)	1.395(13)
N(1A)-C(7)	1.39(3)	C(13)-C(14)	1.50(2)
N(2A)-C(1A)	1.47(2)	C(14)-C(15)	1.53(2)
C(1A)-C(6A)	1.39	C(17)-C(18)	1.526(14)
C(1A)-C(2A)	1.39	C(18)-C(19)	1.47(2)
C(2A)-C(3A)	1.39	C(21)-C(22)	1.553(14)
C(3A)-C(4A)	1.39		

Table 4.
Bond angles [deg] for DR278 A at 150 K.

C(15)-O(2)-C(16)	114.9(11)	C(5B)-C(4B)-N(4)	115.8(14)
C(19)-O(4)-C(20)	119.4(11)	C(3B)-C(4B)-N(4)	123.6(14)
C(21)-N(3)-C(12)	129.0(10)	C(4B)-C(5B)-C(6B)	120.0
O(5)-N(4)-O(6)	122.9(11)	C(5B)-C(6B)-C(1B)	120.0
O(5)-N(4)-C(4A)	117.9(13)	N(1A)-C(7)-C(12)	109.8(14)
O(6)-N(4)-C(4A)	119.2(12)	N(1A)-C(7)-C(8)	132(2)
O(5)-N(4)-C(4B)	122.6(14)	C(12)-C(7)-C(8)	118.3(11)
O(6)-N(4)-C(4B)	114.4(13)	C(12)-C(7)-N(1B)	136(2)
C(10)-N(5)-C(13)	120.0(9)	C(8)-C(7)-N(1B)	105(2)
C(10)-N(5)-C(17)	121.3(9)	C(9)-C(8)-C(7)	121.9(11)
C(13)-N(5)-C(17)	116.6(9)	C(8)-C(9)-C(10)	119.0(11)
N(2A)-N(1A)-C(7)	108(2)	C(9)-C(10)-C(11)	120.7(10)
N(1A)-N(2A)-C(1A)	112(2)	C(9)-C(10)-N(5)	118.2(10)
C(6A)-C(1A)-C(2A)	120.0	C(11)-C(10)-N(5)	121.1(10)
C(6A)-C(1A)-N(2A)	126.8(12)	C(10)-C(11)-C(12)	119.9(10)
C(2A)-C(1A)-N(2A)	113.1(12)	C(11)-C(12)-C(7)	119.8(11)
C(1A)-C(2A)-C(3A)	120.0	C(11)-C(12)-N(3)	121.5(11)
C(4A)-C(3A)-C(2A)	120.0	C(7)-C(12)-N(3)	118.6(10)
C(3A)-C(4A)-C(5A)	120.0	N(5)-C(13)-C(14)	115.2(10)
C(3A)-C(4A)-N(4)	114.1(12)	C(13)-C(14)-C(15)	115.3(11)
C(5A)-C(4A)-N(4)	125.7(12)	O(1)-C(15)-O(2)	125(2)
C(4A)-C(5A)-C(6A)	120.0	O(1)-C(15)-C(14)	126(2)
C(1A)-C(6A)-C(5A)	120.0	O(2)-C(15)-C(14)	108.1(14)
N(2B)-N(1B)-C(7)	110(3)	N(5)-C(17)-C(18)	112.7(9)
N(1B)-N(2B)-C(1B)	109(3)	C(19)-C(18)-C(17)	111.4(11)
C(2B)-C(1B)-C(6B)	120.0	O(3)-C(19)-O(4)	117.0(13)
C(2B)-C(1B)-N(2B)	124.3(14)	O(3)-C(19)-C(18)	123(2)
C(6B)-C(1B)-N(2B)	115.6(14)	O(4)-C(19)-C(18)	118.5(14)
C(1B)-C(2B)-C(3B)	120.0	O(7)-C(21)-N(3)	128.5(11)
C(4B)-C(3B)-C(2B)	120.0	O(7)-C(21)-C(22)	118.3(10)
C(5B)-C(4B)-C(3B)	120.0	N(3)-C(21)-C(22)	113.1(10)

Table 5.
 Anisotropic displacement parameters ($\text{\AA}^2 \times 10^3$) for DR278 A at 150 K.
 The anisotropic displacement factor exponent takes the form:
 $-2\pi^2 [h^2 a^{*2} U_{11} + \dots + 2 h k a^* b^* U_{12} + \dots]$

	U11	U22	U33	U23	U13	U12
O(1)	90(7)	82(7)	80(7)	7(5)	52(6)	7(6)
O(2)	132(9)	67(7)	131(10)	31(7)	91(8)	4(7)
O(3)	172(11)	171(12)	55(7)	-1(8)	38(7)	78(9)
O(4)	93(8)	132(10)	67(7)	6(6)	23(6)	48(7)
O(5)	154(9)	65(7)	106(8)	-9(6)	51(7)	-37(6)
O(6)	78(6)	102(7)	53(6)	-7(5)	27(5)	0(5)
O(7)	78(6)	58(6)	89(6)	-5(5)	38(5)	-8(5)
C(7)	35(7)	89(10)	24(6)	16(7)	0(5)	-2(7)
C(8)	62(8)	63(9)	48(8)	9(7)	7(7)	-9(7)
C(14)	121(12)	68(10)	64(10)	-15(8)	76(9)	-32(9)
C(15)	87(12)	48(10)	116(15)	-8(10)	52(11)	-26(9)
C(16)	107(12)	71(11)	159(17)	27(11)	71(12)	15(9)
C(17)	64(8)	60(8)	39(7)	-2(7)	27(6)	8(7)
C(18)	41(7)	84(9)	34(7)	6(7)	19(6)	1(7)
C(19)	60(10)	135(16)	47(11)	-14(10)	20(8)	11(10)
C(20)	87(10)	119(13)	84(11)	-13(9)	43(9)	70(10)

Table 6.
 Hydrogen coordinates ($\text{\AA} \times 10^4$) and isotropic displacement parameters ($\text{\AA}^2 \times 10^3$) for
 DR278 A at 150 K.

	x	y	z	U(eq)
H(3N)	8477(5)	1843(7)	568(8)	57
H(2A)	8548(14)	6551(16)	1090(21)	77
H(3A)	9266(15)	7553(10)	-185(26)	75
H(5A)	9605(15)	4795(18)	-2188(22)	58
H(6A)	8887(13)	3793(10)	-912(22)	57
H(2B)	8489(16)	5849(21)	930(23)	77
H(3B)	9017(19)	7230(12)	-198(31)	75
H(5B)	9773(17)	4936(23)	-2495(24)	58
H(6B)	9245(15)	3555(13)	-1367(25)	57
H(8)	7330(6)	4364(10)	2775(11)	69
H(9)	6580(6)	3361(9)	3948(11)	62
H(11)	7172(6)	570(9)	2223(10)	58
H(131)	5973(6)	186(10)	2467(11)	73
H(132)	5568(6)	72(10)	3718(11)	73
H(141)	7090(7)	-502(10)	3806(12)	93
H(142)	6424(7)	-1367(10)	3436(12)	93
H(161)	7490(8)	-2784(11)	7174(18)	160
H(162)	6707(8)	-2217(11)	7310(18)	160
H(163)	7470(8)	-1528(11)	7613(18)	160
H(171)	6214(6)	2385(9)	5258(10)	63
H(172)	5729(6)	1298(9)	5354(10)	63
H(181)	5336(5)	2967(11)	3413(10)	62
H(182)	4847(5)	1887(11)	3535(10)	62
H(201)	3791(7)	5078(12)	5093(12)	140
H(202)	4243(7)	4419(12)	6302(12)	140
H(203)	3483(7)	3922(12)	5511(12)	140
H(221)	9042(6)	-605(10)	-37(11)	100
H(222)	9213(6)	681(10)	-76(11)	100
H(223)	8585(6)	145(10)	-1157(11)	100

References

1. TEXSAN: TEXRAY Structure Analysis Package, Ver. 5, 1989, Molecular Structure Corporation, The Woodlands, Texas, USA.
2. G. M. Sheldrick, SHELXTL, Ver. 5, 1994, Siemens Analytical X-Ray Instruments Inc., Madison, Wisconsin, USA.
3. J. A. Bouwstra, A. Schouten, J. Kroon and R. B. Helmholtz, *Acta Cryst.*, **C41**, 420, (1970).
4. K. Woznaik, H. He, J. Klinowski, W. Jones, T. Dziembowska and E. Grech, *J. Chem. Soc. Faraday Trans*, **91**, 77-85, (1995).

